The Dissertation Committee for Zhongjian Zhang Certifies that this is the approved version of the following dissertation:

Tip-Enhanced Raman Spectroscopy of Strained Semiconductor Nanostructures

Committee:

Edward Yu, Supervisor

Emanuel Tutuc

Sanjay Banerjee

Deji Akinwande

Keji Lai

Tip-Enhanced Raman Spectroscopy of Strained Semiconductor Nanostructures

by

Zhongjian Zhang

Dissertation

Presented to the Faculty of the Graduate School of

The University of Texas at Austin

in Partial Fulfillment

of the Requirements

for the Degree of

Doctor of Philosophy

The University of Texas at Austin

May 2018

Dedication

This work is dedicated to my parents, Songning Zhang and Mingshou Tao, whose courage and hard work serve as constant motivation for me to fully take advantage of the opportunities I was fortunate enough to receive.

Acknowledgements

None of my scientific work and mental well-being would have been possible without the numerous people who helped and advised me. First and foremost among them is my Ph.D. advisor, Dr. Edward Yu, who seemed to have an infinite well of patience and wisdom that I could draw upon. From his guidance, I learned how to approach new scientific problems as well as how to effectively communicate my results through presentations and written work. His hard work and passion for his students has also been a great example to me on how I would like to approach my career and future work relationships. I also had the pleasure to learn from him in the classroom, where he was an incredible lecturer.

I must also thank my parents; whose work ethic drives me to become the best version of myself. Their constant example serves as my ultimate inspiration. They have also been more than generous in paying for family vacations so I could indulge my wanderlust on a graduate student's budget.

I would also like to thank my dissertation committee, Dr. Emanuel Tutuc, Dr. Sanjay Banerjee, Dr. Deji Akinwande, and Dr. Keji Lai for taking the time to review my work and give me advice on how best to proceed. They and the rest of the faculty at UT have been an invaluable resource in my intellectual development.

I am infinitely grateful to all my current and past labmates, Chris Brennan, Alex De Palma, Gabriel Cossio, Soonil Lee, Li Ji, Heng-Lu Chang, Ping-chun Li, Vaishno Dasika, Chengqing Hu, and Xiaohan Li who were willing to give their time and intellect to help me advance my work. Each one of them took the time to teach me new skills as well as point me in new directions when I hit a scientific wall that I could not break through by myself. I thank Vaishno for teaching me how to use my experimental equipment. I also

have to thank Chris and Gabriel for helping me create samples and run experiments. Finally, Alex was essential to my work through his work on density functional theory simulations. I hope I have partially returned the favor by teaching him what I have learned from my graduate experience.

I would also like to thank all my collaborators that constantly prove to me that quality experimental science is a team event. I have to thank the following people in particular: Dave Dillen, from Dr. Emanuel Tutuc's group who provided me the nanowire samples from which I got my first results and was exceptionally helpful in performing electrical characterization of the nanowires; Rudresh Ghosh, from Dr. Sanjay Banerjee's group, for growing the MoS2 which was used in my strained MoS2 experiments; Kha Tran, from Dr. Elaine Li's group, who exfoliated the WSe2 used in our strain experiments and performed initial optical characterization; Zhaohe Dai, from Dr. Nanshu Lu's group, who was instrumental in helping me understand strain mechanics in 2D materials.

I also must thank the staff at the Microelectronics Center, including James Hitzfelder, Christine Wood, Ricardo Garcia, Joyce Kokes, William James, Johnny Johnson, Risa Hartman and Dr. Marylene Palard, who trained me on equipment, made sure I could buy materials for my research, and keeping the building operational.

Finally, I have to thank all my friends and family in Austin and around the world, who have kept me motivated and hopeful even when my experiments were not going well. This includes my various concert buddies, who helped me indulge my music obsession by going to shows with me, such as Maryli, Denis, Chris, and Ethan. A special thanks to Stefano Larentis, who provided endless quality lunch conversation that was an always welcome respite during long work days.

This work was partially supported by the Center for Dynamics and Control of Materials through the National Science Foundation MRSEC program under NSF Award

Number DMR-1720595. Part of this work was supported by the NSF under Award Number DMR-1311866 and the Judson S. Swearingen Regents Chair in Engineering at the University of Texas at Austin. The majority of the computational resources were provided by the Texas Advanced Computing Center at the University of Texas at Austin. The Microelectronics Research Center is funded by NSF through the National Nanotechnology Coordinated Infrastructure (NNCI).

Tip-Enhanced Raman Spectroscopy of Strained Semiconductor Nanostructures

Zhongjian Zhang, PhD

The University of Texas at Austin, 2018

Supervisor: Edward Yu

Raman spectroscopy can serve as a powerful tool to probe the vibrational modes of solid state materials. By taking advantage of the enhanced electric fields caused by the surface-enhanced plasmon resonance of a noble metal coated atomic force microscopy tip, tip-enhanced Raman spectroscopy can dramatically increase local signal intensity and measurement spatial resolution. In this dissertation, work is presented on conventional and tip-enhanced Raman measurements of various semiconductor nanostructures with a specific focus on analyzing strain and strain related properties in these material systems. We use tip-enhanced Raman to study Ge-$Si_{0.5}Ge_{0.5}$ core-shell nanowires where we observe two distinct Ge-Ge mode Raman peaks that are affected by strain in the core-shell structure. Tip-enhanced measurements show dramatically increased sensitivity to the modes at the interface between the core and shell and a shift in position of this mode due to plasmonic field localization at the tip apex and the resulting change in phonon self-energy caused by increased coupling between phonons and intervalence-band carrier transitions. We also use tip-enhanced Raman spectroscopy to characterize unstrained and strained MoS_2 and show spatial resolution of approximately 100 nm in the measurements.

The strain dependence of the second order Raman modes in MoS_2 reveals changes in the electronic band structure in strained MoS_2 that are manifested through changes in the Raman peak positions and peak area ratios, which are corroborated through density functional theory calculations. Finally, we use conventional Raman spectroscopy to probe uniaxially strained monolayer and three-layer WSe_2. Using mechanical modeling of strain in atomically thin WSe_2 on a stretched elastic substrate, we confirm complete transfer of strain from the substrate to the WSe_2 flakes and analyze the evolution of the Raman spectra with applied uniaxial strain above 1 percent. These studies enable us to experimentally determine the strain induced Raman shift for various Raman modes and to calculate the Grüneisen parameter and strain deformation potential for the first order in-plane Raman mode, with experimental values confirmed with theoretical values calculated using density functional theory.

Table of Contents

List of Tables

List of Figures

Figure 3.14. (a) (Top panel) AFM topography of the linecut shown previously in Figure 3.11b. Raman peak positions of the first order (2^{nd} panel) E2g1 and **(**bottom panel) A1g vibrational modes along the nanopyramid linecut. The insets show schematic drawings of the movement of the atoms for the corresponding vibrational modes. **(b)** Raman peak positions (with error bars) of the second order modes along the line cut (AFM topography shown in the top panel) related to (2^{nd} panel) longitudinal and transverse acoustic phonon scattering of electrons near the K point in the BZ and (third panel) only longitudinal acoustic phonon scattering of electrons near the K point. (Bottom Panel) Raman peak areas (with error bars) of the second order mode associated with LA phonon scattering of excited electrons near the K point in the BZ (black squares) and the second order mode associated with LA phonon scattering of excited electrons near the M point in the BZ (red circles). **(c)** Phonon dispersion for the acoustic phonon modes calculated using DFT simulations for unstrained (blue curve), +0.5% applied hydrostatic strain (red curve), and +1.0% applied hydrostatic strain (orange curve) bilayer MoS_2. The phonon modes represent the out-of-plane (ZA), in-plane transverse (TA), and in-plane longitudinal (LA) acoustic vibrational modes. The high symmetry points (Γ, Q, K, M) are indicated by the green dashed lines. 81

Chapter 1: Introduction

Raman Spectroscopy and Atomic Force Microscopy Background

Within solid state materials, phonons, vibrational modes of the atoms in a crystal, are directly affected by a large set of material characteristics including strain, band structure, defects and, at the nanoscale, dimensions and volume. Raman spectroscopy provides a powerful tool to directly detect these and various other material properties through the interaction of incident light and phonons.[1,2] Fundamentally, Raman spectroscopy and other forms of spectroscopy such as infrared (IR) spectroscopy rely on the fact that molecules vibrate. The molecular bonds between atoms in a molecule can be thought of as springs which vibrate at characteristic frequencies when an input excitation is applied. The vibrational frequency is directly affected by the atoms participating in the vibrational mode, orientation of the bonds, and environmental factors such as temperature and strain. These vibrational frequencies are also quantized into discrete atomic energy levels, with a lowest vibrational energy level for a given molecule and increasing energies for higher-order vibrational modes.

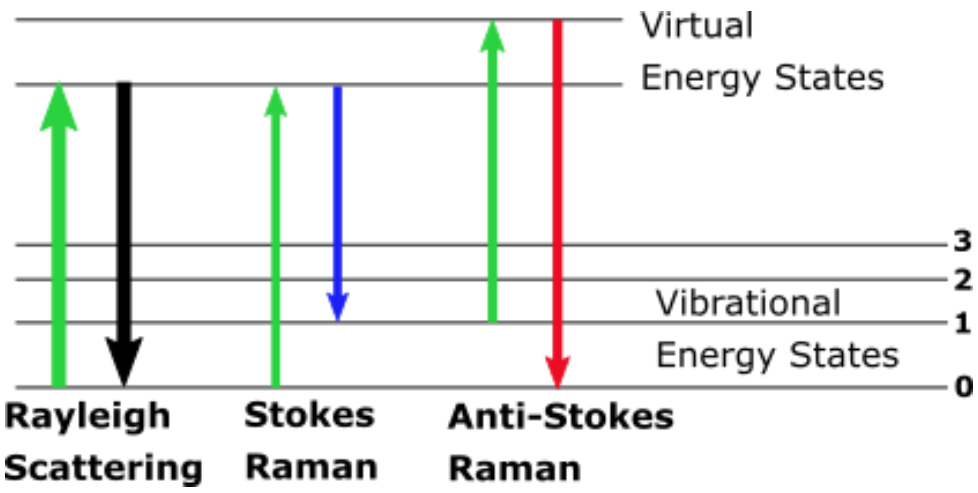

Figure 1.1. Schematic diagram illustrating the energy transitions of the vibrational energy states for Rayleigh scattering, Stokes Raman scattering, and anti-Stokes Raman scattering.

In Raman spectroscopy, the sample of interest is excited by laser photons of a known energy. Most of the photons that scatter from the sample and are measured by the detector are elastically scattered with no change to the kinetic energy of the scattered photons, also known as Raleigh scattering. A small number of the scattered photons are inelastically scattered by vibrational modes in a process known as Raman scattering, where the photons either lose energy (Stokes Raman scattering) or gain energy (anti-Stokes Raman scattering). A schematic illustration of the changes in energy of the molecule and scattered photon are shown in Figure 1.1. In Rayleigh scattering, initial and final vibrational energy states remain the same for a molecule after it absorbs and emits a photon and therefore the energy of the incident and emitted photon also remains the same. In Stokes Raman scattering, the energy of the incident photon is absorbed by the molecule and the molecule is promoted to a higher virtual energy state. The molecule then relaxes to a higher energy vibrational state than its original state and emits a photon of lower

energy, which is called the Raman photon. The energy of the Raman photon is equal to the difference between the incident light and the energy absorbed by the molecule. In anti-Stokes Raman, a molecule in an already excited vibrational energy state absorbs a photon and is promoted to higher virtual energy state, but when it relaxes, the molecule settles to a lower energy state compared to its initial vibrational energy state. The molecule then emits a photon of higher energy than the incident photon. Since very few molecules reside in initial excited energy states, Stokes Raman scattering predominates over anti-Stokes Raman scattering.

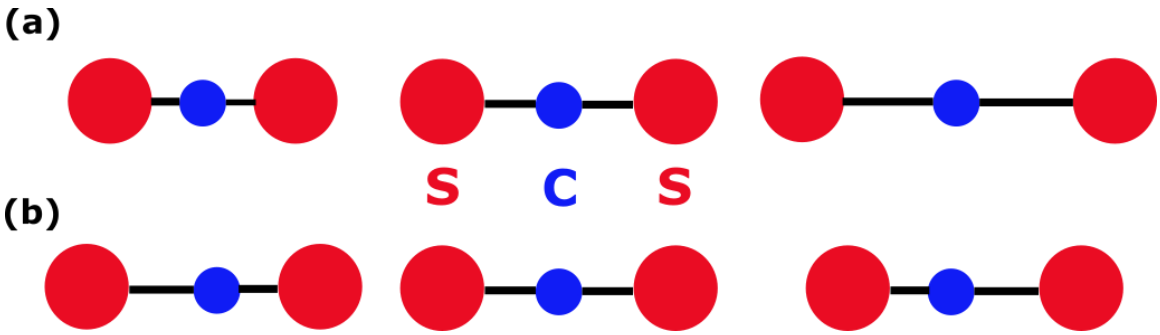

Figure 1.2. Examples of **(a)** Raman-active vibrational modes and **(b)** IR-active vibrational modes in carbon disulphide

Only certain vibrational modes are detectable using Raman spectroscopy. Raman-active vibrational modes cause a change in the polarizability of the electrons in a molecule with the intensity of the Raman scattering for a given mode being directly proportional to the change in the polarizability. Another form of spectroscopy used to probe vibrational modes is infrared (IR) spectroscopy, where vibrational modes are measured through a sample's absorbance of infrared light at different wavelengths. In contrast to Raman spectroscopy, IR-active vibrational modes cause a change in the permanent dipole moment of the molecule. Figure 1.2 shows examples of Raman-active and IR-active vibrational

modes, where in Figure 1.2a, the symmetric stretching-out and stretching-in of carbon disulphide shows a change in polarizability and therefore is Raman-active and has no permanent dipole moment and is therefore IR-inactive. Figure 1.2b shows asymmetric stretching of the same molecule which changes the dipole moment of the molecule and results in no change in the polarizability and is therefore IR-active and Raman-inactive. In general, if a molecule has a center of symmetry, vibrational modes cannot be both Raman-active and IR-active and Raman and IR spectroscopy function as complementary measurement techniques.

Raman spectroscopy can be used to measure a variety of material properties, most commonly, to identify molecules and chemical bonding. Analysis is performed by fitting the Raman spectrum to Lorentzian peaks, with the peak position, peak area, intensity and width of the fitted peak providing important information about the vibrational mode. The spectrum is generally fitted to a Lorentzian because the vibrational modes excited by the incident light have finite lifetime. Since vibrational frequencies are unique to a molecule's bonds, Raman spectroscopy provides a robust and nondestructive fingerprint for molecules, such as separately identifying SiO, Si_2O_2, and Si_3O_3[3] through analysis of the position in frequency of the Raman peaks. Because temperature also directly affects chemical bonding, Raman spectroscopy can also be used to measure changes in temperature and temperature's effects on bonding.[4] Crystal quality in various solid state materials, such as $CuInS_2$[5] and SiC thin films,[6] can also be determined by analyzing the relative change in peak positions and peak intensities in the Raman spectrum. Raman spectroscopy can also directly measures the secondary effects that vibrational modes or phonons have on various other material properties such as carrier densities[7] and electronic band structure[8] in semiconductor materials.

Raman spectroscopy is particularly useful in studying strain in semiconductor materials. Strain inherently affects the bonds between atoms in a molecule and therefore directly affects the vibrational modes that are measured with Raman spectroscopy. Raman allows direct, non-destructive observation of strain with spatial resolutions of approximately 1 μm for conventional measurements. In many material systems, the shift in the Raman peak for a given vibrational mode follows a linear trend as strain is applied and allows determination of various properties of the vibrational modes.[9,10] The spatial resolution also allows measurement of strain in small structures such as thin Si nanostructures[11] and core-shell nanowires.[12]

In addition to the Raman spectra, photoluminescence (PL) spectroscopy can provide further information about structural features in semiconductor materials, such as grain boundaries[13,14] and defects,[15] and can be performed using the same experimental apparatus as Raman spectroscopy. In PL spectroscopy, incident light is absorbed by the sample and provides additional energy to the material through a process called photo-excitation. The excess energy can be dissipated through emission of light or luminescence (PL in the case of photoexcitation). Photo-excitation causes electrons to move into allowed excited states and then return to their equilibrium ground states. When the electrons return to the equilibrium ground states, some of the energy is released through PL. The emitted photons are directly related to the energy difference between the equilibrium and excited states and therefore can be used to directly detect the energy of these transitions. Like Raman spectroscopy, PL spectroscopy can be used for direct chemical detection, such as measuring the concentration of hexaphenylsilole in water.[16] Crucially for semiconductor materials, PL can determine the electronic bandgap energy of material systems such as SiGe[17] and the effects of strain on the bandgap in 2D materials.[18]

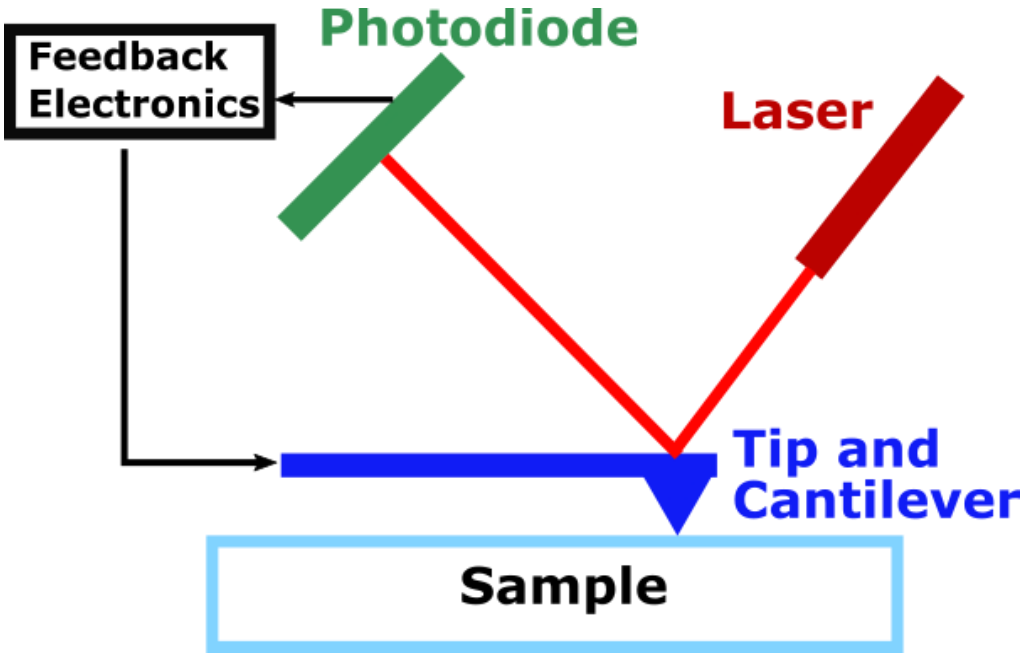

Figure 1.3. Schematic of an example atomic force microscopy experiment using the beam deflection technique.

Scanning probe techniques are broadly used to understand surface topography and other surface-related properties of materials. In scanning probe microscopy, a physical probe is used to scan the surface of the sample. The scanning probe technique used most commonly in our experiments is atomic force microscopy (AFM). AFM allows spatial resolution as high as a fraction of a nanometer, which is orders of magnitude better than optical techniques. In AFM, a sharp tip is attached to the free end of a spring-like cantilever, which is placed in close proximity to the sample surface where forces between the tip and sample leads to a deflection of the cantilever and behaves similarly to a spring governed by Hooke's Law. A detector detects the deflection of the cantilever, a macro-level phenomenon, as it travels over the sample surface and directly relates to the interaction between tip and sample, which is an atomic scale level interaction. Figure 1.3 shows a schematic of an example AFM setup using the beam deflection technique, where

an incident laser is aimed at the cantilever and detected by a photodetector and used to track changes in cantilever deflection, amplitude of the oscillation, and shift in the resonance frequency. The signal from the photodetector is then processed by feedback electronics and used to control the movement of the cantilever and tip. The beam deflection method is widely used in commercial systems because of its high sensitivity and relatively simple operation. Forces that can be measured in AFM include mechanical contact force, van der Waals forces, electrostatic forces, etc. In addition to force, the use of specialized probes can be used to simultaneously measure conductance, temperature, and many other properties at the surface of a sample.

Many imaging modes are used in AFM to measure surface topography of a sample. For our work, two imaging modes are used, contact mode and tapping mode. In contact mode, the tip is dragged along the surface of the sample and the sample surface is measured directly by the deflection of the cantilever or by using the feedback signal required to more generally, maintain a constant interaction force. In ambient conditions, the water in the air causes a liquid meniscus layer to form on the surface of the sample. Due to this liquid meniscus, it is very difficult to keep the probe tip in close enough proximity to the sample for short-range forces to become detectable and prevent the tip from adhering to the sample surface. To overcome this problem, dynamic contact mode or tapping mode was developed. In tapping mode, the cantilever is driven to oscillate at or near its resonant frequency, which is realized by placing a small piezoelectric element in the cantilever holder. The frequency and amplitude of the driving signal are kept constant, which causes a constant amplitude oscillation when the tip is not influenced by external forces such as interaction with the tip. The amplitude of this oscillation ranges from a few to hundreds of nm. When the tip comes close to the surface, surface interactions cause the amplitude of the tip oscillation to change, which is then adjusted by feedback electronics to maintain the

constant tip oscillation. The image is produced through the force of the intermittent contacts of the tip and the sample. Because of the intermittent contact, tapping mode generally causes less damage to both the sample surface and the tip compared to contact mode operation.

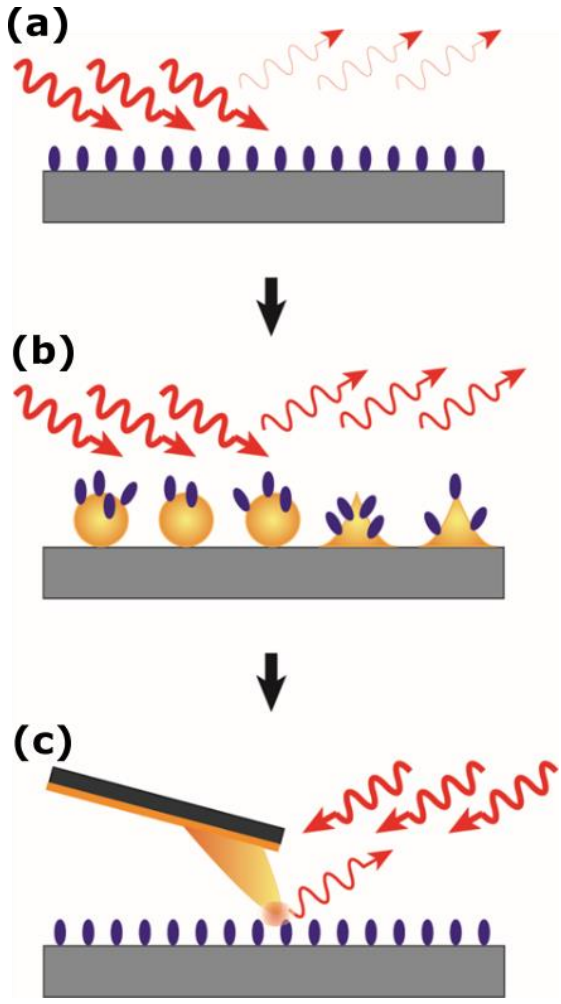

Figure 1.4. Schematic diagrams of **(a)** conventional Raman spectroscopy, **(b)** surface-enhanced Raman spectroscopy, and **(c)** tip-enhanced Raman spectroscopy. The bold red lines represent incident light and the thinner red lines represent scattered light. The purple ovals represent the molecule or sample of interest.

AFM can be combined with specific tip types and experimental configurations to both measure topography as well as other material properties with high spatial resolutions. Examples include magnetic force microscopy (MFM), where a magnetized tip can measure the magnetic structure of the sample surface, and conductive atomic force microscopy (C-AFM), where a conductive AFM probe directly measures current flow. The proximal probe positioning capability, upon which AFM is based, also enables highly localized measurements of optical spectroscopy using the probe tip to concentrate incident electromagnetic (EM) field energy. The extreme localization that can be achieved enables even extremely weak processes, such as Raman scattering, to be detected in nanoscale sample volumes.

In conventional Raman spectroscopy measurements, the spatial resolution that can be achieved is limited by diffraction and by the weakness of Raman scattering processes, which limits signal intensity for small excitation volumes.[1,2] To increase the intensity of the Raman signal, surface-enhanced Raman spectroscopy (SERS) was developed where molecules attached to surface of a roughened metal or metallic nanostructure show dramatically increased Raman intensities, first observed with pyridine on a silver electrode[19] and with enhancement factors of up 10^{10} in single molecule measurements.[20] In SERS, incident photons generate oscillations of surface electron charge density (surface plasmons) on the surface of the metal. These surface plasmons can couple with molecules very close to the surface of the metal and create an efficient pathway to transfer energy to the molecule's vibrational modes and increase the generation of Raman photons. To take advantage of the SERS effect, the laser wavelength chosen must match the localized surface plasmon resonance (LSPR) of the metal surface in order to generate surface plasmons and be much greater in size than the metallic features that molecules lie in close proximity to. Common metals used as substrates for SERS are gold (Au) and silver (Ag)

because they have LSPRs in the visible and near infrared wavelength range and are relatively stable in air. In addition to any EM enhancement, chemical enhancement can occur when a molecule coordinates with the surface of the metallic particle and forms charge transfer states with the energy levels of the metal.[21] The total SERS enhancement combines both the EM enhancement and chemical enhancement. SERS has been demonstrated to be effective in wide range of applications such as biosensing[22] and detecting trace chemicals for the purposes of art preservation.[23]

Taking advantage of the basic concepts learned from SERS, tip-enhanced Raman spectroscopy (TERS) allows dramatic improvement in spatial resolution when compared to conventional Raman spectroscopy by employing a metallic nanostructure at the apex of an atomic force microscope probe tip to induce plasmonic localization and amplification of incident light in the immediate vicinity of the probe tip.[24–26] The plasmonic enhancement induced by the metallic probe also allows near-field PL measurements to be performed with significantly enhanced spatial resolution.[27] The use of a precisely controlled probe tip instead of randomly dispersed metallic structures allows precise positioning of the tip on specific features of interest. In addition, the combination of atomic force microscopy (AFM) and light scattering spectroscopy techniques in a single measurement apparatus allows information concerning structural, electrical, or other properties that can be probed at the nanoscale using AFM and related techniques to be correlated with that gleaned from TERS and nano-PL measurements that can be performed with similar spatial resolution. Also, by placing samples on metal substrates of the same material as the plasmonically enhanced tip, a plasmonic gap mode enhancement can occur that can further increase signal enhancement.[28]

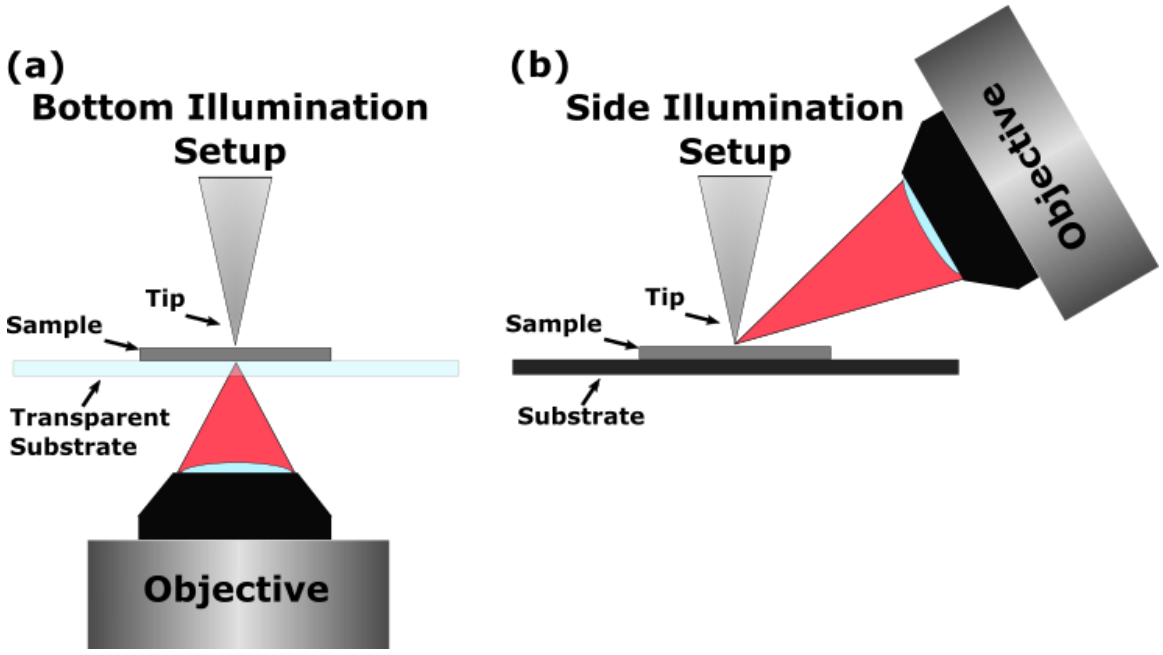

Figure 1.5. TERS experimental geometries: **(a)** Bottom illumination geometry which requires a transparent substrate. **(b)** Side illumination geometry with fewer substrate constraints.

There are multiple possible experimental geometries for TERS, with the two most commonly used being the bottom illumination and side illumination geometries. Bottom illumination is the easiest setup to build and was the first experimental geometry realized for TERS.[25] However, because of the illumination direction, the substrate that the sample is lying on must be transparent, as shown in Figure 1.5a. To overcome the substrate transparency constraint, a side-illumination setup was developed which allows a much wider variety of substrates, as shown in Figure 1.4b. The use of non-transparent substrates allows metal substrates that match the plasmonic properties of the tip to be used which can generate significantly greater enhancement.

Resonance Raman (RR) scattering, in which the excitation wavelength is tuned near the energy of electronic transitions, probes additional changes in the electronic and physical structure not normally detected in conventional Raman scattering.[1] The intensity of certain

vibrational modes become significantly greater and allow access to additional information about the sample of interest. RR is particularly useful for 2D materials since many of the excitonic transitions for these materials occur near the energy of the excitation laser. When the laser excitation wavelength used in TERS also matches the excitation wavelength of electronic transitions, an experiment can take advantage of both the enhancement from TERS as well as RR.[8]

DENSITY FUNCTIONAL THEORY BACKGROUND

To better understand our experimental results, we have used density functional theory (DFT) to calculate the bandstructure and phonon behavior for multiple material systems. DFT simplifies a many-electron system so that it becomes computationally tractable by using functionals, which are functions of the spatially dependent electron density. When using this approach to treat many-body electronic structure problems, the nuclei of the molecules are treated as fixed in position, resulting in a static external potential V in which the electrons move. An electronic state is describe by a wavefunction $\Psi(\overrightarrow{r_1}, \cdots, \overrightarrow{r_N})$ that satisfies the many-electron time-independent Schrödinger equation:

$$\widehat{H}\Psi = \left[\hat{T} + \hat{V} + \hat{U}\right]\Psi = \left[\sum_i^N (-\frac{\hbar^2}{2m_i}\nabla_i^2) + \sum_i^N V(\vec{r_i}) + \sum_{i<j}^N U(\vec{r_i}, \vec{r_j})\right]\Psi = E\Psi, \qquad (1.1)$$

where for an N-electron system, $\widehat{H}$ is the Hamiltonian, $\hat{T}$ is the kinetic energy, $\hat{V}$ is the potential energy from the external field due to the positively charged nuclei, $\widehat{U}$ is the electron-electron interaction energy. Solving for the Schrödinger equation does not scale well with increasing electrons, with $3N$ variables for N electrons. To simplify this problem, DFT instead solves for an approximately equivalent system of single electron

states. The Schrödinger equation is approximated using the Kohn-Sham equations for an auxiliary non-interacting system:

$$\left[-\frac{\hbar^2}{2m}\nabla^2 + V_s(\vec{r})\right]\varphi_i(\vec{r}) = \varepsilon_i\varphi_i(\vec{r}), \tag{1.2}$$

where V_s is the effective potential and the orbitals φ_i are used to produce the electron density, which is the key variable to be solved in DFT. First, the lattice structure is optimized by adjusting the atomic positions and lattice parameters to minimize the forces and stresses. After a relaxed lattice structure is obtained, the electron density is calculated using a self-consistent solution, where φ_i is dependent on the electron density and the electron density is dependent on φ_i.

To solve for the phonon dispersion, we use density functional perturbation theory (DFPT), where we can calculate the frequencies for the phonon modes by solving for the first derivative of the electron density which is equivalent to solving for the second derivative of energy. In our DFPT calculations, we add an additional small perturbation to the lattice structure by altering the atomic positions of the atoms to simulate the effect of strain on the phonons.

SEMICONDUCTOR NANOSTRUCTURE BACKGROUND

TERS can be particularly useful for low dimensional semiconductor materials such as nanowires and nanowire heterostructures due to the variations in composition, bonding, strain, and carrier density that are present at the nanoscale. Among these, group IV nanowires and nanowire heterostructures are of current interest for a broad range of applications including field-effect transistors with enhanced carrier mobility[29,30], superconducting devices[31,32], quantum computing[33,34]; engineered thermal transport[35,36],

and thermoelectrics[37,38]. In Ge-Si_xGe_{1-x} core-shell nanowires, the lattice mismatch between the Ge core and Si_xGe_{1-x} shell provides an opportunity to characterize the correlation between strain and nanowire dimensions at the nanoscale.[39–41] In addition, the valence-band offset at the Ge-Si_xGe_{1-x} interface leads to formation of a quantum-confined hole gas at that interface, and consequently an opportunity to characterize the interactions between optical phonons and intra and inter-valence band transitions enabled by the high hole densities present at the Ge-Si_xGe_{1-x} interface, similar to those that have been observed to occur in heavily doped bulk p-type Ge.[7,42]

In addition to one dimensional materials such as nanowires, the high spatial resolution and precise positional control attained in TERS is especially useful to characterize materials such as atomically thin two-dimensional transition metal dichalcogenides (2D TMDs), because of the nanoscale variations in strain, layer thickness, and electronic band structure that can be present. 2D TMDs can also sustain large elastic deformations before rupture of the material[43,44], which allows realization of localized regions of high strain. Among 2D TMDs, molybdenum disulfide (MoS_2) shows a large intrinsic bandgap that makes it suitable for various electronic and optoelectronic devices.[45–47] The electronic band structure of MoS_2 is also highly sensitive to strain,[18] which highlights the importance of localized detection of strain when designing devices. Strain engineering has been employed, for example, to demonstrate efficient quantum emitters in other TMDs, such WSe_2 and WS_2, with enhanced PL intensity.[48,49] Characterization of nanoscale strain distribution is also relevant to investigation of electromechanical effects in atomically thin TMDs.[50–52] Conventional Raman measurements on MoS_2 have previously been used to measure changes in strain and band structure through Raman and PL measurements but often with low spatial or spectral precision.[10,18] Specifically in MoS_2,

RR scattering reveals a complex variety of second-order Raman features that can yield additional information about the physical properties and band structure.[53,54]

In addition to MoS_2, we have also used Raman spectroscopy to study in detail the effects of strain on the vibrational modes of tungsten diselenide (WSe_2) for which little information on the strain dependence of phonon modes is currently available. WSe_2 has been used as the channel material in high mobility transistors.[55,56] Theoretical work has shown that mechanically straining WSe_2 directly affects properties such as the electronic band structures.[57,58] Monolayer WSe_2 is a direct band gap semiconductor[59], and combined with locally induced strain, has demonstrated quantum emission at low temperatures.[48,49] Because of the direct influence of changes in the lattice structure on electronic and optical properties in WSe_2 and other TMDs, device engineering in these materials will require precise measurements of mechanical strain.

TIP-ENHANCED RAMAN EXPERIMENTAL SETUP

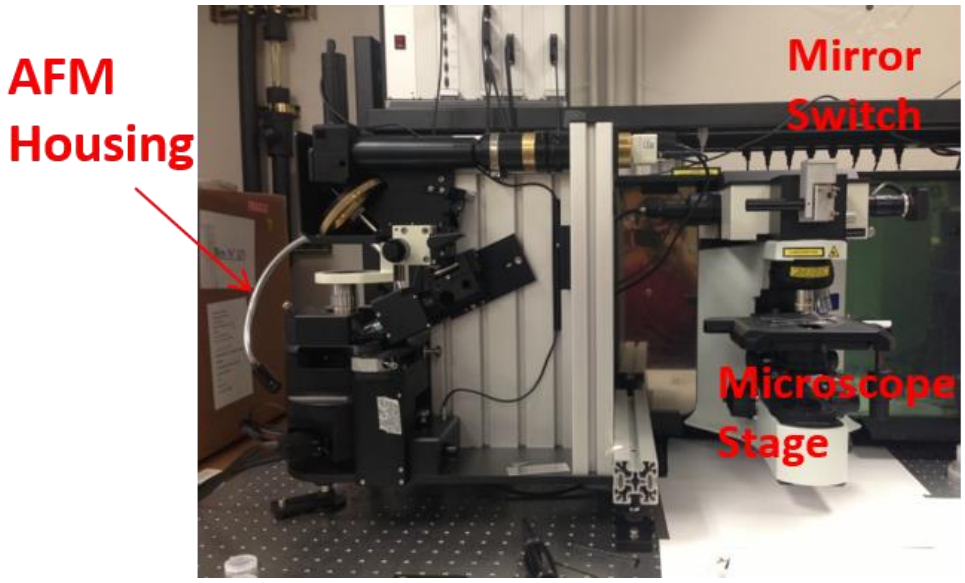

Figure 1.6 Image of the Raman spectrometer, microscope stage, and AFM housing

TERS measurements were obtained using a Horiba Jobin Yvon LabRAM confocal Raman system with a backscattering geometry in conjunction with an AIST-NT Omegascope atomic force microscope that couples with the Horiba setup using a system of external mirrors and lenses to align the laser with the probe tip. The experimental setup is shown in Figure 1.6. In the Raman system, there is a notch filter along the backscattered beam path to the detector to filter out the elastically scattered light at the excitation wavelength. Before reaching the detector, the backscattered beam hits a diffraction grating. A diffraction grating is composed of evenly spaced, narrow grooves which reflect light at different angles based on the energy or wavelength of the incident photon. The angle of the diffracted light is governed by the following equation:

$$\theta_m = \arcsin(sin\ \theta_i - \frac{m\lambda}{d}), \tag{1.3}$$

where θ_m is the angle between the diffracted ray and the grating's normal vector, θ_i is the angle of the incident photon, *m* is and integer representing the propagation mode of interest, λ is the wavelength of the incident photon, and d is the spacing between grooves. By separating the light predictably based on energy, the detector can accurately determine the energy spectrum of the incident light. We use both 300 and 1800 grooves per mm density gratings where the former allows high signal throughput, which is especially useful during alignment, while the latter gives superior spectral resolution. The detector used in the Horiba system was an Andor charge coupled device (CCD), where the detection area on the CCD was limited to a smaller area to further improve spatial resolution.

AFM measurements were performed using an AIST-NT Omegascope. When scanning the topography of the sample, tapping mode operation was used with a tapping amplitude of 15 to 20 nm. The unique feature of the AIST-NT Omegascope is that during

scanning, instead of the tip moving which is common to most other AFM systems, the sample moves instead. Samples are mounted onto metal SEM disks, which are then held in place on the sample stage using a magnet. This allows the system to maintain laser to tap alignment throughout the entire measurement process. Additionally, tracking of the probe tip is performed with infrared lasers so that the tracking lasers are significantly separated in frequency from the excitation lasers used in Raman experiments.

All TERS measurements were performed using laser excitation at a wavelength of 633nm, which takes advantage of the surface enhanced plasmon resonance of Au. For conventional Raman measurements performed using the standard microscope, the laser was focused using either a 20 X, 50 X, or 100 X objective yielding a spot size of ~1 μm for measurements performed with the 100 X objective. Both the conventional Raman and TERS measurement signals follow the same optical path back to the detector. For TERS measurements, a mirror switch was used to send the same excitation laser to a set of external mirrors that illuminate the AFM tip in the AIST-NT Omegascope. A 20 X or 100 X long working distance side objective side illuminates our AFM tip at an angle of 30 degrees relative to the surface of the sample with a spot size of ~5 μm for the 20 X objective and ~1 μm for the 100 X objective. We have chosen a side illumination setup for our experiments so we can take advantage of the significantly greater number of allowed substrates when compared to a bottom illumination system. Side illumination specifically allows placement of samples on Au substrates, which are non-transparent and therefore cannot be used in a bottom illumination geometry, and create significantly greater enhancement due to the creation of a plasmonic gap mode between the substrate and the tip. Because the sample stage moves instead of the tip, optical alignment is maintained throughout. Even though long working distance objectives are used, the working distance of the 100 X objective is still only 13 mm which limits sample size. TERS Raman spectra

were collected using both tapping mode and contact mode configurations of the AFM with various oscillation amplitudes for tapping mode measurements. Contact mode allows the tip to be placed in closest proximity to the sample and achieve the highest level of signal enhancement.

Various AFM tips were used for the TERS experiments including tips that were coated with metals by our lab and those that have been commercially purchased. The tips produced by our lab start by coating Bruker OTESPA tips with a chromium (Cr) and Au metal bilayer using electron beam metal deposition. These tips show decent enhancement but had low AFM scanning endurance due to poor adhesion of the metal layer on the tip. Commercially purchased tips included Au Opus tips from Micromasch and Au tips purchased from Horiba. Micromasch tips had similar geometry to the OTESPA tips and showed similar enhancement performance but superior scanning stability due the stability of the metal adhesion. The Horiba tips had the best Raman enhancement and high scanning stability. The issue with all the tips is that the Raman enhancement was not very stable beyond one to two weeks of use.

In addition to the Horiba Raman system, we also performed conventional Raman and photoluminescence experiments with a Renishaw inVia Raman system with an excitation wavelength of 532 nm. This Raman system has a precision stage that made performing certain conventional Raman measurements more straightforward.

Chapter 2: Strain and Hole Gas Induced Raman Shifts in Ge-Si_xGe_{1-x} Core-Shell Nanowires[A]

INTRODUCTION

TERS offers unique capabilities to characterize mechanical and electronic characteristics of nanowires at the nanoscale. As discussed in Chapter 1, Group IV nanowires and nanowire heterostructures are being studied for applications such as field-effect transistors[29,30], superconducting devices[31,32], quantum computing[33,34]; engineered thermal transport[35,36], and thermoelectrics[37,38]. Ge-Si_xGe_{1-x} core-shell nanowires provide a platform to correlate strain and nanowire dimensions, due to the lattice mismatch between the Ge core and Si_xGe_{1-x} shell .[39–41] The valence-band offset at the Ge-Si_xGe_{1-x} interface creates a quantum-confined hole gas at that interface, which allows probing of interactions between optical phonons and intra and inter-valence band transitions.

In TERS studies of Ge-Si_xGe_{1-x} core-shell nanowires, we have locally observed changes in strain, interactions between phonons and mobile carriers, and the influence of tip-induced field localization on Raman spectra. Our results demonstrate that Raman spectra obtained using TERS combined with structural information provided by AFM topographic imaging can be used to characterize strain distributions at the nanoscale in Ge-Si_xGe_{1-x} nanowire core-shell heterostructures as functions of core and shell dimensions. We also observe clear evidence in Raman spectra obtained by TERS of Raman peak shifts associated with interactions between Ge-Ge vibrational modes and intra and inter-valence-band transitions within the quantum-confined hole gas at the Ge-Si_xGe_{1-x} interface, with the improved spatial resolution in the radial direction afforded by TERS enabling more detailed characterization and analysis compared to prior observations of asymmetrical

[A] [1] Z. Zhang, D.C. Dillen, E. Tutuc, and E.T. Yu, Nano Lett. **15**, 4303 (2015). Zhongjian Zhang designed the experiment, performed Raman spectroscopy and atomic force microscopy measurements, analyzed the collected data, and wrote the manuscript.

broadening of Raman spectra in Ge-Si_xGe_{1-x} core-shell nanowires.[60] Finally, we combine computational modeling with TERS measurements to demonstrate that proximity of a metallized probe tip during the TERS measurements leads to alterations in the spatial distribution of the excitation field that enhance phonon-carrier interactions and increase the Raman peak shift associated with these interactions as the probe tip is brought into close proximity to the nanowire surface.

NANOWIRE GROWTH AND EXPERIMENTAL DETAILS

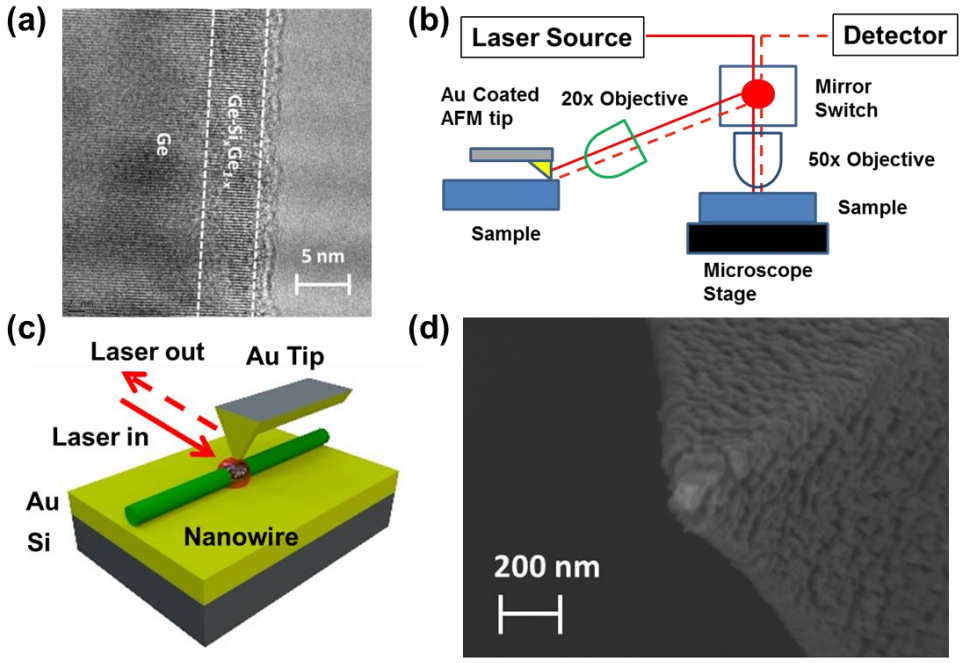

Figure 2.1. (a) TEM image of Ge-Si_xGe_{1-x} core-shell nanowire. **(b)** Schematic diagram of TERS and conventional Raman measurement schemes. **(c)** Schematic diagram of our TERS experimental geometry for TERS measurements of Ge-$Si_{0.5}Ge_{0.5}$ core-shell nanowires. **(d)** SEM image of Cr/Au coated AFM tip used for TERS measurement.

Nanowire samples were grown on Si (111) wafers using Au nanoparticles as catalysts for Vapor Liquid Solid (VLS) growth of the Ge nanowire cores.[61] During VLS

growth, the nanowires taper from base to tip due to a small amount of conformal chemical vapor deposition of Ge on the existing nanowire which results in a core thickness that ranges from 25-55nm. After growth of the Ge core, epitaxial shell growth was done using an ultra-high-vacuum chemical vapor deposition (UHVCVD) process. Typical nanowires were ~6μm long with the nanowire core axis along the [111] direction. Nanowire dimensions and compositions were verified using transmission electron microscopy (TEM) and energy dispersive x-ray (EDX) spectroscopy.[12] Figure 2.1a shows a TEM image of a core-shell nanowire that confirms constant shell thickness and high overall growth quality.

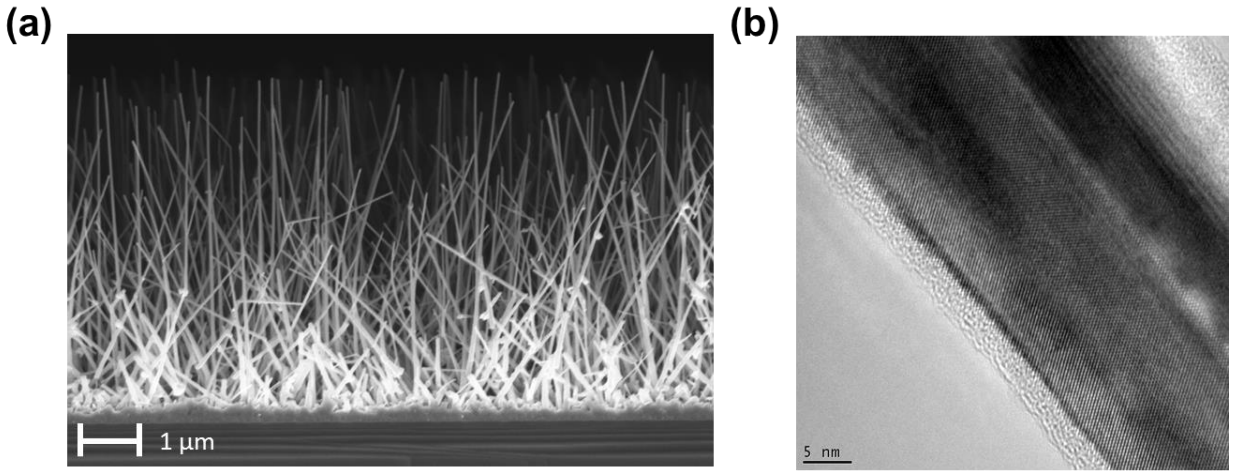

Figure 2.2. **(a)** A 90 degrees SEM cross sectional image of Ge-$Si_{0.5}Ge_{0.5}$ core-shell nanowire growth on Si(111) substrate. **(b)** TEM image showing lattice fringes of the core-shell nanowire

A SEM cross sectional image of the as-grown nanowire and an additional TEM image of nanowire lattice fringes are shown in Figure 2.2a and 2.2b, respectively. The orientation of the substrate has a minimal effect on the axial direction of the nanowires. The axial direction is primarily controlled by surface energetics and is consistently [111] for the diameter range under investigation. The nanowires do grow epitaxial to the substrate and have a predominately vertical orientation.

The Si_xGe_{1-x} shell has a smaller lattice constant than the Ge core; therefore the core region is compressively strained. For the core and shell dimensions and compositions employed here, all the nanowire heterostructures are expected to be coherently strained, based on a prior analysis of strain energetics,[62] with the Ge core region being under compressive strain in both the axial and radial directions.

Figures 2.1b and 2.1c show schematic diagrams of the conventional Raman and TERS experimental setups and the tip and sample geometry for the TERS measurements. In preparation for TERS measurements, the Ge-$Si_{0.5}Ge_{0.5}$ core-shell nanowires were released from the Si (111) growth substrate by sonicating in ethanol, and dispersed on an Au-coated SiO_2/Si (001) substrate by drop casting. The 100nm thick Au layer blocks any signal from the underlying SiO_2 and Si layers.

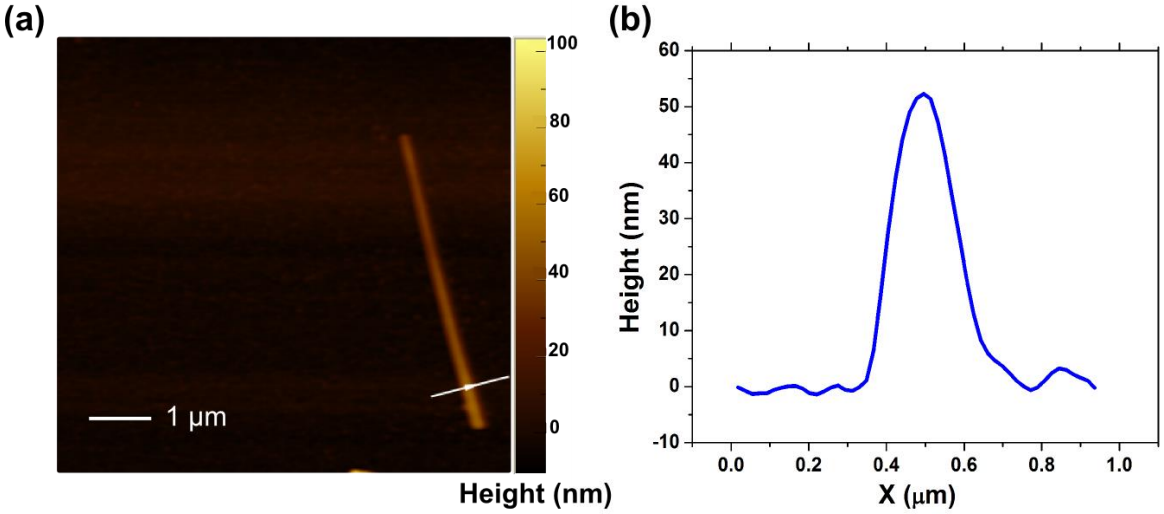

Figure 2.3. (a) Topographic AFM image of a typical Ge-$Si_{0.5}Ge_{0.5}$ core-shell nanowire dispersed on Au substrate. **(b)** Height profile of the nanowire along the line indicated by the arrowed white line in **(a).**

Nanowires characterized by TERS are first located by AFM topographic scanning, with the measured nanowire height being used to determine their diameter, as shown in

Figure 2.3. A typical measured nanowire is separated from other nanowires by at least a few microns. Diameter measurements were also confirmed using scanning electron microscopy (SEM).

The AFM probe tips used for TERS were Si tips with the visible apex of the tetrahedral tip located at the end of the cantilever, and were coated with a metal bilayer consisting of 35nm Cr/140nm Au using electron beam deposition. Figure 2d shows a SEM image of a Cr/Au-coated probe tip, from which we deduce that the radius of curvature of metallized probe tips used in the TERS measurements is approximately 50nm. TERS measurements were performed with the AFM operating in intermittent contact mode with an oscillation amplitude ranging from 3nm to 20nm.

NANOWIRE ELECTRICAL CHARACTERIZATION

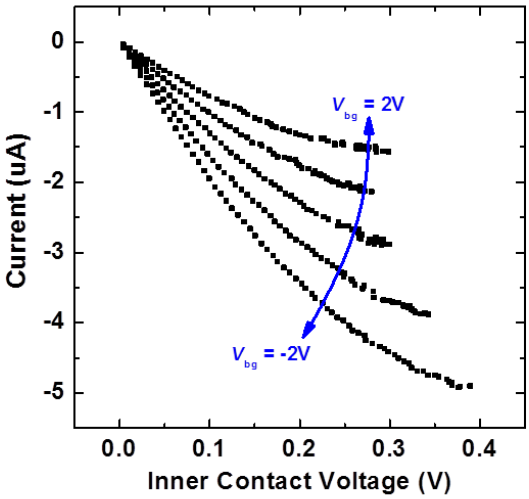

Figure 2.4. Four point electrical measurements used to determine nanowire carrier density.

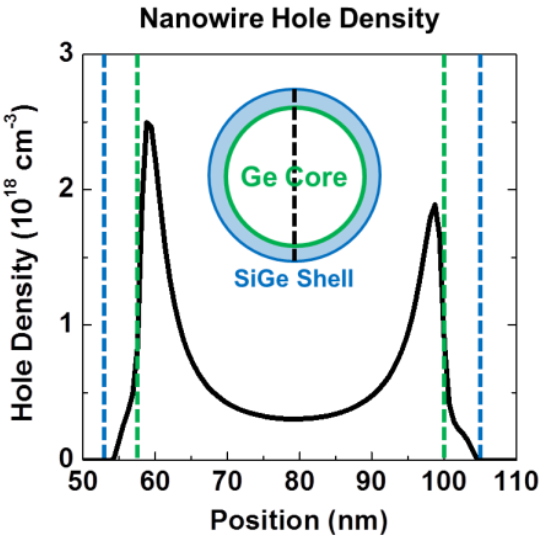

Figure 2.5. Simulated hole density at zero back gate voltage with full quantum solution in a Ge-$Si_{0.5}Ge_{0.5}$ core-shell nanowire. The following parameters were used: core thickness, d = 42 nm, a shell thickness, T_{sh} = 5 nm, a core/shell valence band offset = 130 meV, and a back-gate SiO_2 thickness = 54 nm. The blue and green dashed lines indicate the border of the nanowire and the core-shell interface, respectively. The dashed black line in the inset shows the plane from which the hole density and valence band edge energy correspond with. Peak hole density in core is 2.5×10^{18} and 1.9×10^{18} cm^{-3} at the bottom and top of the NW, respectively.

In order to probe the intrinsic nanowire resistivity without contributions from a finite contact resistance, electrical measurements were performed on a back-gated four-point device with a 54 nm SiO_2 dielectric and boron implanted regions under Ni contacts, with results shown in Figure 2.5 (the nanowire channel remains undoped). Results yield a room temperature conductance of 1.39×10^{-5}A/V at zero gate voltage, and a field-effect mobility of 600 cm^2/V·s for a device with channel length of 1100nm, Ge core diameter of 42nm, and $Si_{0.5}Ge_{0.5}$ shell thickness of 5nm. The field-effect mobility was extracted using the gate dependence of the intrinsic conductance: $\mu = (dG/dV_{bg})L_{ch}/C_{ox}$, where C_{ox} = 5.56×10^{-13} F/cm is the back-gate capacitance per unit length as determined by Sentaurus TCAD simulations (Synopsys). The dependence of conductance on gate voltage indicated

that the nanowires are p-type, and the measurement of conductance at zero gate bias combined with Sentaurus TCAD simulations yields a peak hole concentration near the interface of 2×10^{18} cm^{-3}.

To shift the threshold voltage to match experimental data ($V_{th} \approx 4.5$V), 2×10^{18} cm^{-3} boron doping was added to shell. The core remains undoped. Band offsets used for the simulation were taken from previous results.[30] The electric field approximation for the triangular well underestimates the electric field closer to the interface; however, this is offset by the overestimation of the barrier height, which is assumed to be of infinite height, in the triangular well approximation when in actuality the barrier is significantly smaller.

NANOWIRE RAMAN BACKGROUND

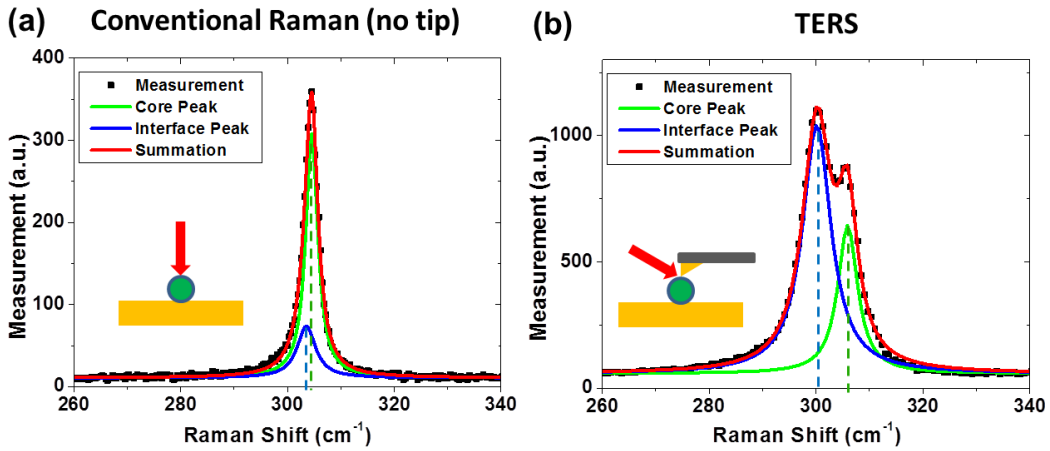

Figure 2.6. Raman spectra from **(a)** conventional Raman measurements and **(b)** TERS measurements. Both spectra are fitted to two Lorentzian peaks: one in green for the core region and one in blue for the interface region. The sum of the two peaks is shown in red in both plots, and shows excellent agreement with the measured spectra.

Figure 2.6 shows Raman spectra for the Ge-Ge vibrational mode obtained from Ge-$Si_{0.5}Ge_{0.5}$ core-shell nanowire heterostructures both using the conventional Raman spectroscopy apparatus and via TERS. In each case, the spectra are fitted to two Lorentzian

peaks. One peak, shown in green, corresponds to Ge-Ge vibrational modes in the Ge core of the nanowire. The other, shown in blue, is associated with Ge-Ge vibrations in the Ge nanowire core region near the Ge-$Si_{0.5}Ge_{0.5}$ interface, at which a quantum-confined hole gas is present. Prior studies of Raman spectra in heavily doped p-type Ge have demonstrated that coupling between the Ge-Ge vibrational mode and intra- and inter-valence-band transitions leads to an asymmetric broadening of the Ge-Ge Raman peak as well as a shift in peak position to smaller wave numbers.[7,42] In addition, behavior similar to that shown in Figure 2.6a has been observed in earlier Raman spectroscopy studies of Ge-Si core-shell nanowires, and attributed to a superposition of Raman peaks from the Ge nanowire core and the vicinity of the quantum-confined hole gas at the core-shell interface.[60]

In comparing the conventional and tip-enhanced Raman spectra shown in Figure 2.6, we observe that the amplitude of the peak attributed to Ge-Ge vibrational modes near the core-shell interface (hereafter referred to as the "interface peak") is substantially larger, compared to the peak associated with Ge-Ge vibrations in the Ge core (hereafter referred to as the "core peak"), in the TERS measurement, indicating that TERS yields a stronger relative signal from the interface region. In addition, the separation between the core and interface peaks is significantly greater in the TERS measurement than in the conventional Raman spectrum. We attribute the increase in peak separation in the TERS measurement to an enhancement in coupling between the Ge-Ge vibrational mode and a combination of intra and inter-valence-band transitions that occur due to the altered spatial distribution of the electromagnetic field in the vicinity of the probe tip under laser illumination.

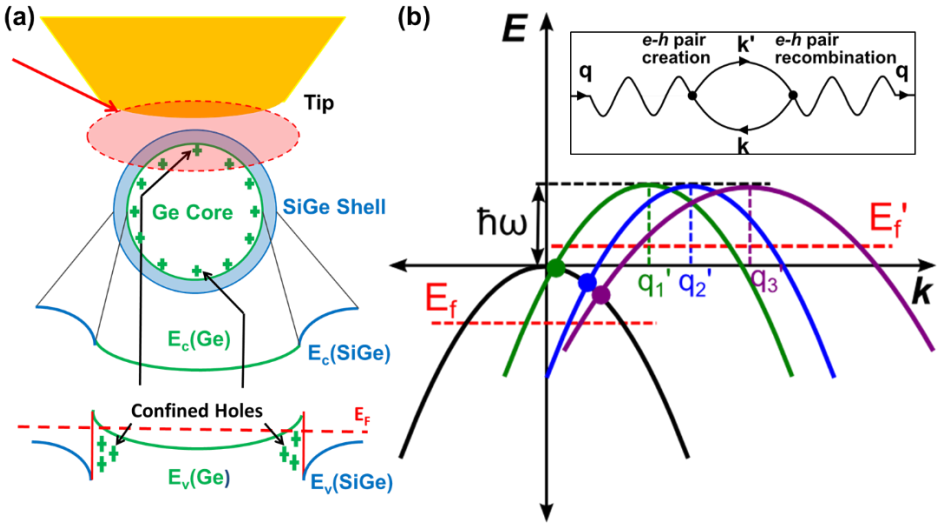

Figure 2.7. (a) Schematic diagram of the nanowire band structure as it relates to the TERS experimental setup. **(b)** Schematic band diagram showing energy and momentum conservation constraints for the carrier transitions within the valence band. The black parabola represents the initial band dispersion with an initial Fermi level position, E_f. The colored parabolas represent the shift in energy, $\hbar\omega$, and shifts in momentum, q_1',q_2', and q_3', caused by different carrier transitions with the Fermi level at E_f'. The green and blue parabolas indicate intravalence band transitions with two different momentum shifts, q_1' and q_2'. The purple parabola with a shift in momentum q_3' represents a intervalence band transitions between bands with different band curvatures. The inset shows a schematic diagram of the phonon mediated *e-h* pair creation and recombination that alters the self-energy of the phonon.

Figure 2.7a shows a schematic band edge energy diagram of the nanowire heterostructure. The interface region in the Ge core contains a two dimensional hole gas (2DHG) with a much higher hole concentration than in the rest of the core. Based on electrical measurements and transport simulations, a peak carrier density of approximately 2×10^{18} carriers cm^{-3} occurs in the interface region, which is below the threshold in p-type bulk Ge for observing either a red shift in the Ge-Ge Raman peak position or a broadening in the peak when compared to intrinsic bulk Ge.[7,42] However, the geometry of the 2DHG in the interface region of the nanowire results in a significantly altered valence-band

structure, compared to the bulk case, where factors such as the greater curvature of the first and second heavy hole subbands would result in a greater number of occupied and unoccupied valence states near the Fermi energy. A greater number of occupied and unoccupied states near the Fermi energy would allow for coupling between intra and inter-valence-band carrier transitions and the Ge-Ge phonon mode comparable to that of much more heavily doped bulk Ge, which would be observed through the similar peak shift and broadening of the Ge-Ge mode Raman peak.

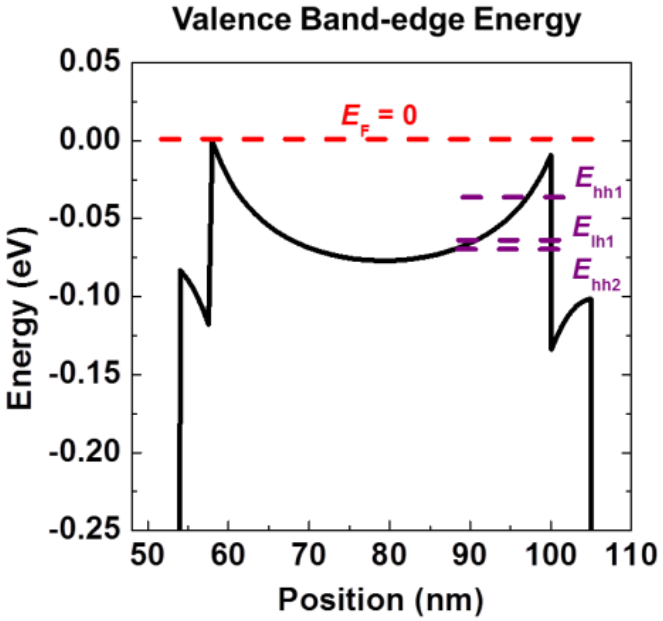

Figure 2.8. Simulated band edge energy diagram for the valence band for the same core-shell nanowires. The dashed red line indicates the Fermi level. The top of the nanowire is the region closest to the tip apex and therefore of most interest. The dashed purple lines indicate confinement energies for the first and second heavy hole bands, E_{hh1} and E_{hh2}, and the first light band, E_{lh1}. The confinement energies were approximated by modeling the interface region as a triangular well. The average electric field used in the triangular well approximation is taken from the band edge energy diagram over 12nm towards the center of the Ge core from the interface.

For bulk Ge, the heavy hole effective mass is $0.33m_e$, and the light hole effective mass is $0.043m_e$.[42] To calculate the effective masses for the 2D hole gas in the interface region of the core shell nanowire, we assume a triangular quantum well and use the experimentally determined Luttinger parameters, $\gamma_1 = 13.35$ and $\gamma_2 = 4.25$[63], which results in a transverse heavy hole effective mass of $\frac{m_e}{\gamma_1+\gamma_2} = 0.0568m_e$, and a light hole transverse effective mass of $\frac{m_e}{\gamma_1+\gamma_2} = 0.1099m_e$. When comparing the two valence band curvatures, the heavy hole band in the nanowire case has significantly more curvature than the heavy hole band in the bulk case, and the light hole bands have comparable curvature in both cases. The much greater curvature would indicate a higher number of occupied and unoccupied states for carrier transitions to occur. Based on a carrier concentration of 2×10^{18} cm^{-3}, the sheet density for the 2DHG at the nanowire interface would be 1.59×10^{12} cm^{-2}, which would only fill the first heavy hole subband of the valence band. The Fermi level is then below the top of the valence band, which allows intervalence-band transitions to occur between the subbands.[64]

The shift and broadening of the Raman peak in heavily p-type Ge can be explained by considering the phonon mode excited in the Raman scattering process and the interaction with the 2DHG at the core-shell interface through particle-vacancy creation and recombination processes. For simplicity we illustrate this interaction in Fig. 2.4b for the case of a non-degenerate parabolic band; a quantitative description should take into account the degeneracy and full dispersion of the Ge valence band including confinement effects. For a process of particle-vacancy creation through phonon absorption, the energy and momentum conservation conditions may be written as

$$\hbar\omega = \frac{\hbar^2 k'^2}{2m} - \frac{\hbar^2 k^2}{2m} \quad , \tag{2.1}$$

$$\mathbf{k}' = \mathbf{k} + \mathbf{q}, \tag{2.2}$$

respectively, where ω is the phonon frequency, **k** and **k'** are the wavevectors for the initial and final electronic states, **q** is the phonon wave vector, and m is the hole effective mass. Assuming plane wave incident and scattered radiation, the phonon wave vector **q** is given, due to momentum conservation, by[7]

$$q = \frac{4\pi}{\lambda} n(\lambda), \tag{2.3}$$

where λ is the free-space wavelength of the incident light and $n(\lambda)$ is the refractive index of the nanowire material as a function of wavelength. Coupling of phonons to electronic transitions between valence-band states can occur through the deformation potential mechanism, which is directly responsible for the self-energy of the phonons.[7,65] When the phonon frequency is comparable to the free-carrier redistribution time, as is the case for optical phonons that are of interest here, the electron-phonon interaction must be treated quantum mechanically, and can allow for the decay of phonons into hole excitations within the valence bands.[66] These free-particle excitations take place due to transitions of electrons from occupied to unoccupied valence-band states near the Fermi energy. If (i) both interacting elementary excitations are Raman active, as is the case with transverse optical (TO) phonons and electron-hole pairs, (ii) the phonon energy coincides with the energy of the electronic excitations, and (iii) momentum conservation among the phonon momentum and the initial and final electronic state momenta is satisfied, the Raman peak associated with the phonon mode may broaden asymmetrically due to the Fano effect.[7]

In general, Fano resonances arise due to interference between the scattering amplitudes from a discrete excitation and a continuum of transitions,[67] which in this case are the optical phonon and the continuum of electronic transitions within the Ge valence band, respectively. In Raman measurements, coupling between phonons and such transitions can occur when both energy and momentum conservation are satisfied, which in turn requires very high hole concentrations. Figure 3b shows a schematic illustration of the momentum and energy conservation constraints on carrier transitions within the valence band. A carrier transition shifts the energy and momentum of the initial parabolic valence band dispersion, shown in black with Fermi energy E_f, to a new position, shown with the colored parabolas with Fermi energy E_f', depending on the phonon frequency, ω, and wavevector, q. A carrier transition is allowed if the intersection point of the original parabola and the shifted parabola is higher in energy than E_f, which indicates an initially occupied hole state, and lower in energy than E_f', which indicates a final vacant hole state. The energy and momentum conservation constraints for allowed transitions apply to both intra and intervalence-band transitions, with changes in dispersion of the bands for the initial and final states implicitly modeled within the allowed intersection points of the original and final parabolas. For Ge-Si_xGe_{1-x} core-shell nanowires, the elevated hole concentration in the quantum-confined hole gas, combined with changes in valence-band dispersion in this region, leads to coupling of phonon interactions with a continuum of intervalence-band transitions to produce a shift in the Ge-Ge interface Raman peak. Although the Fano resonance lineshape can in principle differ dramatically from the Lorentzian form, we continue to model the Raman spectra for the core-shell nanowires using a superposition of Lorentzian lineshapes as we observe only very limited departures from Lorentzian behavior experimentally, as is evident from Figure 2. The limited asymmetry observed in our measurements is consistent with Raman spectra reported for

heavily doped bulk p-type Ge with room temperature hole concentrations similar to those estimated for the quantum-confined hole gas region in our samples.[7,42]

Coupling of phonons to intervalence-band carrier transitions has been identified previously as the dominant mechanism leading to a substantial negative shift in Raman peak wave number in heavily doped p-type Ge and Si.[7,68] Intravalence-band transitions, which may also occur but are not the primary contributor to the observed Raman peak shift, lead to a positive shift in Raman peak wave number in heavily doped p-type Ge, as well as a dependence of peak position on the excitation radiation wavelength.[7] Specifically in the case of heavily doped p-type Si, a detailed analysis has shown that coupling of the Si-Si vibrational mode to a continuum of electronic excitations produced by intervalence-band transitions with energies overlapping that of the vibrational mode leads to a shift of the Si-Si Raman peak to smaller wave numbers.[68] The valence band structure of Si is similar in a number of key respects to that of Ge, including splitting that occurs at the top of the valence band under strain, and similar effective masses for both the heavy-hole ($0.49m_e$ and $0.33m_e$ for Si and Ge, respectively, where m_e is the free electron mass) and light-hole ($0.16m_e$ and $0.043m_e$ for Si and Ge, respectively) valence bands.[42] The spin-orbit splittings (0.044eV and 0.29eV for Si and Ge, respectively) differ significantly, but the split-off band is not expected to play a very significant role at the hole concentrations expected to be present in Ge-$Si_{0.5}Ge_{0.5}$ core-shell nanowires.

Because of these similarities between the valence-band structures for Si and Ge, we have adopted the approach of Cerdeira *et al*[68] to analyze coupling between Ge-Ge phonon modes and intervalence-band transitions near the Ge/$Si_{0.5}Ge_{0.5}$ interface of the core-shell nanowires employed here. Specifically, the shift in the position of the Ge-Ge Raman peak arising from coupling to intervalence-band transitions is assumed to be given by[68]

$$\hbar\Gamma(\omega) = \pi \int \rho(\hbar\omega) \left\langle \left| \langle \psi_i | H | \phi \rangle \right|^2 \right\rangle_{av} dV \,, \tag{2.4}$$

where Γ is the magnitude of the shift in Raman peak position, $\rho(\hbar\omega)$ is the joint density of states for the continuum of intervalence-band transitions, $\left\langle \left| \langle \psi_i | H | \phi \rangle \right|^2 \right\rangle_{av}$ is the square of the magnitude of the electron-phonon interaction matrix element, averaged over different symmetry directions, and the integral is computed over the nanowire crystal volume. As the Fermi level moves deeper into the valence band with increasing hole concentration, the wave vectors of the optical phonons in a conventional Raman measurement, as given by Eq. (2.3), begin to allow electronic excitations within the valence band of p-type Ge at the optical phonon energy.[7] These transitions lower the electronic contribution to the free energy of the material, decreasing the elastic constants and thereby reducing the phonon energy. This behavior is directly observable as a shift of the Raman peak for the Ge-Ge vibrational mode to smaller wave numbers.[7,42]

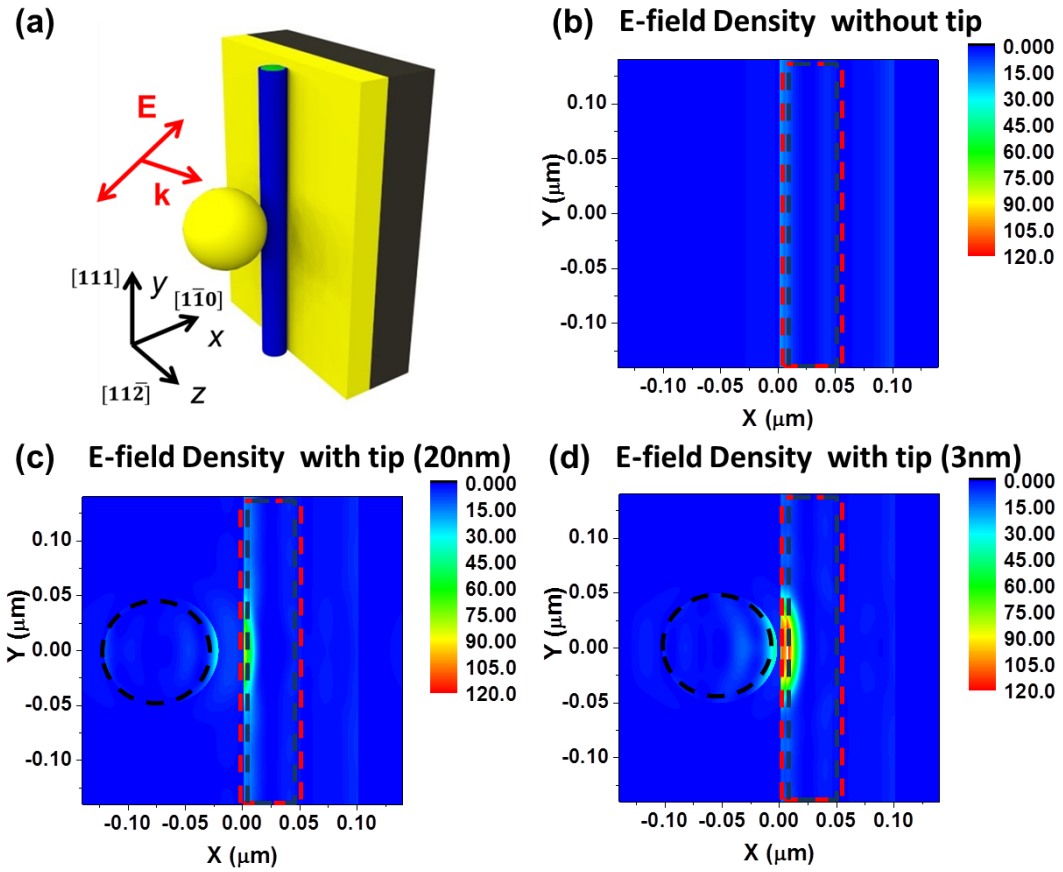

Figure 2.9. Computational electromagnetic simulations for an electromagnetic plane wave incident on a nanowire in proximity to an AFM probe tip, modeled as an Au sphere. **(a)** Schematic of simulation geometry showing **k** propagating at an angle of 30° relative to the z-axis and the electric field polarized at an angle of 30° relative to the x-axis. Spatial cuts of E_x are taken along the center of the nanowire in the x-y plane. Shown are field distributions for **(b)** the case without the tip, **(b)** the case with the tip at a distance of 20 nm from the nanowire, and **(c)** the case with the tip at a distance of 3nm from the nanowire. The dashed lines show the position of the tip (modeled as a sphere) and the nanowire.

In a TERS measurement, the proximity of the sample to the metallized AFM probe tip changes the spatial distribution of the electromagnetic field in the sample region near

the tip, and consequently increases the coupling between the Ge-Ge vibrational mode and the continuum of intervalence-band transitions. Figure 2.9 shows computational electromagnetic simulations of electric field distributions for a Ge-$Si_{0.5}Ge_{0.5}$ core-shell nanowire with a shell thickness of 5nm and total diameter of 50nm positioned just below a metallized probe tip, modeled for simplicity as an Au sphere 100nm in diameter, and subjected to plane-wave illumination at a wavelength of 633nm. The simulation geometry is illustrated in Figure 2.9a.

The RSoft DiffractMod software package was used to perform EM simulations. The DiffractMod package uses a combination of Rigorous Coupled Wave Analysis (RCWA) with Modal Transmission Line (MTL) Theory. RCWA represents the electromagnetic fields as a sum over coupled waves, while the periodic permittivity function is represented using Fourier harmonics. Each coupled wave is related to a Fourier harmonic, allowing the full vectorial Maxwell's equations to be solved in the Fourier domain and the spatial field distributions are computed from the Fourier harmonics. The diffraction efficiencies are then computed at the end of simulation. MTL is equivalent to RCWA, except that MTL uses summations over individual modes to represent the electromagnetic fields, which gives the benefit of describing the fields as an equivalent transmission-line network. The transmission-line network acts as a template for generating computational programs, and therefore providing a more systematic procedure to deal with complex geometries. In the simulation, five Fourier harmonics were used when modeling the simulation geometry. The incident electric field polarization is taken to be normal to the nanowire axis.

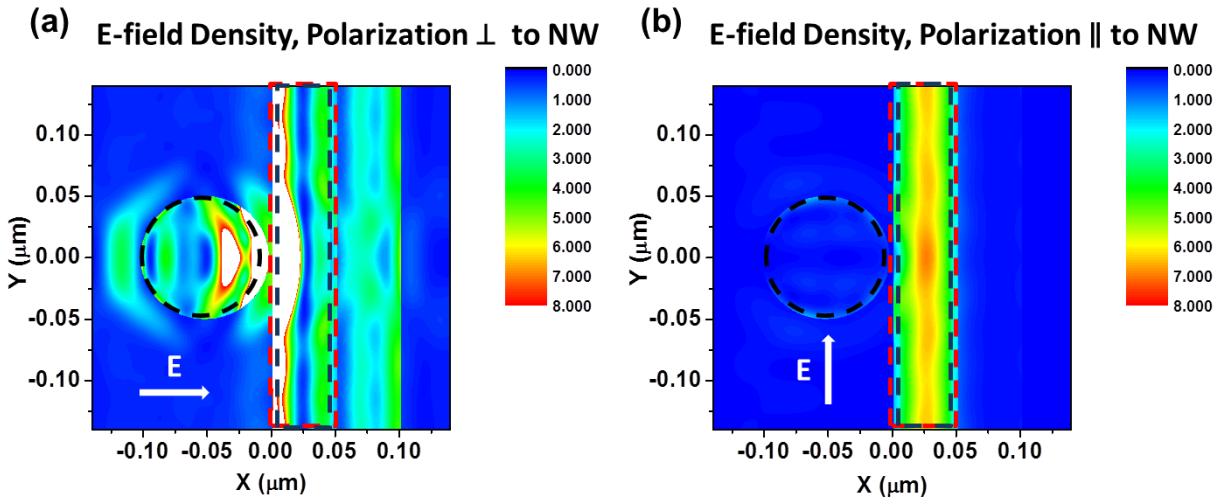

Figure 2.10. Computational electromagnetic simulations. Shown are results along the center of the nanowire in the x-y plane of the electric field density for **(a)** an electric field polarization of 30° in relation to the x-axis and **(b)** an electric field polarization along the y-axis. Both simulations are performed with the tip within 3 nm of the nanowire.

Prior studies[60] and our own simulations have shown that the polarization of the electric field can substantially influence the amplitude of the field within the nanowire core, as shown in Figure 2.10. When the electric field is polarized along the direction of the nanowire axis, the electric field density within the wire is significantly higher than when it is perpendicular to the nanowire axis. In the x-polarization case, the polarization is the same as in Figure 2.9. The polarization employed for the simulations shown in Figure 2.9 was chosen to highlight the effects of field localization by the metallized probe tip. Optical parameters for the materials present in the simulation volume were taken from the literature.[69]

Figure 2.9b-2.9d shows plots of the numerically simulated electric field density $U_E(\mathbf{r})$, given by

$$U_E(\mathbf{r}) = \frac{1}{2}\mathrm{Re}[\varepsilon(\mathbf{r})]|\mathbf{E}(\mathbf{r})|^2, \tag{2.5}$$

where $\varepsilon(\mathbf{r})$ is the complex dielectric function at the appropriate wavelength and $\mathbf{E}(\mathbf{r})$ is the electric field amplitude, in the *xy* plane that bisects the nanowire in the absence of the probe tip, and for separations between the tip and nanowire of 20nm and 3nm. The dashed lines indicate the positions of the Au sphere and the core and shell nanowire regions. As shown in the figure, there is a substantial enhancement in the electric field density in the nanowire region near the Au sphere used to model the metallized AFM probe tip, with the enhancement being much more pronounced, and extending farther into the nanowire, at a tip-sample distance of 3nm compared to that at 20nm. In addition, the field distribution in the absence of the Au sphere is, as shown in Figure 2.9b, largely plane wave-like, whereas with the Au sphere present, as in Figures 2.9c and 2.9d, the field distributions deviate substantially from those for simple plane waves.

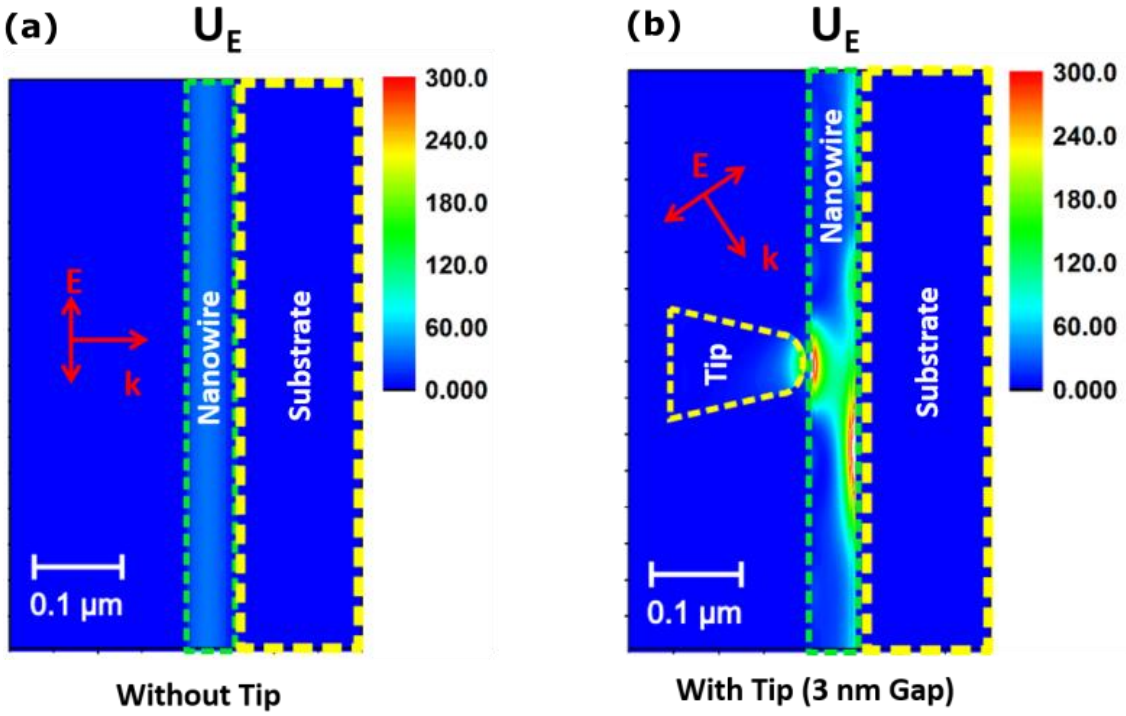

Figure 2.11. Computational electromagnetic simulations of electric field density with improved tip design. **(a)** Simulation without the tip with the k vector normal to the substrate surface. **(b)** Simulation with the improved tip 3 nm from the nanowire, with the same EM field conditions as Figure 2.5d.

We have also performed EM simulations of the interaction between the nanowire and an improved tip design that mirrors more closely the actual shape of a TERS tip. In these simulations, instead of just a sphere, we use a cone shaped tip shape as shown by in Figure 2.11b. The electric field density at the interface between the core and the shell remains very similar in profile to previous simulations with the tip modeled as a sphere.

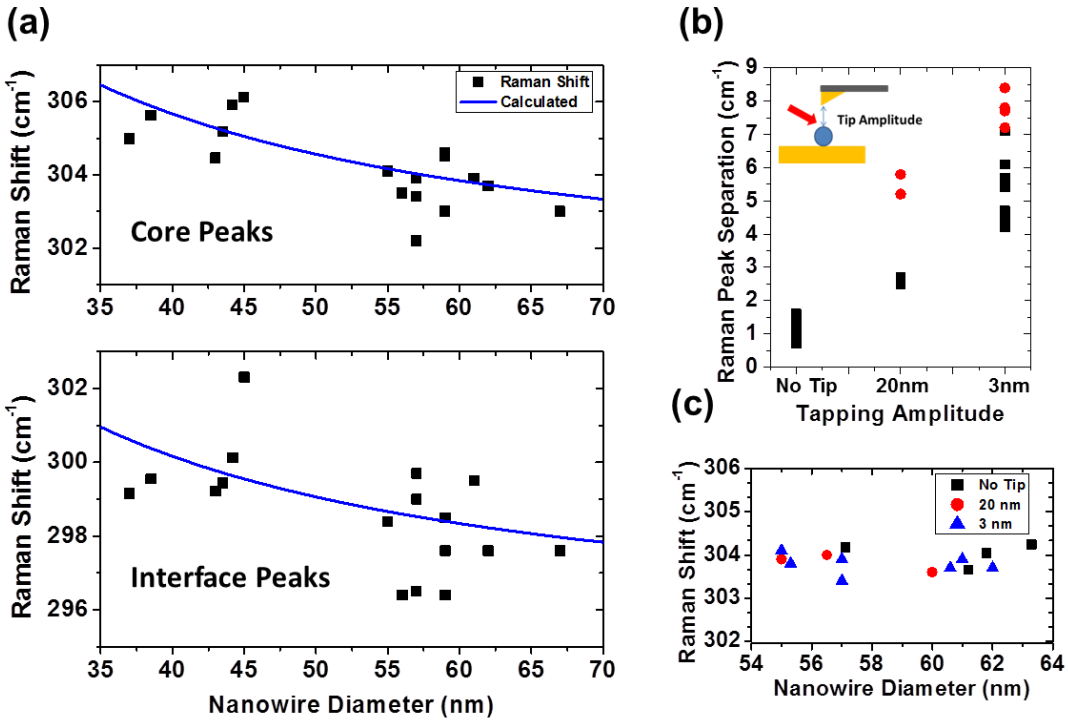

Figure 2.12. **(a)** Raman peak positions vs. total nanowire diameter. The top panel shows the core peak positions. The calculated Raman shift is shown with the solid blue line. The bottom panel shows the interface peak positions. The solid blue line represents the calculated Raman shift for the core peak (shown in the top panel) rigidly shifted by -5.5 cm^{-1}. **(b)** The separation between the core and interface peaks for our three measurement conditions. Different symbols represent measurements from different probe tips. **(c)** Core peak positions for various measurement configurations for a diameter range of 55 to 64 nm. Core peak positions are independent of measurement configuration.

The increased field density in the immediate vicinity of the probe tip results in an increased amplitude for the interface peak in the Raman spectra measured by TERS, as was shown in Figure 2.3. As a result, the positions of both the core and interface peaks can be precisely determined. Figure 2.12a shows the core and interface Raman peak positions from TERS spectra obtained for several different nanowire regions as functions of total

nanowire diameter at the probe tip position. Measurements were performed on regions of Ge-$Si_{0.5}Ge_{0.5}$ core-shell nanowires with diameters ranging from 35nm to 70nm and constant shell thicknesses of 5nm. All measurements shown in Figure 2.12a were performed in intermittent contact mode with a tip oscillation amplitude of 3nm. The solid lines in Figure 2.12a correspond to Ge-Ge Raman peak positions calculated based on measured nanowire dimensions and assuming coherent strain between the nanowire core and shell. Specifically, the calculated position of the core peak, corresponding to the solid line in the upper plot of Figure 2.12a, was obtained as a function of nanowire diameter by solving the secular equation of lattice dynamical theory with appropriate elastic constants.

The calculated Raman shift due to strain was determined by solving the secular equation obtained from lattice dynamical theory:[70]

$$\begin{pmatrix} p\varepsilon'_{11} + q(\varepsilon'_{22} + \varepsilon'_{33}) - \lambda_1 & 2r\varepsilon'_{12} & 2r\varepsilon'_{13} \\ 2r\varepsilon'_{12} & p\varepsilon'_{22} + q(\varepsilon'_{11} + \varepsilon'_{33}) - \lambda_2 & 2r\varepsilon'_{23} \\ 2r\varepsilon'_{13} & 2r\varepsilon'_{23} & p\varepsilon'_{33} + q(\varepsilon'_{11} + \varepsilon'_{22}) - \lambda_3 \end{pmatrix} = 0 \qquad (2.6)$$

The terms *p, q,* and *r* are the Ge core phonon deformation potential values, ε_{ij} indicates the values of the strain tensor, and λ_k are the wavelengths of the Raman modes. Eq. (2.6) can be simplified by taking into account the form of the strain tensor in the core due to the cylindrical symmetry of the NW. By taking the z-axis to be in the direction of the NW main axis, the [111] direction and the x and y axes as the $[1\bar{1}0]$ and $[11\bar{2}]$ directions, respectively, the strain tensor is then of the form:[39,40]

$$\boldsymbol{\varepsilon} = \begin{pmatrix} \varepsilon_{rr} & 0 & 0 \\ 0 & \varepsilon_{rr} & 0 \\ 0 & 0 & \varepsilon_{zz} \end{pmatrix}, \qquad (2.7)$$

where the in-plane components ε_{xx} and ε_{yy} are equal and labeled as ε_{rr}. The off-diagonal shear components are 0. The strain tensor is then converted into a crystal-oriented coordinate system where the x', y', and z' axes correspond to the [100], [010], and [001] directions, respectively. Using the following tensor transformation:

$$\varepsilon'_{ij} = \sum_{pq} a_{ip} a_{jq} \varepsilon_{pq}, \tag{2.8}$$

where

$$\mathbf{a} = \begin{pmatrix} 1/\sqrt{2} & 1/\sqrt{6} & 1/\sqrt{3} \\ -1/\sqrt{2} & 1/\sqrt{6} & 1/\sqrt{3} \\ 0 & -2/\sqrt{6} & 1/\sqrt{3} \end{pmatrix}, \tag{2.9}$$

this results in the following strain tensor:

$$\boldsymbol{\varepsilon}' = \begin{pmatrix} \frac{2}{3}\varepsilon_{rr} + \frac{1}{3}\varepsilon_{zz} & \frac{-1}{3}\varepsilon_{rr} + \frac{1}{3}\varepsilon_{zz} & \frac{-1}{3}\varepsilon_{rr} + \frac{1}{3}\varepsilon_{zz} \\ \frac{-1}{3}\varepsilon_{rr} + \frac{1}{3}\varepsilon_{zz} & \frac{2}{3}\varepsilon_{rr} + \frac{1}{3}\varepsilon_{zz} & \frac{-1}{3}\varepsilon_{rr} + \frac{1}{3}\varepsilon_{zz} \\ \frac{-1}{3}\varepsilon_{rr} + \frac{1}{3}\varepsilon_{zz} & \frac{-1}{3}\varepsilon_{rr} + \frac{1}{3}\varepsilon_{zz} & \frac{2}{3}\varepsilon_{rr} + \frac{1}{3}\varepsilon_{zz} \end{pmatrix}, \tag{2.10}$$

By substituting Eq. (2.10) into Eq. (2.6), a nondegenerate singlet mode $\lambda_s = \lambda_1$ and a degenerate doublet mode $\lambda_d = \lambda_2 = \lambda_3$ are obtained:

$$\begin{aligned} \lambda_1 &= \varepsilon_{zz}\left[\tfrac{1}{3}p + \tfrac{2}{3}q + \tfrac{4}{3}r\right] + \varepsilon_{rr}\left[\tfrac{2}{3}p + \tfrac{4}{3}q - \tfrac{4}{3}r\right], \\ \lambda_{2,3} &= \varepsilon_{zz}\left[\tfrac{1}{3}p + \tfrac{2}{3}q - \tfrac{2}{3}r\right] + \varepsilon_{rr}\left[\tfrac{2}{3}p + \tfrac{4}{3}q + \tfrac{2}{3}r\right], \end{aligned} \tag{2.11}$$

Using the polarization selection rule:[71]

$$I_i \propto \left|\vec{E}_{inc}^{T} \cdot \boldsymbol{R'}_i \cdot \vec{E}_{scat}\right|^2, \tag{2.12}$$

where

$$\boldsymbol{R'}_i = \sum_j \left(\vec{u}_j \cdot \vec{u}_i'\right) \boldsymbol{R}_j, \tag{2.13}$$

the relative intensities I_i, can be determined for the three Ge-Ge modes λ_i from Eq. (2.11). The unstrained phonon wavevectors, $\vec{u}_j$, are given by $\vec{u}_1 = [100]$, $\vec{u}_2 = [010]$, and $\vec{u}_3 = [001]$. $\vec{u}_i'$ are the phonon wavevectors under strain, where the values were found through a solution of Eq. (2.6) using a strain tensor of the form of Eq. (2.7) with arbitrary values for ε_{rr} and ε_{zz}. $\vec{E}_{inc}^{T}$ and $\vec{E}_{scat}$ are the polarization vectors of the incident and scattered light, respectively. $\boldsymbol{R'}_i$ are the Raman tensors of the perturbed system, while $\boldsymbol{R}_j$ are those of the unstrained cubic system.[72] After calculating the Raman intensities of the three Ge-Ge modes, it was determined that the singlet mode had the highest relative intensity and was the one being observed. The constants given in Table 2.1 were then used to determine the theoretical Raman shift:

Table 2.1. Elastic constants

p/w_0^2	q/w_0^2	r/w_0^2	a_{core} (Å)	a_{shell} (Å)	$E_{[111]}$ (GPa)	v	t (N/m)
-1.66[73]	-2.19[73]	-1.11[74]	5.658[75]	5.538[75]	155[75]	0.16[75]	1.00[39]

The calculated position of the interface peak, corresponding to the solid line in the lower plot of Figure 2.12a, was obtained by applying a rigid shift of -5.5cm^{-1} to the calculated core peak positions. For simplicity, this rigid negative shift was determined by

taking the average difference between the core and interface peak positions for each individual measurement.

As seen in Figure 2.12a, the calculated core and interface peak positions, and their dependence on total nanowire diameter, are in good agreement with those measured experimentally. The good agreement between the calculated and measured core peak positions provides confirmation that, for all the nanowire regions studied, the core and shell are coherently strained, with decreasing total nanowire and core diameter leading to an overall shift of the core peak from the intrinsic unstrained Ge-Ge vibrational mode position of 300.5cm^{-1} to larger wave numbers. This occurs because for a constant shell thickness, it is energetically favorable for compressive strain in the core region to increase in magnitude with decreasing core diameter and consequently volume, leading to the observed increase in Raman peak wave number with decreasing nanowire diameter. The very similar diameter dependence of the core and interface Raman peak positions indicates that both the core and interface peak positions are influenced by the same strain configuration. Since the only region of the core-shell nanowire that is expected to have spatially uniform strain is the Ge core, and since the shell region is expected to have a very different strain configuration, with a different diameter dependence, compared to the core,[12] we conclude that both the core and interface peaks are associated with Ge-Ge vibrations in the Ge core, with the interface peaks corresponding to Ge-Ge vibrations near the Ge-$Si_{0.5}Ge_{0.5}$ core-shell interface.

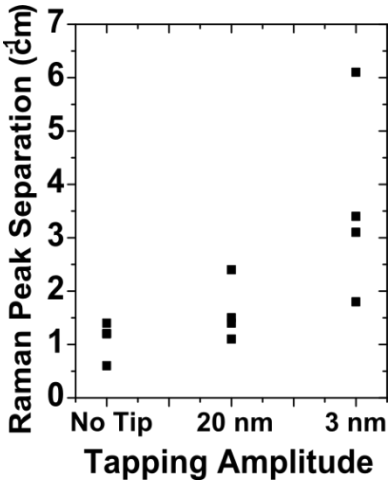

Figure 2.13. The separation between the core and interface peaks for our three measurement conditions with vertically polarized laser excitation.

Figure 2.12b shows the separation between the core and interface peaks measured for various nanowire regions using conventional Raman spectroscopy ("no tip"), and for tip oscillation amplitudes, which to a reasonable approximation correspond to the average distance between the tip apex and sample surface, of either 20nm or 3nm. The two different symbols represent measurements with two different tips. For both probe tips, the separation between the core and interface peaks increases in the presence of the probe tip and as the probe tip moves closer to the sample surface, although the size of the peak separation varies from one tip to the other. Experimental data obtained with a vertical polarizer along the excitation laser path shows the same relationship between peak separation and distance between probe tip and sample surface as shown in Figure 2.13. Differences in the precise values of Raman peak separation as a function of tip tapping amplitude occur due to variations in tip shape and size at the nanoscale.

Figure 2.12c shows the position of the Raman core peak measured in the absence of a probe tip and for tip oscillation amplitudes of 20nm and 3nm, for nanowire diameters ranging from 55nm to 64nm. The position of the core peak is seen to be independent of

proximity to, and even the presence of, the probe tip, demonstrating that the increased peak separation with increasing tip proximity shown in Figure 2.12b is due entirely to a shift in the position of the interface peak. In addition, the observation that the core peak position remains fixed for the different measurement configurations employed confirms that the enhanced fields from the tip are not significantly changing the background hole density in the Ge core or inducing local heating effects, which would be expected to be more prominent in the TERS measurement than in conventional Raman spectroscopy, and which would produce a negative shift in Ge-Ge core peak position, or introducing other factors that would affect the core peak position.

The shift in Ge-Ge interface peak position with increasing proximity to the probe tip can be explained as follows. Without the Au-coated probe tip present, the phonon wave vector magnitude q, given by Eq. (2.3), is determined by the wavelength of the incident illumination and the nanowire refractive index. For typical wavelengths, q is very small in comparison to the size of the Ge crystal Brillouin zone, and therefore severely constrains the intervalence-band transitions that are consistent with conservation of linear momentum. In conventional Raman spectroscopy of a Ge-$Si_{0.5}Ge_{0.5}$ core-shell nanowire, the high hole concentration present in the quantum-confined hole gas at the Ge/$Si_{0.5}Ge_{0.5}$ interface, combined with altered valence-band dispersion associated with quantum confinement, enables these transitions to occur and produces the observed shift in the position of the interface peak position. In the presence of the probe tip, however, the fields are no longer plane wave-like in the immediate vicinity of the tip. The fields scattered by the tip contain additional Fourier components, which provide additional options to satisfy momentum conservation constraints in phonon scattering, and therefore enable greater interaction between the Ge-Ge vibrational modes excited by the incident illumination and electronic transitions within the Ge valence bands. This basic concept was illustrated in Figure 2.4b,

which shows the energy and momentum shifts associated with multiple intra and intervalence-band transitions with the same energy, but different wave vectors; more such transitions will be allowed for TERS compared to conventional Raman measurements.

Fourier Analysis of Electromagnetic Simulations

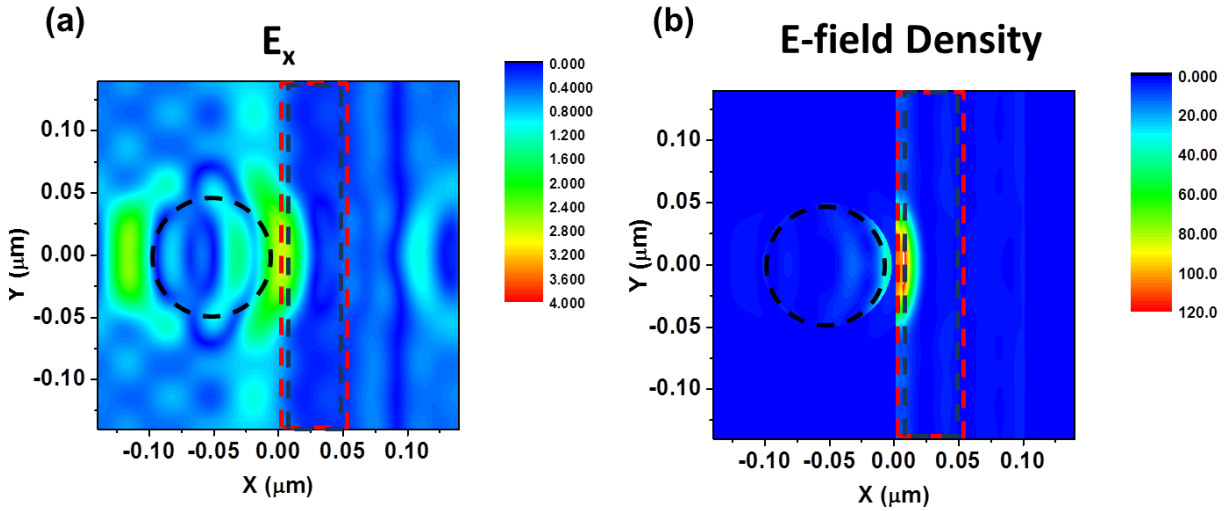

Figure 2.14. Computational electromagnetic simulations. Spatial cuts along the center of the nanowire in the x-y plane of **(a)** E_x and **(b)** the electric field density are shown. Both simulations are performed with the tip within 3 nm of the nanowire.

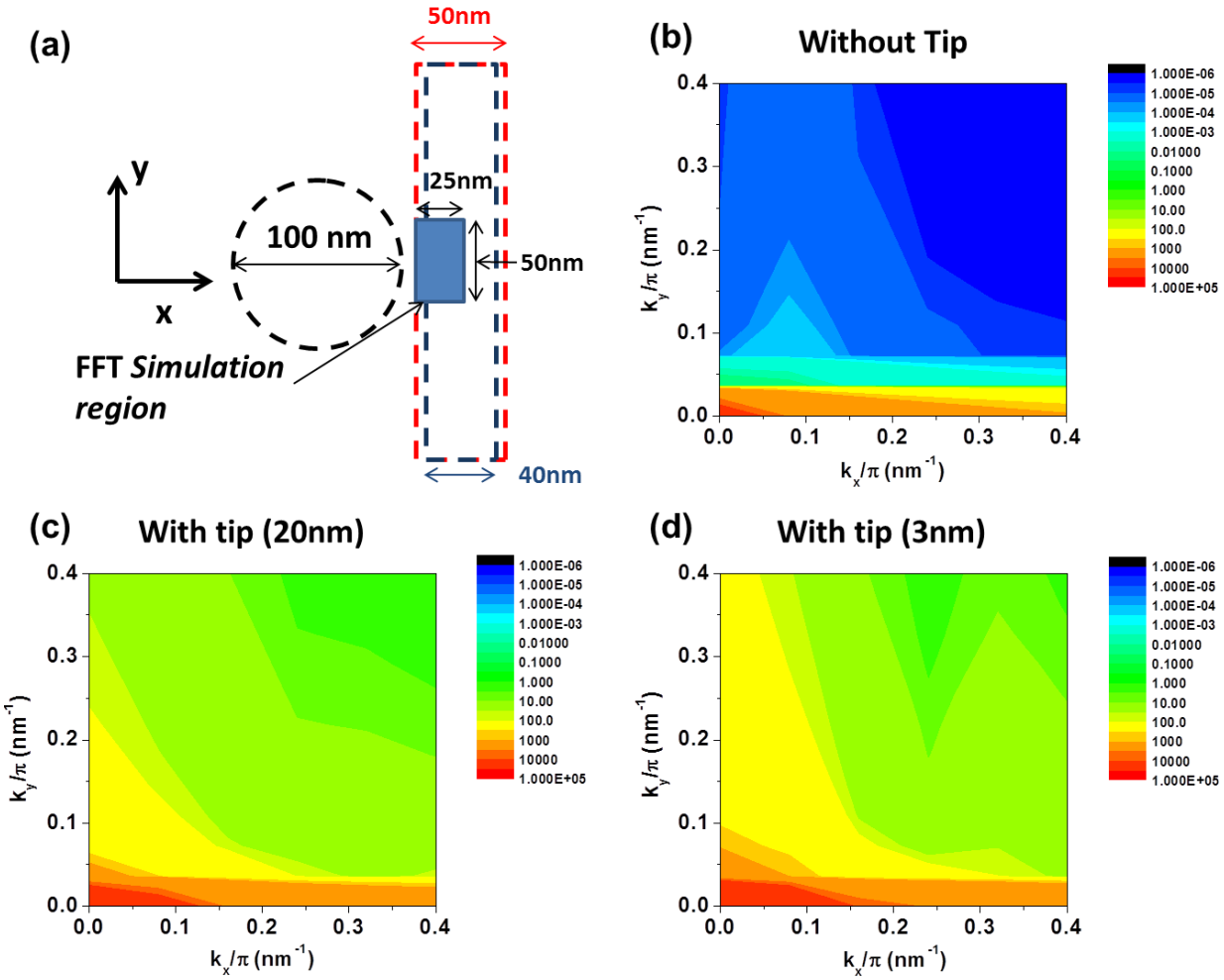

Figure 2.15. 2D FFT computations from our spatial electric field simulation data **(a)** Schematic of the simulation region used to compute the 2D FFT. The calculated electric field component in the x-direction (E_x) for the 25nm × 50nm region of the nanowire closest to the Au tip is used to compute the 2D FFT. Computation results for the cases **(b)** with no tip, **(c)** with a tip 20 nm from the nanowire, and **(d)** with a tip 3 nm from the nanowire.

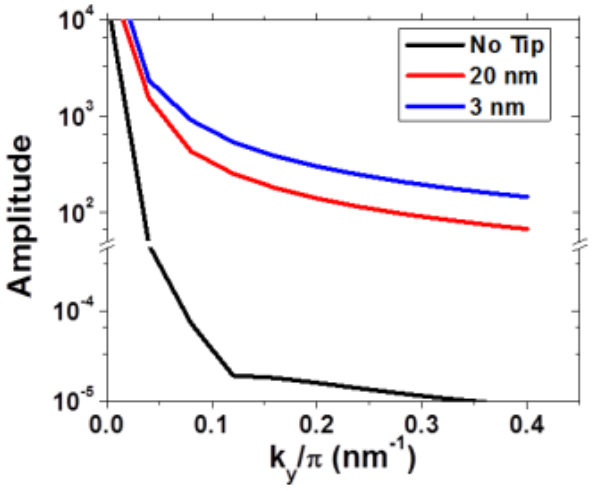

Figure 2.16. Fourier amplitude as a function of k_y computed from EM simulations for $k_x = 0$

Fourier analysis of numerically simulated electromagnetic field distributions provides further insight into the influence of probe tip proximity on Raman scattering processes and coupling between optically excited phonons and intervalence-band transitions in the TERS experiments reported here. Specifically, two-dimensional Fast Fourier Transforms (FFTs) have been performed on the *x*-component of the electric field, E_x, computed for an electromagnetic plane wave of wavelength 633 nm incident on a Ge-SiGe core-shell nanowire under the same conditions and for the same geometries as in Figure 2.9. E_x was selected for this analysis because it is the dominant field component in the electric field density in the vicinity of the probe tip as shown in Figure 2.14. The features in the spatial field distribution at the interface region are very similar for both the electric field component in the x-direction and the electric field density plots. As shown in Figure 2.15a, the FFT analysis was performed for a 25nm×50nm region of the nanowire closest to the Au sphere in the simulation, and in the *xy*-plane bisecting the nanowire. Full FFT computations for the no tip, 20 nm tip separation and 3 nm tip separation scenarios

are shown in Figures 2.15b, 2.15c, and 2.15d, respectively. Figure 2.16 shows the Fourier amplitude as a function of k_y computed from the electromagnetic simulations for $k_x = 0$ in the absence of the Au sphere, corresponding to a conventional Raman spectroscopy measurement configuration, and with the sphere surface either 20 nm or 3 nm from the nanowire surface, corresponding to TERS measurements with tip oscillation amplitudes of 20 nm or 3 nm, respectively. Since the allowed wave vectors for carriers in the quantum-confined hole gas in the *xy*-plane are quantized in the *x*-direction, the Fourier amplitudes are analyzed only as a function of k_y. The greater Fourier wave amplitudes are limited to k_y values close to the Brillouin zone center, which allows us to assume that the additional Fourier components only create discrete states at the flat zone center region of the Ge optical phonon dispersion and therefore limits the energy range of the optical phonons that interact with the continuum of intervalence-band transitions.

Raman Shift Analysis

We model the effect of these additional Fourier components by including multiple discrete phonon states with wavevectors limited to values near the center of the Brillouin zone, consistent with Fourier analysis of simulated field distributions, shown in Figure 2.15, that interact with the continuum of intervalence-band carrier transitions. The energy range of the optical phonons remains very narrow because the optical phonon dispersion in Ge is nearly flat at the Brillouin zone center.[76] The limited range of energies and wavevector values for the optical phonons results in consistent magnitude of second-order coupling between each discrete phonon state and other excited phonon states, due to coupling via the continuum of carrier transitions, and between each discrete phonon state and the continuum, which combined cause an absolute shift in the phonon self-energy that is consistent across all the discrete states.[67] The consistent absolute shift in the phonon self-

energy results in a greater separation between the core and interface peaks with limited peak broadening for the interface peak as can be seen in Figure 2.7b.

For heavily p-type Si and Ge, the dominant mechanism that causes the significant red shift in the Raman spectra when compared to the intrinsic material is intervalence band carrier transitions rather than intravalence band carrier transitions, although both types of transitions may occur.[7] The Raman shift caused by the intervalence band transitions can be described by[68]

$$\hbar\Gamma(\omega) = \pi \int \rho(\hbar\omega)\langle|\langle\psi_i|H|\phi\rangle|^2\rangle_{av}\, dV, \tag{2.14}$$

where Γ is the magnitude of the Raman shift, $\rho(\hbar\omega)$ is the combined density of states for the continuum of intervalence band transitions, $\langle|\langle\psi_i|H|\phi\rangle|^2\rangle_{av}$ is the average matrix element of the electron-phonon interaction for different symmetry directions, and the integral is computed over the nanowire crystal volume. By assuming the average matrix element is independent of energy and by computing the two-band electron-phonon matrix element using the deformation potential approximation for 26 directions in k space (6{100}, 8{111}, and 12 {110}), this leads to a value given by[68]

$$\langle|\langle\psi_i|H|\phi\rangle|^2\rangle_{av} = \frac{95}{78}\left(\frac{1}{2}\delta E\right)^2, \tag{2.15}$$

where $\delta E$is the splitting of the top of the valence band produced by the k = 0 optical phonon. Assuming δE is constant for the excitation volume of the crystal, the splitting for the ground state zero-point phonon is given by[68]

$$\delta E = \left(\frac{a^3\hbar}{4MV_{ex}\Omega}\right)^{1/2}\frac{2d_0}{a}(1+n_B)^{1/2}, \tag{2.16}$$

where a is the lattice constant, M is the ionic mass, V_{ex} is the excitation crystal volume, d_0 is the deformation potential and n_B is the number of phonons which are distributed in energy according to the Bose-Einstein distribution, which relates directly to the number of phonons involved in the splitting of the top of the valence band. By assuming $\rho(\hbar\omega)$ is also constant for the excitation volume, the expression for Γ is then[68]

$$\hbar\Gamma = \frac{\pi}{4}\left(\frac{95}{78}\right)\frac{\hbar a}{M\Omega} d_0^2 \rho(\hbar\omega)(1 + n_B). \tag{2.17}$$

To evaluate Γ, a numerical estimate of ρ must be obtained, which can be determined by its value at the Fermi energy (μ), by assuming limited variation in $\rho(\hbar\omega)$ in the neighborhood of $\omega = \Omega$. Parabolic bands can be assumed with masses m_h and m_l for the heavy hole and light hole valence bands. Using these assumptions, the density of states is given by[68]

$$\rho(\mu) \cong \frac{3}{2}\frac{\alpha^{3/2}}{(1-\alpha)^{3/2}(1-\alpha^{3/2})}\frac{N_h - N_l}{\mu}, \tag{2.18}$$

where $= m_l/m_h = 0.22$, for heavy hole and light hole effective masses for Ge calculated using the k.p method.

In the case of the interface region of the nanowire in close proximity to the probe tip, additional wavevector values are produced by the changed spatial field distribution. Additional wavevector values relax momentum conservation constraints and result in a greater number of phonons involved in the intervalence band transitions. This now means that instead of just taking into account the effect of the k = 0 optical phonon, a distribution of phonons, with the maximum centered at k = 0, contribute to the intervalence band carrier transitions. An increase in intervalence band carrier transitions would result in a pronounced increase in the red shift of the Raman spectrum. To quantify this increased

change, the value of n_B must be first determined. The value of Γ can be compared to the Raman shifts measured in the case without the tip to determine the appropriate value of n_B that will be used in further calculations. For a Raman shift of ~1.2 cm^{-1}, which is the average for our Raman measurements without the tip, we obtain a value for n_B of 0.62. To incorporate the effect of the tip, an additional distribution function representing the distribution of additional phonons allowed by momentum conservation relaxation is convoluted with Eq. (2.17) to represent the distribution of phonons that are now allowed instead of just the zone center optical phonon.[77] This yields an equation for the Raman shift given by

$$\hbar\Gamma = \frac{\pi}{4}\left(\frac{95}{78}\right)\frac{\hbar a}{M\Omega} d_0^2(1+n_B)\int \rho(\hbar\omega')h(\hbar\omega')d\omega', \tag{2.19}$$

where $h(\hbar\omega)$ is the distribution function for the allowed phonons. Because $\rho(\hbar\omega)$is very flat around $\omega = \Omega$, its value can be taken as a constant with a value determined by Eq. (2.18). Solving the integral for Eq. (14) is now simple and yields:

$$\hbar\Gamma = \frac{\pi}{4}\left(\frac{95}{78}\right)\frac{\hbar a}{M\Omega} d_0^2(1+n_B)\,\rho(\mu)h_d, \tag{2.20}$$

where h_d is the value of the integral of the phonon distribution function. For a Γ of 4.2 and 8.4 cm^{-1}, the lower and upper bounds for the interface peak Raman shift for 3 nm tapping amplitude measurements, the values for h_d are 3.5 and 7.0, respectively. The average Γ for conventional Raman measurements is 1.0, which corresponds to a h_d of 0.83. If the conventional Raman results are used to normalize the distribution function, the resulting full width half maximum (FWHM) of h_d for the lower bound and upper bound for 3 nm tapping amplitude measurements would be 2.4 cm^{-1} and 4.7 cm^{-1}. In previous results relating optical phonons and acceptor continuum states in Si, the FWHM for the

phonon distribution was found to be ~15 cm^{-1} which is greater but still reasonably close to the values determined in the TERS measurement.[77]

Although the detailed analysis of the additional Raman shift arising from coupling of phonons to intervalence-band transitions was performed assuming bulk valence band structure parameters for Ge, we expect that the same concepts, with qualitatively similar conclusions, should apply for core-shell nanowires and intervalence-band transitions in the quantum-confined hole gas. In particular, we anticipate that coupling between the Ge-Ge vibrational mode and intervalence-band transitions in the quantum-confined hole gas will still occur due to the high local hole concentration, although the strength of that coupling will vary depending on the detailed structure of the valence subbands. The additional Fourier components of the electric field induced by proximity to the probe tip will increase this coupling, just as in the bulk case, resulting in an increased shift of the Raman interface peak to smaller wave numbers in the presence of the probe tip, and with decreasing distance between the probe tip and nanowire surfaces.

CONCLUSIONS

In conclusion, we have performed TERS and conventional Raman spectroscopy measurements on Ge-SiGe core-shell nanowires and, for the first time, identified two clearly distinguishable Ge-Ge vibrational mode Raman peaks from the core and interface regions of the nanowires. We confirm the origin of the two Ge-Ge mode Raman peaks, and determine the local strain configuration in the nanowire, through analysis of the diameter dependence of the Raman peak positions. We also demonstrate that positioning the Au coated AFM probe in close proximity to the nanowire directly causes a pronounced increase in the separation between the core and interface peaks and overall larger interface peak signal that indicates localized probing of that specific radial region of the nanowire.

By performing a Fourier analysis on electromagnetic simulations of field distributions arising from the presence of a probe tip and the interaction between tip and nanowire, we find an increase of the higher-order Fourier amplitudes in the vicinity of TERS probe. The increased amplitudes of higher-order Fourier components cause significantly more coupling of intervalence-band transitions to phonon modes, which directly leads to an increased negative shift in the position of the interface peak. This study also opens up possibilities for further investigations into local bonding, phonon behavior, carrier distributions, and phonon-carrier interactions in a variety of solid-state nanostructures.

Chapter 3: Probing Nanoscale Variations in Strain and Band Structure of MoS_2 on Au Nanopyramids[B]

INTRODUCTION

Atomically thin MoS_2 is an especially interesting material system to study using TERS because of the nanoscale variations in strain, layer thickness, and electronic band structure that can be present. Previous work has shown that the MoS_2 electronic band structure is highly sensitive to strain,[18] which emphasizes the need to characterize strain at the nanoscale when designing low dimensional devices. Conventional Raman measurements on MoS_2 have previously been used to measure changes in strain and band structure through Raman and PL measurements but often with low spatial or spectral precision.[10,18] RR scattering in MoS_2 probes a variety of second-order Raman features that can yield additional information about material properties such as electronic band structure.[53,54]

We have performed localized characterization of thickness, strain, and bandstructure of monolayer and bilayer MoS_2 using TERS, through both the first order and second order Raman modes, as well as tip enhanced photoluminescence (TEPL). By combining Raman spectroscopy with a scanning probe technique, we can dramatically increase positional precision while simultaneously achieving superior spatial resolution. Using AFM, we identify a region of MoS_2 that transitions from monolayer to bilayer and perform TERS measurements that accurately distinguish sample thickness with resolutions well below the diffraction limit. We also observe a previously unreported negative shift in the second order acoustic phonon Raman band at the interface between monolayer and

[B] [1] Z. Zhang, A.C. De Palma, C.J. Brennan, G. Cossio, R. Ghosh, S.K. Banerjee, and E.T. Yu, Phys. Rev. B **97**, 85305 (2018). Zhongjian Zhang designed the experiment, performed Raman spectroscopy, photoluminescence, atomic force microscopy measurements, analyzed the collected data, and wrote the manuscript.

bilayer regions. After applying strain to bilayer MoS_2 by draping the sample over patterned Au nanopyramids, we detect changes in strain across a half a micron region using both TERS and TEPL through the negative shift in the first order Raman modes and the change in intensity of the PL spectra that occurs in isolated regions of higher tensile strain. We also show in detail the strain dependence of the second order Raman modes in MoS_2 for the first time that further indicates changes in the band structure of MoS_2 induced by applied strain. Finally, we perform density functional theory (DFT) simulations that show the strain dependent changes in the second order Raman spectra directly correlate with strain dependent changes in the band structure and phonon dispersion.

MoS_2 Growth and Transfer

The MoS_2 samples studied in these experiments were grown by a standard vapor transfer growth process with MoO_3 (15 mg) and sulfur (1 g) powder as the starting materials. Further information on growth details can be found in Reference 78.

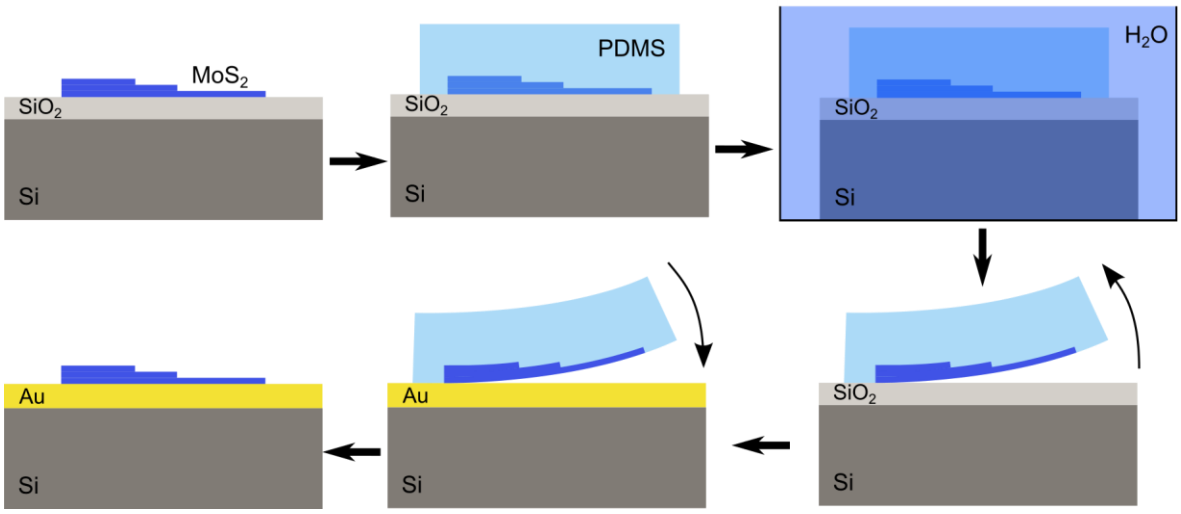

Figure 3.1. Schematic drawings of process flow for polydimethylsiloxane (PDMS) stamp transfer process

MoS_2 was transferred from the growth substrate on to both a flat Au substrate or the patterned Au nanopyramid substrate using a PDMS stamp and water transfer process. Figure 3.1 shows a schematic of the transfer process. MoS_2 was transferred from the growth substrate on to both a flat Au substrate or the patterned Au nanopyramid substrate using a PDMS stamp and water transfer process. The as-grown MoS_2 is under approximately 0.21% residual tensile strain[79], which is relaxed under the transfer process. The PDMS stamp is applied to a region of the growth substrate with atomically thin MoS_2. To separate the MoS_2 from the growth substrate, the substrate, MoS_2 and stamped PDMS is placed in a water bath. The PDMS stamp with the MoS_2 is then pressed on to either the flat or patterned Au substrates and heated with a hot plate to 50° C. Slowly peeling away the PDMS transfers the MoS_2 to the substrate.

EXPERIMENTAL DETAILS

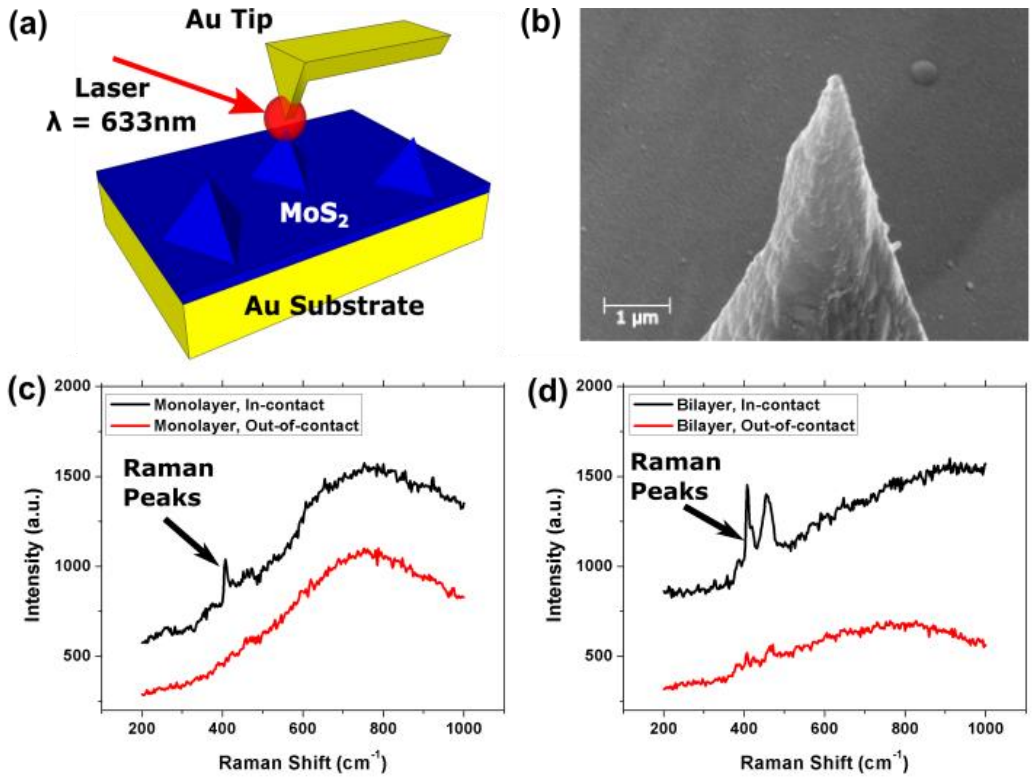

Figure 3.2. (a) Schematic diagram of the TERS experimental geometry for TERS measurements of MoS_2 draped over Au nanopyramid structures. **(b)** SEM image of an example Au tip used for TERS and TEPL measurements. Raman spectra obtained with the Au AFM probe in tapping mode (red curve) and in soft contact with the sample surface (black curve) from **(c)** monolayer MoS_2 and **(d)** bilayer MoS_2

Figure 3.2a shows a schematic diagram of the TERS experimental setup with tip and sample geometries for TERS measurements of MoS_2 on a patterned Au nanopyramid sample. MoS2 regions characterized by TERS are first located by AFM topographic scanning in tapping mode, which is also used to determine layer thickness and changes in topography. Au coated AFM probe tips used in experiments were purchased commercially and first tested to demonstrate signal enhancement on a reference sample. Figure 3.2b

shows a scanning electron microscopy (SEM) image of a typical tip where we estimate the radius of curvature from the image to be about 50 nm. TERS and TEPL measurements were taken with the tip in soft contact with the sample surface to maximize signal enhancement.

Figures 3.2c and 3.2d show Raman spectra taken from monolayer and bilayer regions of MoS_2, respectively. The red curves indicate spectra taken with the Au AFM probe in tapping mode with a 15 nm tapping amplitude. The black curves indicate spectra taken with the Au AFM probe in soft contact mode, which is the condition with which all TERS and TEPL data reported here were taken. Measurements taken in soft contact show a dramatic increase in Raman signal when compared to measurements taken in tapping mode. When the tip is placed into soft contact with the sample surface, the distance between the Au tip and the Au substrate decreases to around the order of a few nm, which allows a gap mode to form between the tip and substrate with strong enhancement of the EM field within that region that greatly increases the Raman signal as well as the background luminescence.[80] The significant signal enhancement indicates that by placing the probe tip in very close proximity to the sample, we can increase both signal localization and local excitation intensity.

MoS_2 Raman Analysis

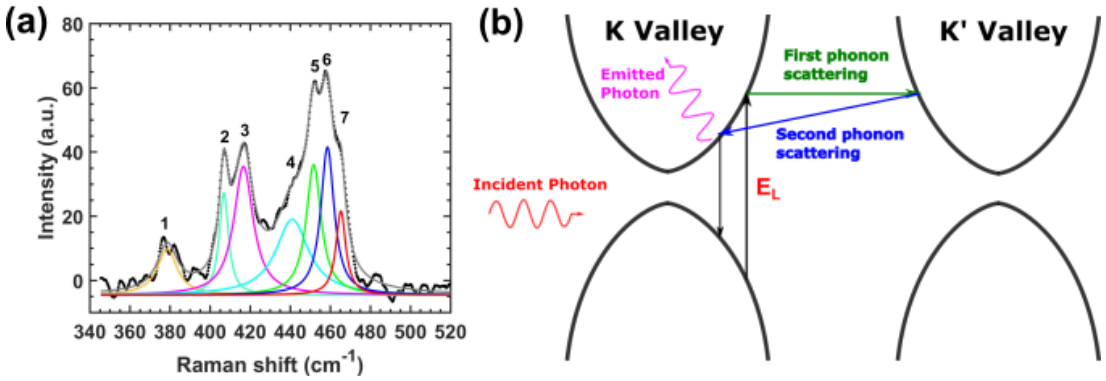

Figure 3.3. (a) TERS spectrum from bilayer MoS_2. The TERS spectrum has been fit to 7 Lorentzian peaks with the corresponding numbers matching vibrational modes listed in Table 1. The sum of the fitted peaks is shown in red and shows excellent agreement with the measured spectra. **(b)** Schematic drawing of an example DRR process where first an incident photon of energy E_L excites an electron-hole pair in the K valley, then the excited electron is scattered to the K' valley through the emission of the phonon, as shown with the green arrow. The excited electron is then scattered back to the K valley through the emission of a second phonon, as shown with the blue arrow. Finally, the electron hole pair recombines and emits a photon.

Table 3.1. Corresponding vibrational modes for fitted Lorentzian peaks shown in Figure 3.3a. Peak assignments, where indicated, obtained from Reference 54.

Peak #	Vibrational Modes
1	E_{2g}^1
2	A_{1g}
3	$LA(\sim \boldsymbol{K}) + TA(\sim \boldsymbol{K})$[54]
4	$A_{1g} + E_{2g}^2$ or possibly asymmetry from peak 5[54]
5	Van Hove Singularity in the phonon DOS[54]
6	$2LA(\sim \boldsymbol{K})$ [54]
7	$2LA(\sim \boldsymbol{M})$ [54]

Figure 3.3a shows a TERS spectrum for bilayer MoS_2 on a flat Au substrate that has been fit to 7 Lorentzian peaks to estimate the spectral positions of the various Raman modes. The peaks have been numbered and assigned a corresponding vibrational mode, listed in Table 3.1, that has been identified experimentally and theoretically in Reference 54. In our RR regime, the first order in-plane E_{2g}^1 mode centered at ~380 cm^{-1}, labeled peak 1, displays some asymmetry but we found it is still best to analyze the spectral position by fitting with one Lorentzian peak. Peak 2, centered at ~405 cm^{-1}, represents the out-of-plane A_{1g} vibrational mode. The remaining peaks represent second order Raman modes, which we emphasize we fit to single Lorentzians for convenience, since second order modes generally involve convolutions of multiple interactions.

Most of the second order Raman modes represent double resonance Raman (DRR) interactions that occur due to intervalley resonant scattering of the excited electrons by phonons. As illustrated schematically in Figure 3.3b, an example DRR process starts when an incoming photon excites an electron-hole pair near the K valley of the Brillouin zone (BZ). The excited electron is then inelastically scattered by the emission of a phonon to the K' valley. After the first scattering process, the excited electron is inelastically scattered back to the K valley by the emission of a second phonon, where then the electron-hole pair recombines and emits a photon. Which phonons can mediate this scattering interaction is governed by energy and momentum conservation constraints. In our work, the DRR process describes the scattering of excited electrons by longitudinal acoustic (LA) and transverse acoustic (TA) phonons associated with Raman modes represented by peaks 3, 6, and 7.[54]

From Reference 54 and as listed in Table 3.1, we associate peak 3, centered at ~420 cm^{-1}, with intervalley scattering of excited electrons near the K point in the BZ by a combination of LA and TA phonons. Peak 4, centered at ~445 cm^{-1}, represents either a combination of the A_{1g} and E_{2g}^2 vibrational modes or an asymmetry related to peak 5. Peak 5, centered at ~455 cm^{-1}, represents a van Hove singularity in the phonon density of states (DOS) which can be shown as a saddle point between the M and K points in the BZ. Finally, Peak 6, centered at ~465 cm^{-1}, and peak 7, centered at ~470 cm^{-1}, represent intervalley scattering of excited electrons by two LA phonons near the K point and M point of the BZ, respectively. Each Raman mode gives unique information about the sample. We observe all the first and second order Raman modes in all TERS measurements in both monolayer and bilayer MoS_2.

DENSITY FUNCTIONAL THEORY SIMULATIONS

Computational Details

We performed first-principles plane wave calculations within density functional theory (DFT) executed in the Plane-Wave Self-Consistent Field (PWscf) package of Quantum Espresso[81] using ultrasoft pseudopotentials.[82] The exchange correlation potential was approximated by a generalized gradient approximation (GGA) using the PW91 functional.[83] Dispersion corrections using the DFT-D2 method were used during structural optimizations to determine the interlayer spacing in bilayer MoS_2 structures.[84] A vacuum spacing exceeding 10 Å was employed in the unit cells in order to separate adjacent supercells. A kinetic energy cutoff of 70 Ry was used, and the Brillouin zone was sampled using a Monkhorst-Pack grid[85] of 25×25×1 and 15×15×3 k-points for monolayer and bilayer calculations, respectively. Atomic positions and lattice constants were optimized using damped molecular dynamics and the quick-min Verlet algorithm. The Hellmann-Feynman force acting on each atom was limited to under 3×10^{-7} Ry per atomic unit, and the pressure in the unit cell was limited to less than 0.1 kbar. Structural optimizations yielded a lattice parameter of a = 3.2201 Å, which is within 2% of the experimentally measured lattice parameter of 3.16 Å.[86] The calculated interlayer Mo-Mo spacing for bilayer MoS_2 is 6.2177 Å. Strain was applied to the lattice in the form of in-plane biaxial strain. In strained unit cells, atoms were relaxed along the axis perpendicular to the plane, but were otherwise fixed. Phonon vibrational frequencies were calculated using density functional perturbation theory (DFPT) as implemented in the PHonon package of Quantum Espresso.

Electronic Bandstructure Simulations

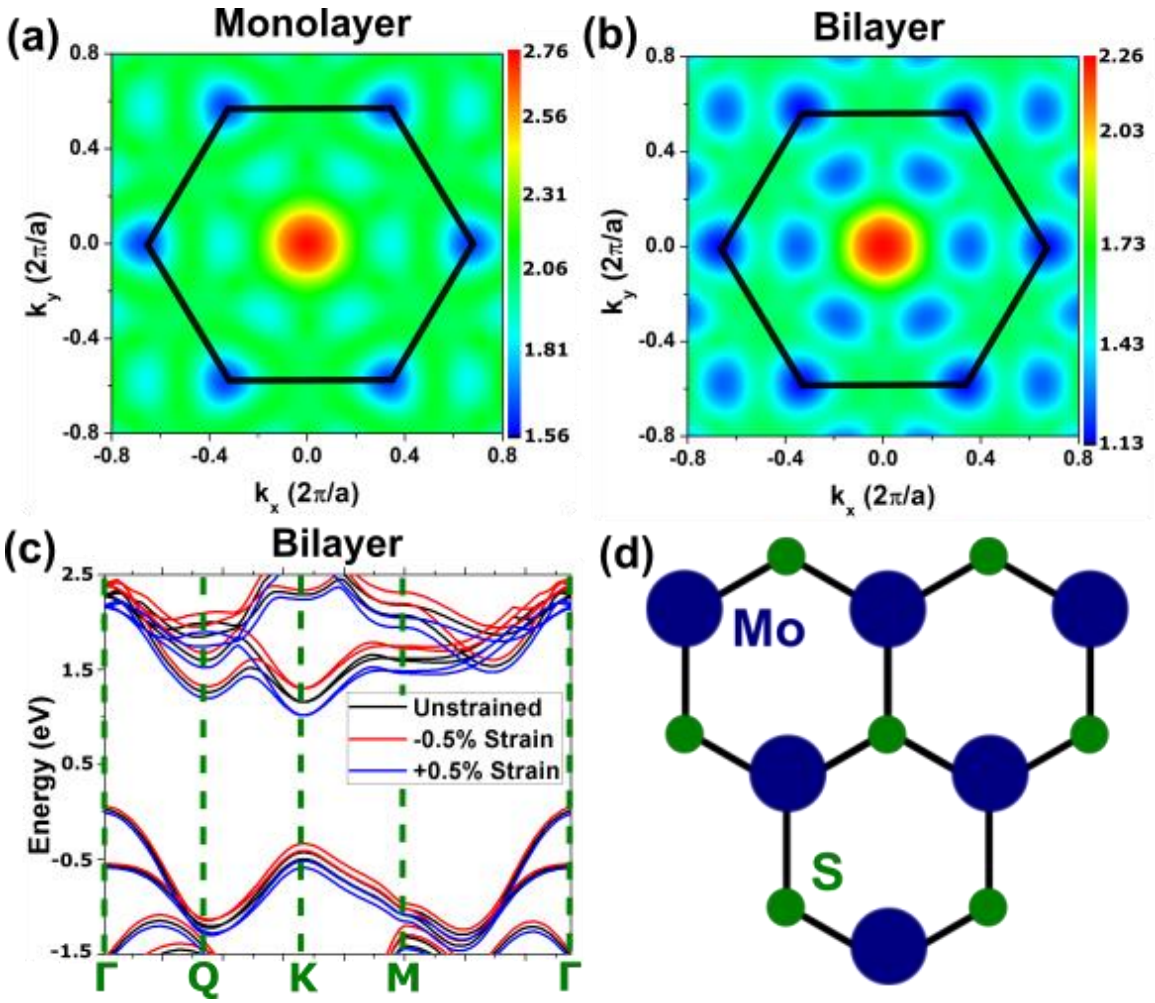

Figure 3.4 Contour maps of the conduction band edge energy calculated from density functional theory band structure simulations for **(a)** monolayer (a = 3.2139 Å) and **(b)** bilayer (a = 3.2201 Å) MoS_2. **(c)** Cut of the band structure along the high symmetry directions in k for unstrained (black curve), -0.5% applied hydrostatic strain (red curve), and +0.5% applied hydrostatic strain bilayer (blue curve) MoS_2. The high symmetry points (Γ, Q, K, M) are indicated by the green dashed lines. **(d)** Top view of the monolayer MoS_2 lattice structure.

Figures 3.4a and 3.4b shows contour plots of the conduction band minimums from the band structure in monolayer and bilayer MoS_2, respectively, calculated from DFT

simulations. The conduction band minimum at the Q point in the BZ decreases in energy relative to the conduction band minimum at the K point in the BZ from monolayer to bilayer. Figure 3.4c shows a cut of the band structure for the high symmetry directions and point (Γ, Q, K, M) in the BZ for unstrained, -0.5% applied hydrostatic strain, and +0.5% applied hydrostatic strain bilayer MoS_2. The strain behavior of the conduction band minima at the various high symmetry points varies, most notably with a larger decrease in the conduction band minimum at the K point relative to the decrease at the Q point with higher applied strain. The strain dependence of the band structure agrees with previous theoretical work on bulk MoS_2, which has a similar band structure to bilayer MoS_2.[87]

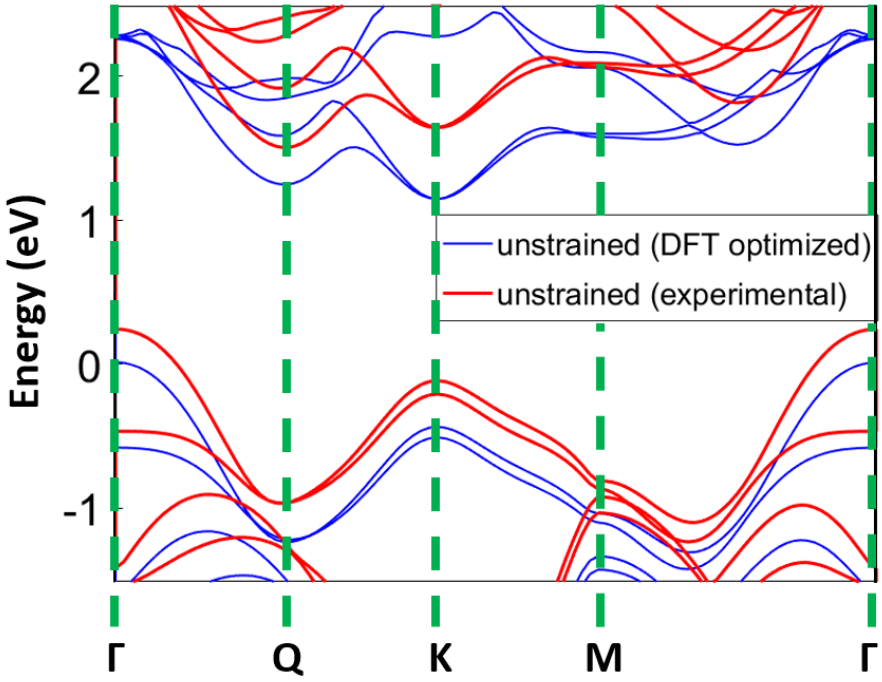

Figure 3.5. Band structures of bilayer MoS_2, calculated via DFT, of both the structure optimized using DFT and structure using experimental lattice parameters. Energy of 0 eV is set to the top of the valence band at the Γ point of the DFT optimized structure.

The calculated band structure for unstrained MoS_2 displays a conduction band minimum at the K point. Experimentally, the conduction band minimum for multi-layer MoS_2 is found between the Γ and K points, denoted as the Q point in Figure 3.5. This qualitative discrepancy between calculated and experimental band structures is the result of our choice of the generalized gradient approximation functional incorporating long range dispersion corrections (GGA+D) functional and the subsequent effect on the lattice parameters following structural optimization, which results in an approximate overestimation of ~2% for the calculated lattice parameters in comparison to experimental values. Previous work has demonstrated that conduction band minimums at the K-point during DFT calculations are the result of an overestimation of the interlayer spacing.[88] In order to confirm that the cause of the discrepancy in calculated and experimental band structures is an overestimation of lattice parameters during structural optimization, the band structure for bilayer MoS_2 is calculated using experimentally determined lattice parameters a = 3.160 Å and c/2 = 6.147 Å. The band structure using the experimental lattice parameters, shown in Figure 3.5, displays a conduction band minimum at the Q point, demonstrating qualitative consistency with experimental results for MoS_2. While the GGA+D functional produces lattice parameters different from the known equilibrium structure, they are still reliable in demonstrating the qualitative effect of strain on the band structure.

Strain-Induced Phonon Shifts

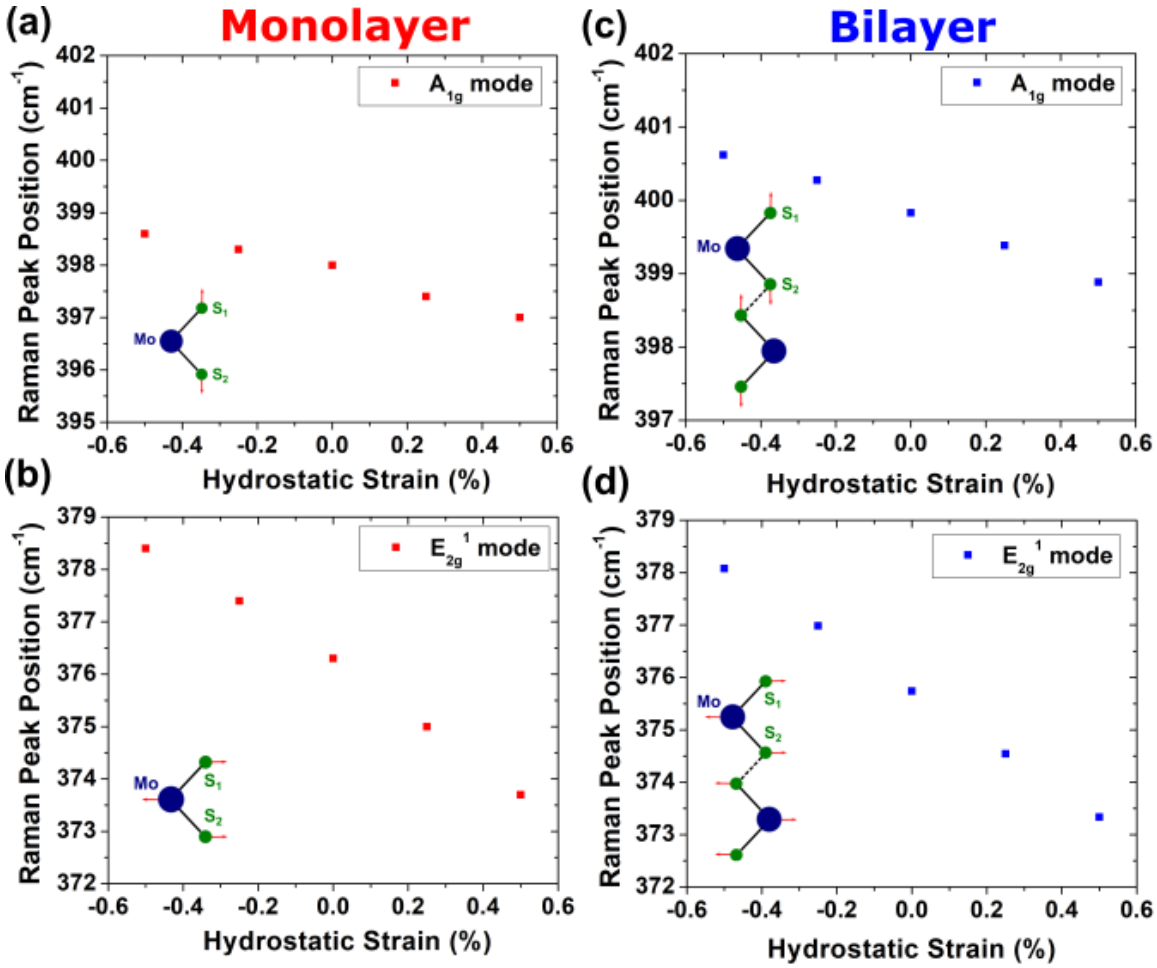

Figure 3.6. Strain dependence of the E^1_{2g} and A_{1g} vibrational modes in monolayer and bilayer MoS_2 calculated using density functional perturbation theory. **(a)** and **(b)** show the behavior of the E^1_{2g} and A_{1g} modes, respectively, with applied in-plane biaxial strain for monolayer MoS_2. **(c)** and **(d)** show the behavior of the E^1_{2g} and A_{1g} modes, respectively, with applied in-plane biaxial strain for bilayer MoS_2. The insets show schematic drawings of the movement of the atoms for the corresponding vibrational modes

As shown in Figure 3.6, for each optimized structure at each strain, zone-center phonon modes were calculated using density functional perturbation theory (DFPT). First order Raman modes for both monolayer and bilayer MoS_2 follow the same strain behavior

with increasing tensile strain, causing a redshift in the Raman peak position for both the E^1_{2g} and A_{1g} vibrational modes. The A_{1g} vibrational mode also shows a larger shift in Raman peak position than the E^1_{2g} vibrational mode. The strain induced on MoS_2 by the Au nanopyramid structures is not completely in-plane or hydrostatic, but the DFT simulations still provide a useful estimation for the strain dependence of the Raman modes.

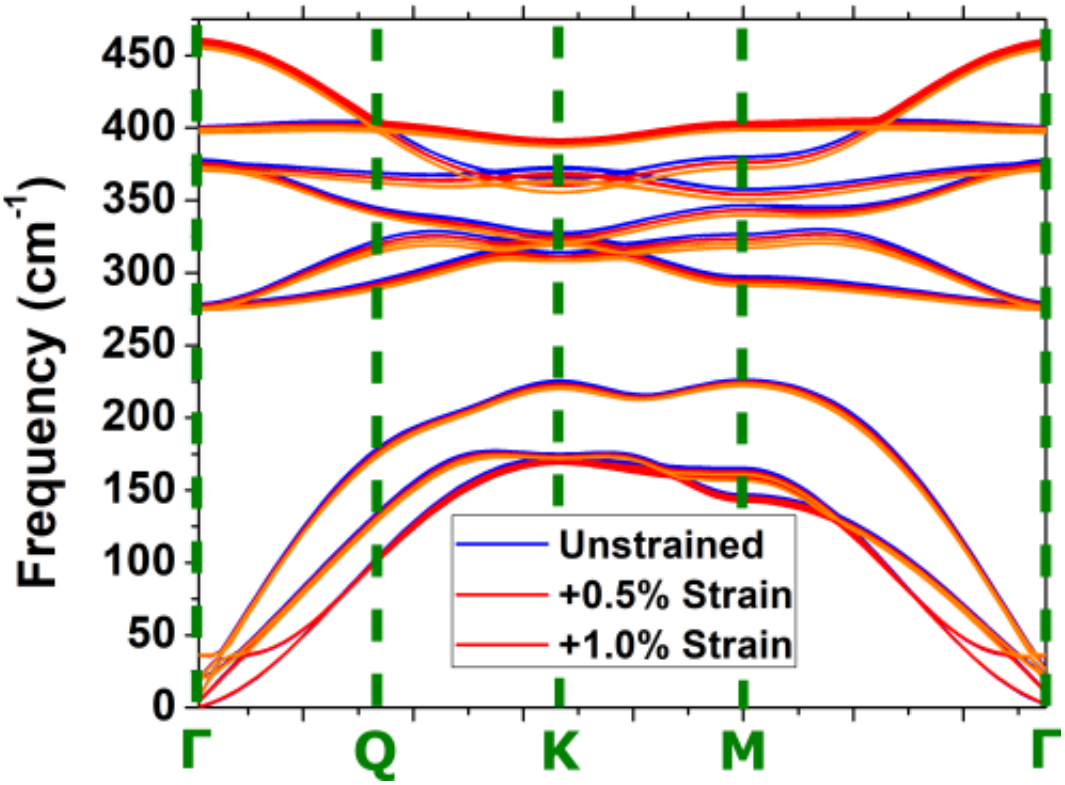

Figure 3.7. The phonon dispersion for both optical and acoustic phonon modes for unstrained (blue curve), +0.5% applied hydrostatic strain (red curve), and +1.0% applied hydrostatic strain (orange curve) bilayer MoS_2. The high symmetry points (Γ, Q, K, M) are indicated by the green dashed lines.

The phonon dispersion for various strains is shown in Figure 3.7. Phonon dispersion was calculated by first calculating dynamical matrices on a uniform grid of 6×6×2 q-points. These data were then used to generate the real-space interatomic force

constant matrix, which could then be used to generate the dynamical matrix at a generic q-point. Simple acoustic sum rules enforcing translational invariance were applied to the dynamical matrices to compensate for the approximations used during calculations.

TERS MEASUREMENTS OF UNSTRAINED MoS_2

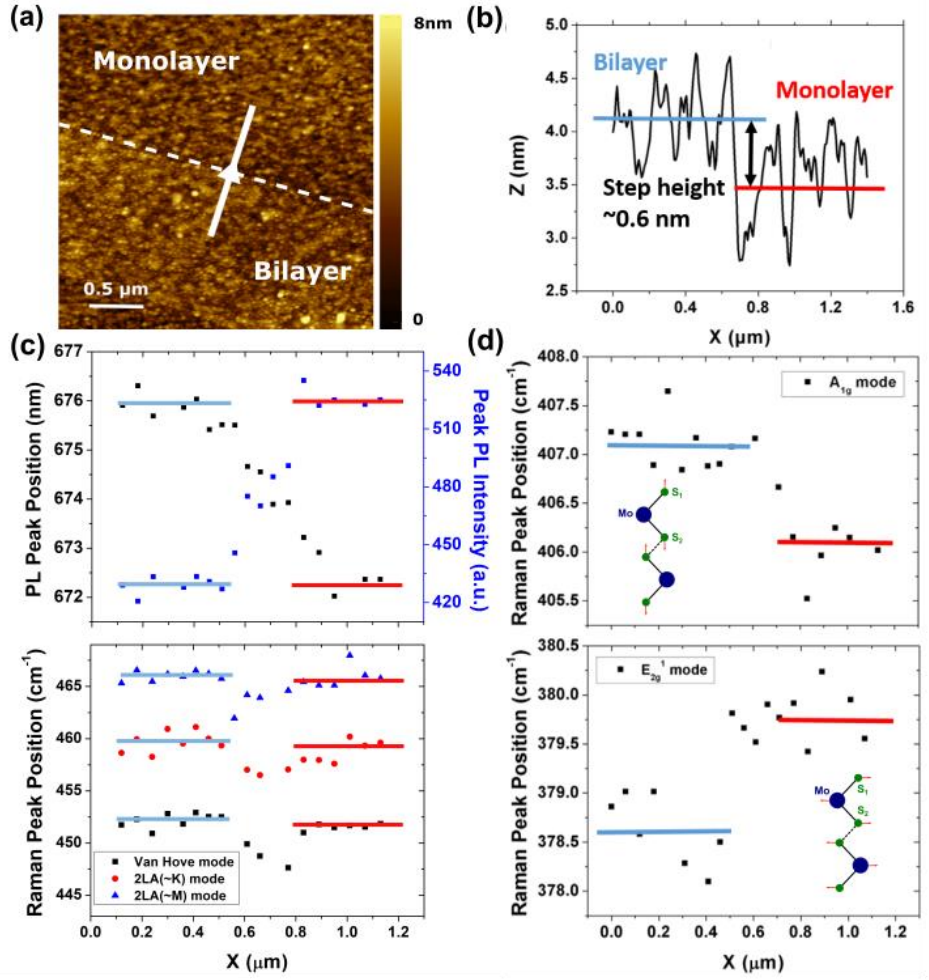

Figure 3.8. **(a)** AFM image of MoS_2 transferred onto a flat Au substrate. The solid white linecut traverses a transition from a bilayer to a monolayer region, delineated by the white dashed line. **(b)** AFM topography for the white linecut shown in **(a)**. The blue and red lines highlight the bilayer and monolayer regions, respectively, with a step height between the regions of ~0.6 nm. TEPL and TERS measurements taken along the linecut in **(a)** across the monolayer to bilayer transition region. The blue and red lines highlight the average constant values in the bilayer and monolayer regions **(c)** (Top Panel) Position of the PL peak associated with the A exciton and trion (black points) and Peak PL intensity (blue points) along the linecut. (Bottom panel) Raman peak positions for the second order Raman modes associated with the van Hove singularity in the phonon DOS and scattering of electrons by longitudinal acoustic phonons near the K and M points in the BZ. **(d)** Raman peak positions for (top panel) first order out-of-plane A_{1g} mode and (bottom panel) second order in-plane E^1_{2g} mode. The insets for the top and bottom panels show schematic drawings for the movement of the atoms in the corresponding vibrational modes.

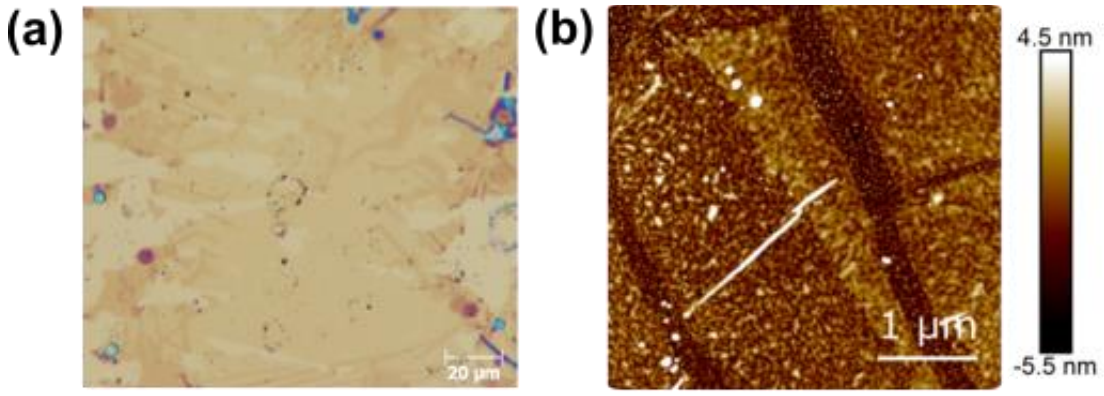

Figure 3.9. MoS_2 transferred onto a flat Au substrate with **(a)** optical and **(b)** atomic force microscopy (AFM) images of typical sample areas

Figure 3.8a shows an AFM image of MoS_2 that has been transferred onto a flat Au substrate. The region shown features both monolayer and bilayer regions where the solid white line indicates a line cut across a transition region from monolayer to bilayer. The topography along the line cut, shown in Figure 3.8b, indicates a clear change in thickness of the sample with a step height of approximately 0.6 nm, which is consistent with the layer thickness of MoS_2 of 0.65 nm found in previous AFM measurements.[89] Optical and AFM images of the larger sample area are shown in Figure 3.9a and 3.9b, respectively.

TEPL and TERS measurements were taken along the same line cut indicated in Figure 3.8b. The layer thickness of MoS_2 is directly detectable using PL and Raman, with PL measurements showing a general decrease in PL intensity [90,91] with increasing layer thickness. In particular, MoS_2 exhibits a transition from direct bandgap for monolayer thickness to indirect bandgap for bilayer thickness, which leads to clear differences in both the PL intensity[90,91] and a shift in the A excitonic peak to longer wavelengths[79] in the PL spectra between monolayer and bilayer MoS_2. The top panel of Figure 3.8c shows the position of the A excitonic PL peak and the peak PL intensity of TEPL measurements taken

along the linecut indicated in Figure 3.8a. The A excitonic PL peak, which is associated with emission from both the uncharged excitons and charged excitons (trions) of the A excitonic transition,[92] is fit to one Lorentzian to determine the peak position. The behavior of the PL peak position and the PL intensity clearly indicates separate monolayer and bilayer regions in the MoS_2 that correspond very well with the topographic transition observed in AFM, with increasing layer thickness resulting, as expected, in a shift to longer wavelengths of the A excitonic peak position as well as decreasing peak PL intensity. As reported in previous work, there is significant PL quenching from the substrate specifically in monolayer MoS_2 that mitigates the change in PL intensity from monolayer to bilayer.[93] The width of the transition region from monolayer to bilayer, which includes TEPL spatial resolution and carrier diffusion lengths, is approximately half a micron**.** The transition region width of the TEPL measurement is comparable to carrier diffusion lengths reported on exfoliated few-layer MoS_2,[94] but it should be noted that the MoS_2 we are measuring contains both monolayer and bilayer regions and is in close proximity to Au.

The top and bottom panels of Figure 3.8d show the behavior of the first order Raman peak positions associated with the out-of-plane A_{1g} and the in-plane E^1_{2g} vibrational modes, respectively, from the TERS measurements taken along the same line cut across the monolayer to bilayer transition region. The insets show corresponding schematics that illustrate the movement of the atoms for the corresponding vibrational modes. In previous work, increasing layer thickness of MoS_2 results in increasing separation between the Raman peaks associated with the E^1_{2g} and A_{1g} modes.[10,9] There is a clear delineation of the monolayer and bilayer regions with the expected behavior of increasing layer thickness resulting in greater separation between the first order Raman modes. The width of the transition region from monolayer to bilayer for the Raman peak position associated with the out-of-plane A_{1g} mode indicates a spatial resolution of approximately 100 nm, well

below the illumination spot size of ~1 μm employed in these measurements. The separation observed between the E_{2g}^1 and A_{1g} modes in the TERS experiments was ~26 cm^{-1} and ~29 cm^{-1} for monolayer and bilayer MoS_2, respectively, which is greater than the corresponding ~19 cm^{-1} and ~22 cm^{-1} separation observed in conventional measurements with a 532 nm excitation laser performed on the same region of interest shown in Figure 3.8a. We believe the increased separation in the TERS measurements is due to a combination of factors. First, in the resonant Raman regime, the E_{2g}^1 Raman peak has noticeable asymmetry with broadening occurring towards lower frequencies which would result in a shift of the peak position of the E_{2g}^1 mode towards lower frequencies and a greater separation between the E_{2g}^1 and A_{1g} modes. Second, the influence of the Au substrate can result in shifts in the peak positions for the E_{2g}^1 and A_{1g} modes. Third, the unique electromagnetic enhancement of the TERS measurements could result in shifts in the peak positions in comparison to the conventional Raman case.

The bottom panel of Figure 3.8c shows the behavior of the second order Raman peak positions of modes associated with the Van Hove singularity in the phonon DOS and LA phonon scattering of excited electrons near the K and M points of the BZ from the TERS measurements taken along the linecut in Fig. 3.8a. The peak positions are relatively unchanged from monolayer to bilayer, however, there is a clear negative shift in the peak positions of all three modes near the interface between the monolayer and bilayer regions. The origin of these negative Raman shifts is currently being investigated.

LOCALLY STRAINED MoS_2 OVER AU NANOPYRAMIDS

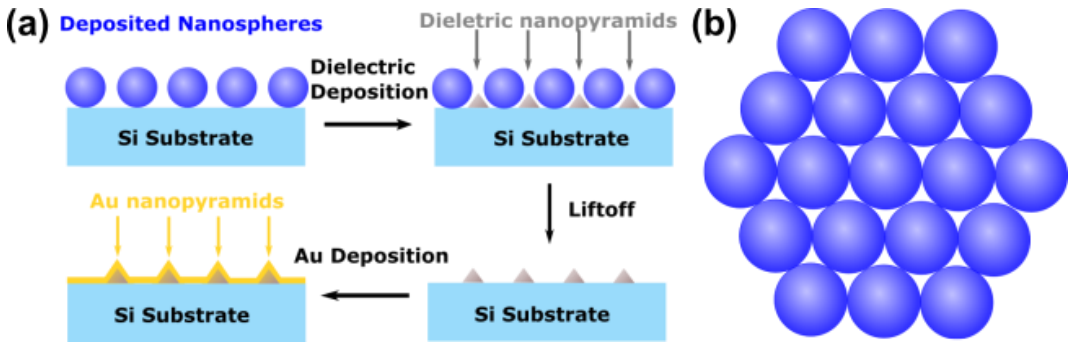

Figure 3.10. (a) Schematic drawings of the fabrication work flow for creating the Au nanopyramid arrays. **(b)** Schematic drawing of self-assembled hexagonal nanosphere array.

By applying strain to MoS_2, we can observe changes in the Raman and PL spectra that elucidate strain dependence in the band structure and phonon dispersion. Using nanosphere lithography, we patterned an array of Au nanopyramids to induce strain on MoS_2. Figure 3.10a shows a fabrication work flow for the creation of Au nanopyramid structures on a Si substrate. First, a clean petri dish was filled approximately three quarters full with deionized (DI) water. A glass slide was then inserted into the petri dish so that one end rest on the bottom surface of the dish and the other end is exposed to air resting on the rim of the petri dish. A solution of equal parts 99.5% anhydrous ethanol and 1 μm polystyrene nanospheres (3% coefficient of variance, 2.6% solids-latex from Polysciences Inc.) was made and micropipetted onto the glass slide in small increments. The solution is then allowed to thin out and roll down the glass slide and enter the bulk DI water. A strong surface tension gradient between the ethanol-nanosphere solution and the DI water causes the nanospheres to self-assemble into ~1 cm^2 monolayers on the air-water interface. A silicon substrate was then used to "scoop up" the monolayers of nanospheres onto the

substrate surface. The wet monolayer was left to dry under a heat lamp. A schematic drawing of the self-assembled hexagonal array of nanospheres is shown in Figure 3.10b. The hexagonal array of nanospheres was then used as a mask for electron beam evaporation of ~100 nm of Al_2O_3 to form the nanopyramid structure. The sample is then sonicated in toluene for 10 seconds to dissolve the nanospheres and reveal the Al_2O_3 nanopyramids. Finally, a 5/65 nm thick Cr/Au bilayer is deposited using electron beam deposition on the substrate, creating Au nanopyramids. The same previously mentioned PDMS stamp transfer process is then used to transfer CVD grown MoS_2 onto the finished patterned substrate. Figure 3.11a shows an SEM micrograph of a patterned Au nanopyramid substrate with MoS_2 successfully transferred.

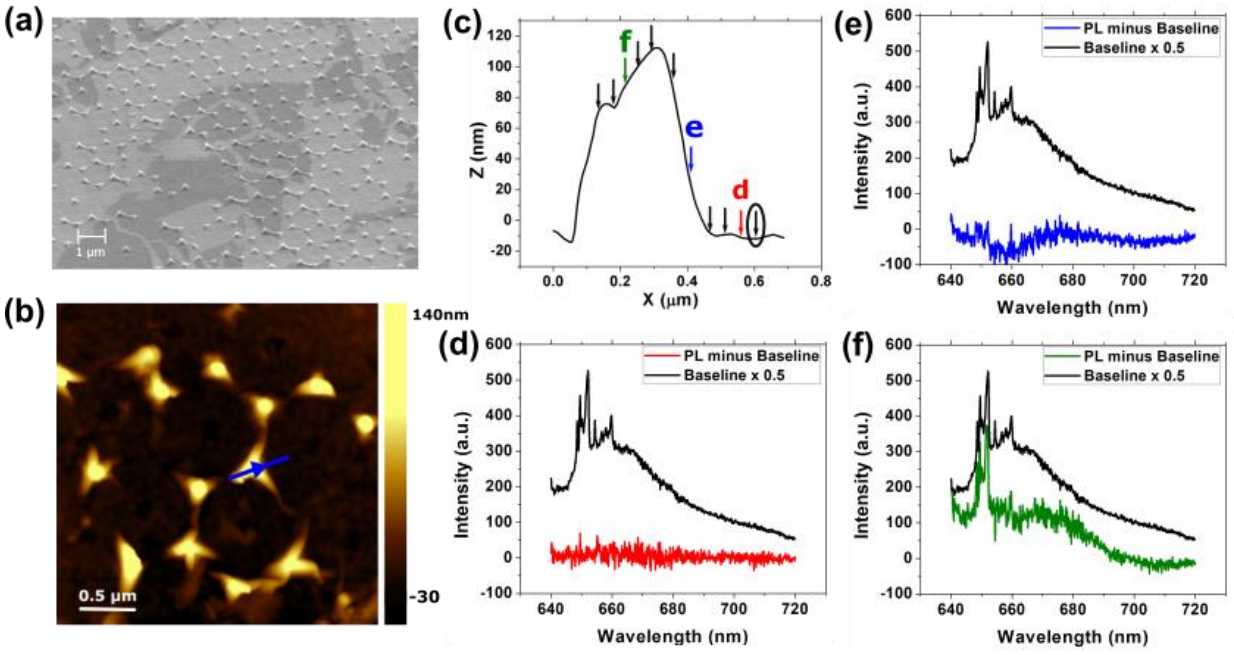

Figure 3.11. **(a)** SEM image of successfully transferred MoS_2 on a patterned Au nanopyramid array. Areas covered by MoS_2 appear darker in the image. **(b)** An AFM image and linecut of bilayer MoS_2 draped over a Au nanopyramid. **(c)** AFM topography along the blue linecut in **(b).** Arrows indicate spatial position where TERS and TEPL measurements were taken. **(d-f)** TEPL spectra taken at points corresponding to the labeled arrows in **(c).** The black baseline PL spectrum is taken at the point indicated by the circled arrow.

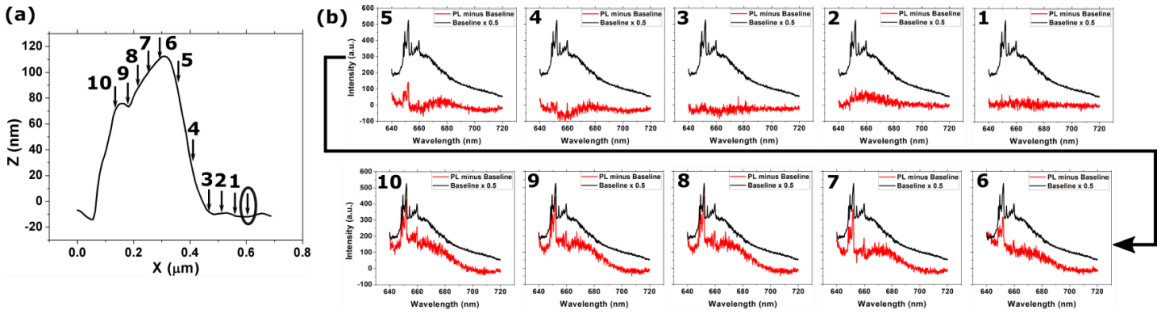

Figure 3.12. **(a)** AFM topography of the Au nanopyramid linecut indicated in Figure 3.11b with arrows indicating the positions where TEPL measurements are taken. The circled arrow indicates where the baseline spectrum is taken. **(b)** Evolution of the photoluminescence spectra along the taken at the points indicated by the corresponding numbered arrows in **(a)**. The baseline PL spectrum (black curve) is taken at the point on the flat Au region indicated by the circled arrow in **(a)**. The PL spectrum at each point (red curve) has the baseline spectrum subtracted.

Figure 3.11b shows an AFM image and linecut of bilayer MoS_2 that has been successfully draped over a Au nanopyramid. The linecut goes from the end of one corner of the pyramid to the apex of the pyramid, where tensile strain would be highest, to finally a relaxed flat region. The topographic profile, shown in Figure 3.11c, yields a maximum height of ~120 nm and width of ~400nm for the MoS_2 draped over the nanopyramid. To estimate the maximum strain induced on the MoS_2 at the apex of the pyramid, we employ two estimation methods: spherical pure bending[95] and buckle delamination[18].

To estimate the maximum strain using the spherical pure bending method, where the structure is modeled as a surface wrapped around a sphere, the following equation is applied:

$$\varepsilon \sim \frac{\frac{t}{2}}{R-\frac{t}{2}} + \varepsilon_{add}\ , \qquad (1),$$

where t is the thickness of the MoS_2 sample, R is the radius of curvature at the apex of the nanopyramid and ε_{add} is the residual strain, which is a fitting parameter. Taking the

thickness to be 1.3 nm, the radius of curvature to be 40 nm and the residual strain to be 0, we estimate a maximum strain of 1.65%.

Approximating the MoS_2 profile as a one-dimensional buckle delamination, we can apply the following equation to estimate a maximum uniaxial strain:

$$\varepsilon \sim \frac{\pi^2 ht}{(1-\sigma^2)\lambda^2}, \quad (2),$$

where t is the thickness of the MoS_2 sample, h is the height of the buckle, σ is Poisson's ratio for MoS_2 and λ is the width of the buckle. Taking the thickness to be 1.3 nm, the height to be 120 nm, Poisson's ratio to be 0.29[44], and the width to be 400 nm, we estimate a maximum strain of 1.06%.

We performed TEPL and TERS measurements at the points indicated by the arrows in Figure 3.11c. Figures 3.11d, 3.11e, and 3.11f show representative PL spectra taken at the points corresponding to the arrows with matching colors, with the red PL spectrum of Figure 3.11d taken at a point on flat Au, the blue PL spectrum of Figure 3.11e taken at a point on the slope of the nanopyramid, and the green PL spectrum of Figure 3.11f taken at a point near the apex of the nanopyramid. The baseline PL spectrum, taken on a flat region, is taken at the point indicated by the circled arrow in Figure 3.11c. The entire evolution of the PL spectra along the linecut is shown in Figure 3.12b. As shown in Figure 3.4c, tensile strain causes a decrease in both the Γ-Q and Γ-K bandgaps in bilayer MoS_2, which is analogous to the change in bandgap in locally strained monolayer MoS_2 that induces an exciton funneling effect that also enhances and shifts to longer wavelength the PL.[18] The blue and green PL spectra in Figures 3.11e and 3.11f, respectively, reveal enhancement of the PL spectrum from ~670 nm to ~690 nm in wavelength, with additional luminescence shifted to longer wavelengths, which indicates a lowering of the bandgap energy in the locally strained bilayer MoS_2. There is also a significant enhancement of the Raman modes

in the green spectrum from ~645 nm to ~660 nm, which indicates that the unique geometry of the tip-sample junction at the apex of the nanopyramid contributes to the TERS enhancement as well as the PL enhancement. The change in geometry especially affects the gap mode that forms between the tip and the Au substrate when the tip is within a few nm of the substrate.

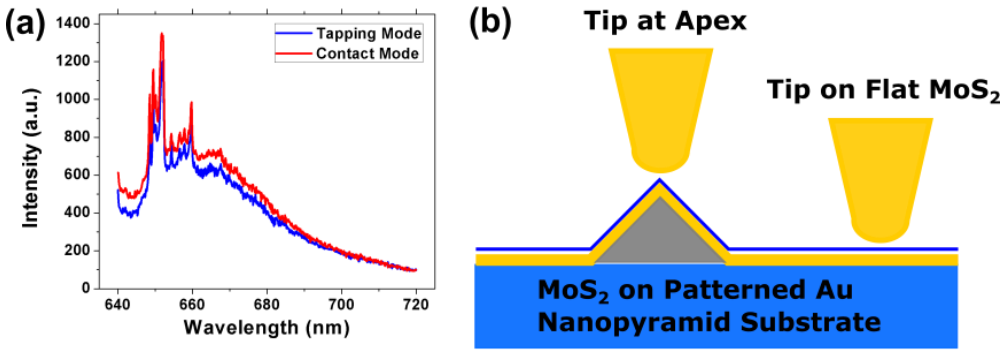

Figure 3.13. **(a)** PL spectrum of MoS2 taken at the same point on a Au nanopyramid substrate in tapping mode (blue curve) and contact mode (red curve). **(b)** Schematic drawing of the tip sample geometry when the Au tip is at the apex of the Au nanopyramid and at the flat region.

Figure 3.13a shows the difference in PL signal intensity when the tip is in tapping mode and in contact mode at the same point for MoS_2. We see an overall increase in the signal intensity when the tip is placed in contact mode compared to tapping mode below ~690 nm in wavelength with no increase in intensity above ~690 nm in wavelength. The increase in signal intensity is expected due to the greater EM field enhancement created by the change in tip-sample geometry that occurs when the tip goes from tapping mode to contact mode. The wavelength dependence of the intensity increase of measurements taken in contact mode versus tapping mode matches the wavelength dependence of the signal intensity increase when comparing measurements taken at the apex of the nanopyramid versus in the flat region, which indicates that the change in EM field enhancement due to

a change in tip-sample geometry contributes to the increase in PL intensity at the nanopyramid apex.

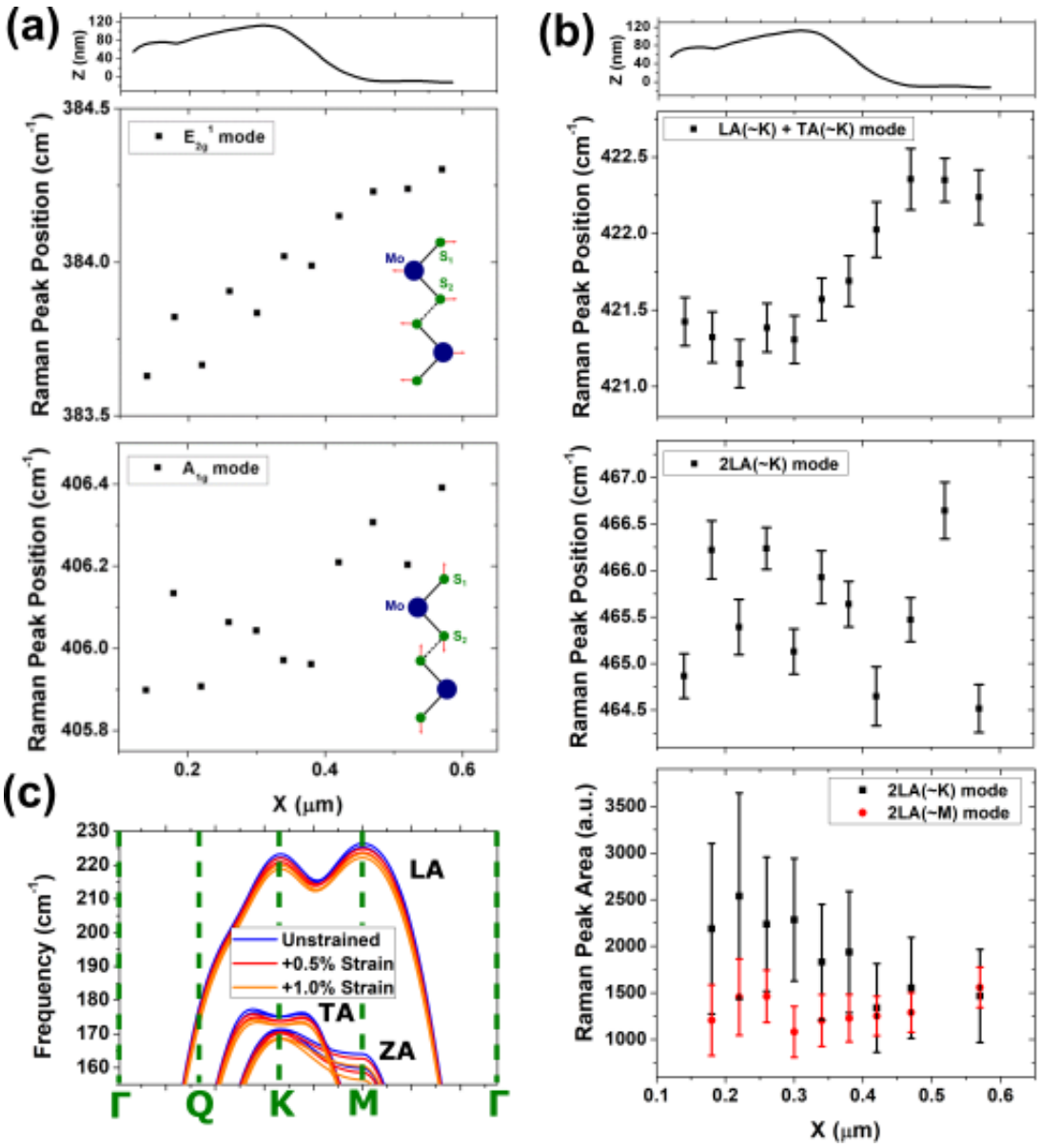

Figure 3.14.

Figure 3.14. (a) (Top panel) AFM topography of the linecut shown previously in Figure 3.11b. Raman peak positions of the first order (2nd panel) E^1_{2g} and **(**bottom panel) A_{1g} vibrational modes along the nanopyramid linecut. The insets show schematic drawings of the movement of the atoms for the corresponding vibrational modes. **(b)** Raman peak positions (with error bars) of the second order modes along the line cut (AFM topography shown in the top panel) related to (2nd panel) longitudinal and transverse acoustic phonon scattering of electrons near the K point in the BZ and (third panel) only longitudinal acoustic phonon scattering of electrons near the K point. (Bottom Panel) Raman peak areas (with error bars) of the second order mode associated with LA phonon scattering of excited electrons near the K point in the BZ (black squares) and the second order mode associated with LA phonon scattering of excited electrons near the M point in the BZ (red circles). **(c)** Phonon dispersion for the acoustic phonon modes calculated using DFT simulations for unstrained (blue curve), +0.5% applied hydrostatic strain (red curve), and +1.0% applied hydrostatic strain (orange curve) bilayer MoS_2. The phonon modes represent the out-of-plane (ZA), in-plane transverse (TA), and in-plane longitudinal (LA) acoustic vibrational modes. The high symmetry points (Γ, Q, K, M) are indicated by the green dashed lines.

Figure 3.14a shows the behavior of the Raman peak positions associated with the E_{2g}^1 and A_{1g} vibrational modes, respectively, from TERS measurements taken along the same linecut of bilayer MoS_2 draped over the Au nanopyramid with corresponding topography indicated in Figure 3.14c. Both the Raman peak positions of the E_{2g}^1 and A_{1g} vibrational modes show a negative shift as the tensile strain increases at the apex of the nanopyramid. The negative shift is larger for the in-plane E_{2g}^1 mode when compared to the out-of-plane A_{1g} mode which agrees with both previous results[10] and DFT simulations. We do not observe significant splitting of the E_{2g}^1 mode due to strain which has been observed to occur at uniaxial strains above 1.0%, which breaks symmetry.[96] The strain induced by the Au nanopyramids is biaxial and does not contribute as significantly to symmetry breaking of the E_{2g}^1 mode.

The effects of strain on the second order Raman modes of MoS_2 have not been previously studied in detail. The second order Raman modes of MoS_2 related to DRR processes are sensitive specifically to changes in the momentum and energy conservation constraints that govern which transitions and states in the BZ participate in resonant interactions and in turn make them a useful tool to observe how strain causes distortions in the electronic band structure. Figure 3.14b illustrates the strain dependence of the second order Raman modes from TERS measurements taken along the same linecut of bilayer MoS_2 draped over the Au nanopyramid with corresponding topography indicated in the top panel. As shown in the second panel of Figure 3.14b, there is a negative shift of the Raman peak position of the second order DRR mode associated with resonant scattering of excited electrons by both LA and TA phonons near the K point in the BZ (peak 3) as the TERS measurement location moves from the relaxed flat region to the region of highest tensile strain at the apex of the pyramid.

Figure 3.14c shows the phonon dispersion for the acoustic phonon modes in bilayer MoS_2 calculated using DFT. The full phonon dispersion is shown in Figure 3.7. With positive applied hydrostatic strain, the calculated phonon dispersion indicates a negative shift in frequency for both the LA and TA vibrational modes at the K point, which would indicate a negative shift in the peak position both for peak 3 as well as for the peak position associated with only LA phonon scattering of excited election near the K point (peak 6). The third panel of Figure 3.14b shows the behavior of Raman peak positions for peak 6, along the linecut of the nanopyramid. The position of peak 6 does not show significant strain dependence; however, experimental uncertainty in determining peak position may obscure strain dependence. From Figure 3.3a, peak 3 is isolated in frequency from the remaining second order modes, which allows it to be fit more accurately and independently from the remaining second order modes, such as peak 6.

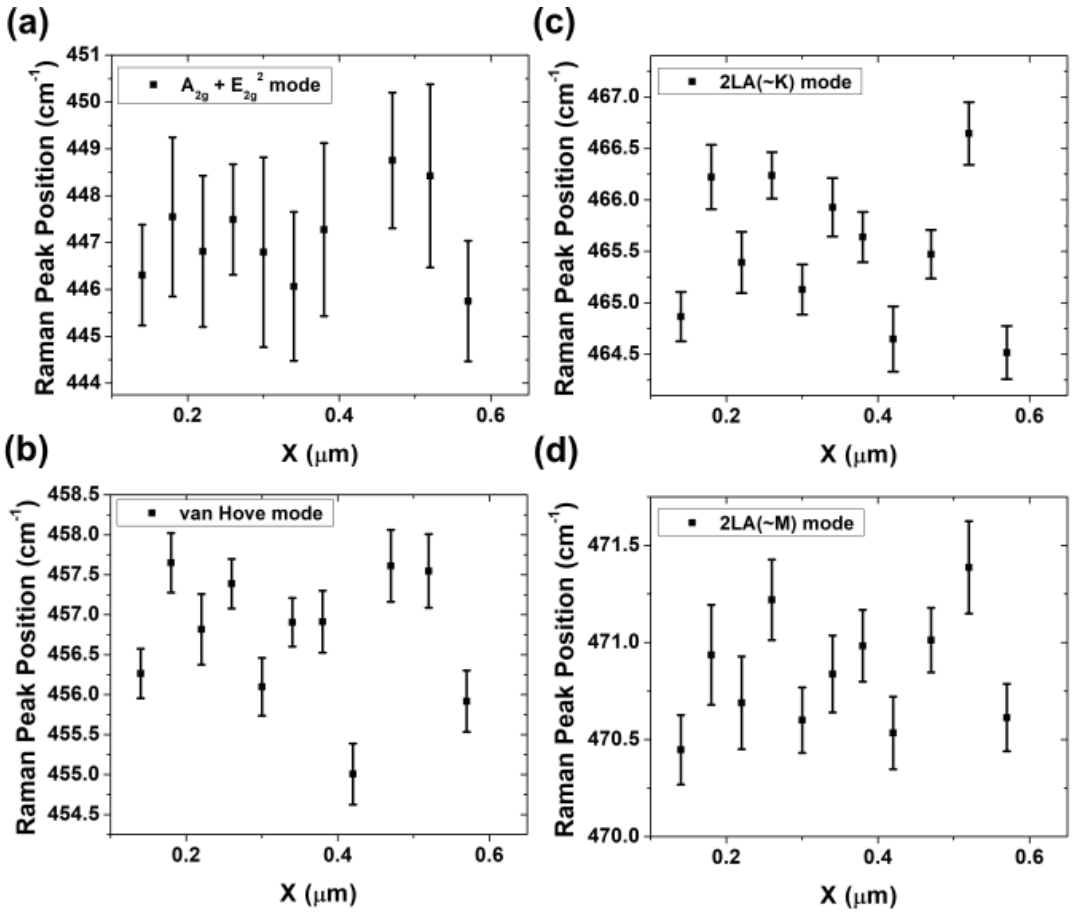

Figure 3.15. Raman peak positions (with error bars) of the second order modes along the line cut (shown in Figure 3.11b, with AFM topography shown in Figure 3.11c) related to **(a)** a combination of the A_{1g} and E_{2g}^2 vibrational modes, **(b)** the van Hove singularity, and **(c, d)** scattering of excited electrons by two LA phonons near the K point and M point of the BZ, respectively.

Figure 3.15 shows the behavior of the peak positions of the remaining 2nd order Raman modes along the same linecut of bilayer MoS_2 draped over the Au nanopyramid with corresponding topography indicated in Figure 3.11c within the broad 2nd order Raman band at 430 cm^{-1} to 475 cm^{-1}. The Raman peak positions appear to be strain independent, however, because the Raman modes are in such close proximity to each other in regards to

spectral position, small trends in peak position could be obscured due to experimental uncertainty.

We also observe a change in the peak areas of the second order modes relative to each other. The bottom panel of Figure 3.14b shows Raman peak areas of the second order mode associated with LA phonon scattering of excited electrons near the K point in the BZ (peak 6) and the second order mode associated with LA phonon scattering of excited electrons near the M point in the BZ (peak 7). From the figure and the corresponding topography, there is a clear increase in the area of peak 6 relative to that of peak 7 as tensile strain increases near the apex of the nanopyramid. A decrease in the peak area of peak 6 relative to that of peak 7 has been previously observed in connection with the transition from monolayer to multilayer MoS_2, where the K point and Q point conduction band minima become closer in energy as seen in Figure 3.4a and 3.4b.[54] In the monolayer case, when the K point conduction band minimum is lower in energy than the Q point conduction band minimum, K to K' transitions mediated by the $\mathbf{q}_{\sim K}$ acoustic phonons are much more prominent than K to Q transitions mediated by $\mathbf{q}_{\sim M}$ phonons, as seen from the phonon density of states for allowed DRR processes in monolayer MoS_2, as shown in Reference 54. In bilayer MoS_2, because the difference in energy decreases between the K and Q points conduction band minima, many more transitions mediated by the $\mathbf{q}_{\sim M}$ phonons will satisfy the constraints on a DRR process, which in turn increases the peak area of peak 7 relative to that of peak 6. Figure 3.4c shows that with increased tensile strain, the conduction band minimum at the K point has a greater decrease in energy than the conduction band minimum at the Q point, which results in increased $\mathbf{q}_{\sim K}$ phonon mediated transitions relative to $\mathbf{q}_{\sim M}$ phonon mediated transitions, The increase in $\mathbf{q}_{\sim K}$ phonon mediated transitions relative to $\mathbf{q}_{\sim M}$ phonon mediated transitions is directly observed

through an increase in the peak area of peak 6 relative to peak 7, which we see in the regions with greater tensile strain near the apex of the nanopyramid.

CONCLUSIONS

In conclusion, we have probed monolayer and bilayer MoS_2 with TERS and TEPL and achieved submicron spatial resolution. Furthermore, we have locally strained bilayer MoS_2 using patterned Au nanopyramids and observe enhanced and shifted PL spectra in the areas of localized tensile strain, which we attribute to both a reduction in the bandgap as well as greater plasmonic enhancement from the gap mode. We have also, for the first time, probed the strain dependence of the second order Raman spectrum in bilayer MoS_2, which shows variations that we attribute to changes in the electronic band structure and phonon dispersion due to tensile strain. By performing DFT simulations, we show that applying tensile strain affects the energy level of the conduction band minimum as well as the acoustic phonon dispersion, which confirms that changes in the second order Raman spectrum functions as a useful probe for band structure and phonon mode behavior. Thus, resonant TERS characterization is shown to provide a powerful probe of strain, luminescence, electronic band structure, and phonon dispersion at the nanoscale. The information learned from these studies is likely to be important for a variety of TMD-based devices including quantum emitters, and devices exploiting piezoelectric or flexoelectric effects at the nanoscale.

Chapter 4: Raman Behavior in Strained Monolayer and Three-Layer WSe_2

INTRODUCTION

WSe_2 is a versatile TMD that has been used as the channel material in high mobility transistors[55,56], is a direct band gap semiconductor in the monolayer regime[59], and when locally strained has demonstrated quantum emission at low temperatures.[48,49] Additionally, monolayer lateral heterojunctions of different TMDs have been successfully achieved[97,98], where the lattice mismatch at the interface could be used to tailor the electronic structure of the heterojunctions via strain engineering. Precise measurements of strain in WSe_2 and other TMDs will be needed to fully understand electrical and optical properties of this material system.

Raman spectroscopy has been used to probe layer thickness in WSe_2[99] and changes in strain in other TMDs, such as MoS_2,[10,79] through a systematic study of the behavior of the prominent Raman peaks. The effects of strain on the phonon modes in WSe_2 has been studied theoretically,[100] but a systematic experimental Raman study of the effect of mechanical strain on monolayer WSe_2 has not previously been reported.

We present Raman spectroscopy studies of monolayer and three-layer WSe_2 under applied uniaxial strain. Samples are prepared by transferring mechanically exfoliating WSe_2 onto polyethylene terephthalate (PET) sheets, which are then mechanically stretched to apply tensile strain to the transferred WSe_2 flakes. Spatially resolved Raman spectroscopy is performed on monolayer and three-layer WSe_2 as a function of applied tensile strain. Via detailed mechanical analysis that has been applied for graphene-substrate systems[101], we prove that there is almost full transfer of strain from the PET substrate to the WSe_2. As uniaxial strain is applied onto both monolayer and three-layer WSe_2 regions, there is a splitting of the high intensity Raman peak associated with the frequency

degenerate A' and E' modes in monolayer (A_{1g} and E_{2g}^1 in three-layer) WSe_2, arising from a negative frequency shift of the in-plane E' (E_{2g}^1) mode. Tensile strain also causes a negative frequency shift of the Raman band associated with second order longitudinal acoustic phonon interactions (2LA) in both monolayer and three-layer WSe_2 as well as a negative shift in frequency to the three-layer only peak. From the measured strain behavior of the Raman peaks, we experimentally determine deformation potentials for the strain induced Raman shifts for the various Raman modes for monolayer and three-layer WSe_2, and show that these agree well with theoretical behavior calculated using DFT.

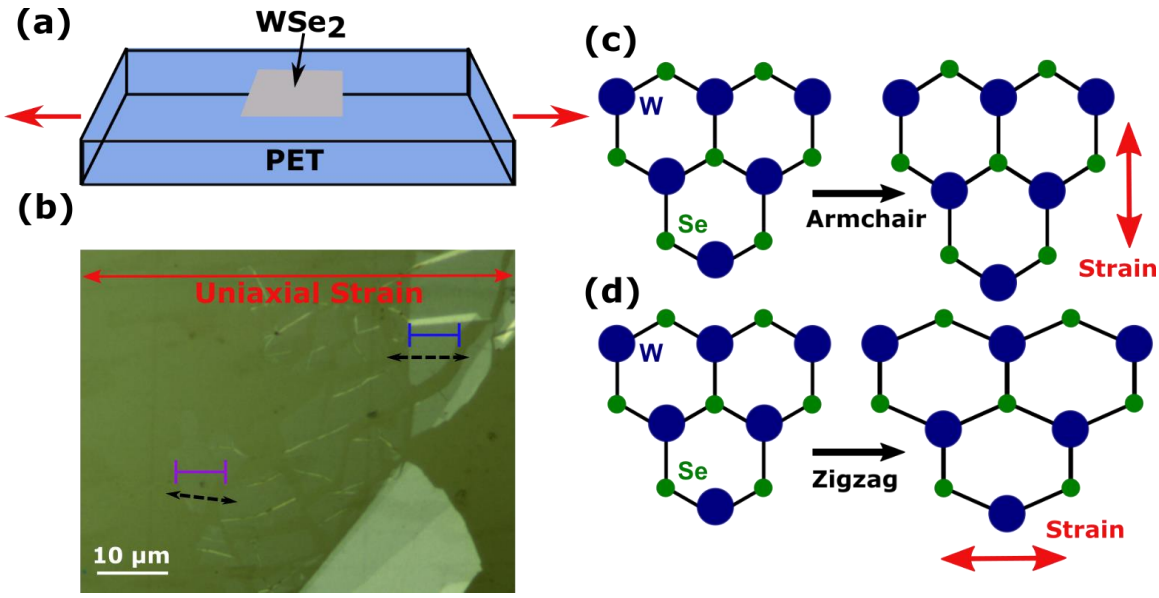

Figure. 4.1 (a) Schematic diagram (not to scale) of the WSe_2 on PET strain experiment with the red arrows indicating the direction of uniaxial strain applied to the PET. **(b)** Optical image of exfoliated WSe_2 flakes on the stretched PET substrate. The red arrows indicate the axis along which the uniaxial strain is applied. The purple and blue lines indicate the region from which line scans of the Raman spectra were obtained for monolayer and three-layer WSe_2, respectively. The dashed black lines indicate the zigzag direction for both monolayer and three-layer WSe_2 flakes, which were determined using second harmonic generation. **(c, d)** Top view of monolayer WSe_2 and the effect on the lattice structure of applying uniaxial tensile strain in the **(c)** armchair direction and **(d)** zigzag direction.

Fig. 4.1a shows a schematic diagram of the experimental setup for applying uniaxial strain to WSe_2. The WSe_2 employed in these experiments was first mechanically exfoliated from commercial bulk crystal purchased from HQ Graphene. A polypropylene carbonate (PPC) coated polydimethylsiloxane (PDMS) dot was used to pick up and deposit the exfoliated WSe_2[102] on a PET substrate. Uniaxial tensile strain was applied to the WSe_2 flakes by stretching the underlying PET substrate. Using a custom sample stretcher, we

first secure either end of the PET strip with screw-tightened clamps and then separate the clamps using a rotating threaded shaft. The applied strain is calculated by measuring the change in distance between the inner portion of the two clamps, which is equal to the amount the PET was stretched.

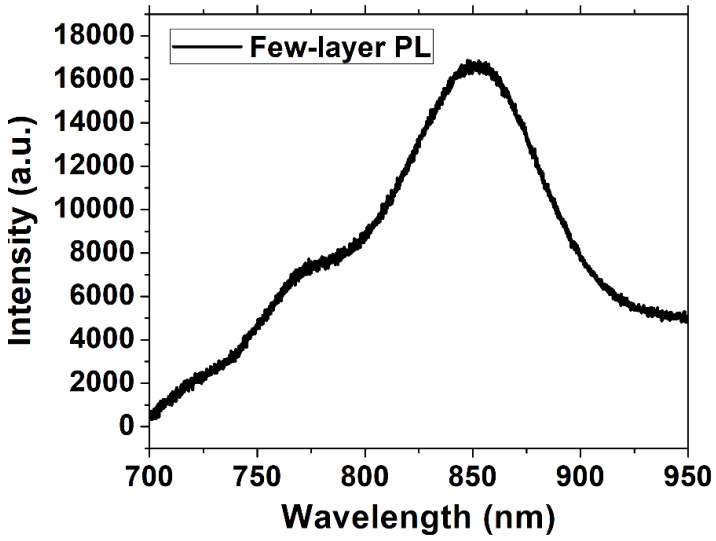

Figure 4.2. Photoluminescence measurement of few-layer WSe_2 flake with the background PET signal subtracted.

Figure 4.1b shows an optical image of exfoliated WSe_2 flakes on the stretched PET substrate with the direction of the uniaxial applied strain indicated in red. Layer thicknesses of the WSe_2 flakes were determined using Raman and PL measurements, with the monolayer regions easily identifiable due to the bright PL signal and the absence of a Raman peak at ~310 cm^{-1}. In Figure 4.2, we see the PL spectrum of the few-layer WSe_2 flake shown in Figure 4.1b. The background PET PL signal has been removed and the remaining PL spectrum shows a main peak centered at ~850 nm, which indicates a three-layer thick WSe_2 flake based on previously reported Raman measurements.[103] Raman line scans across the WSe_2 flakes were performed in the areas indicated by the purple and blue

lines on Figure 4.1b for monolayer and three-layer WSe_2, respectively. Measurements on WSe_2 flakes of odd numbered layers allows determination of the orientation of the flakes through second harmonic generation with the orientation of the zigzag direction indicated by the dashed black lines in Figure 4.1b in both monolayer and three-layer flakes.[104] From the orientation of the flakes relative to the stretching direction, we conclude that in both the monolayer and three-layer flakes, the strain is applied along approximately the zigzag direction. The orientations of strain applied along the armchair and zigzag directions are shown schematically in Figures 4.1c and 4.1d, respectively.

All Raman spectroscopy and photoluminescence measurements were performed with a Renishaw inVia confocal Raman system with a backscattering geometry at an excitation wavelength of 532 nm. A 100 X top objective illuminates the sample normal to the surface with a spot size of ~1 μm and an incident laser power of 375 μW, conditions for which local heating was not found to affect the Raman measurements.

COMPUTATIONAL DETAILS

To further corroborate our experimental results, we performed first-principles plane wave calculations within density functional theory (DFT) executed in the Plane-Wave Self-Consistent Field (PWscf) package of Quantum Espresso[81] using ultrasoft pseudopotentials[82,105] The exchange correlation potential was approximated by a generalized gradient approximation (GGA) using the Perdew-Burke-Ernzerhof (PBE) functional.[106] Dispersion corrections using the DFT-D2 method[84] were used during structural optimizations to determine the interlayer spacing in bilayer WSe_2 structures. A vacuum spacing exceeding 10 Å was employed in the unit cells in order to separate adjacent supercells. A kinetic energy cutoff of 120 Ry was used, and the Brillouin zone was sampled using a Monkhorst-Pack grid[85] of 25×25×1 and 15×15×3 k-points for monolayer and

bilayer calculations, respectively. Atomic positions and lattice constants were optimized using damped molecular dynamics and the quick-min Verlet algorithm. The Hellmann-Feynman force acting on each atom was limited to under 3×10^{-7} Ry per atomic unit in the monolayer case, and 1×10^{-6} Ry in the bilayer case. The pressure in the unstrained unit cell was limited to less than 0.1 kbar. Structural optimizations yielded a lattice parameter of a = 3.328 Å, which is within 2% of the experimentally measured lattice parameter of 3.280 Å[107]. The calculated interlayer W-W spacing for bilayer WSe_2 is 7.034 Å. Strain was applied to the lattice in the form of uniaxial strain along the zigzag direction, utilizing a Poisson ratio of 0.34, which is that of the PET substrate to which the WSe_2 flakes are adhered.[108] Within each strained unit cell, atomic positions were relaxed in all directions. Phonon vibrational frequencies were calculated using DFPT as implemented in the PHonon package of Quantum Espresso.

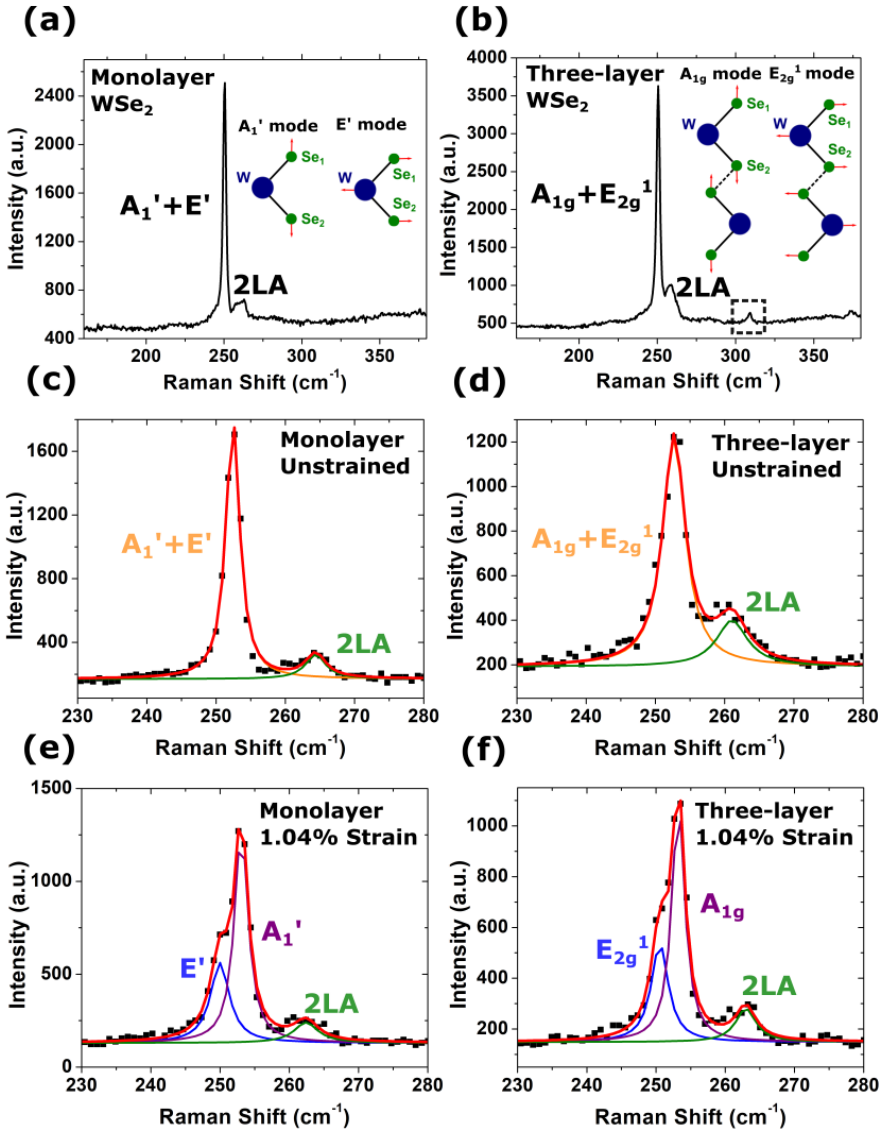

Figure 4.3. Representative Raman spectra for **(a)** monolayer and **(b)** three-layer WSe_2 with the corresponding vibrational modes shown in the insets. The dashed box in **(b)** indicates the peak seen only in three-layer WSe_2. Raman spectra of unstrained monolayer **(c)** and three-layer **(d)** WSe_2. Both spectra are fitted to two Lorentzian peaks within the frequency range 230 to 280 cm^{-1}: one peak in orange for the frequency degenerate A_1' and E' modes in monolayer and A_{1g} and $E_{2g}{}^1$ modes in three-layer WSe_2 and one peak in green for the second order longitudinal acoustic phonon mode (2LA). Raman spectra of monolayer **(e)** and three-layer **(f)** WSe_2 with 1.04% applied uniaxial strain. Both spectra are fitted to three peaks due to splitting of the A_1' and E' modes in monolayer and A_{1g} and $E_{2g}{}^1$ modes in three-layer WSe_2. The sum of the fitted peaks is shown in red and shows good agreement with the measured data represented by the black points.

Figures 4.3a and 4.3b show the Raman spectra for unstrained monolayer and three-layer WSe_2, respectively. The highest intensity peak represents a superposition of the out-of-plane A_1' and in-plane E' vibrational modes for monolayer (A_{1g} and E_{2g}^1 vibrational modes for few-layer) WSe_2, which are nearly frequency degenerate for unstrained material. The weaker and broader peak at ~260 cm^{-1} is associated with a second order interaction related to longitudinal acoustic phonon modes (2LA) near the M point in the Brillouin zone.[109] Vibrational mode assignments were based on previous experimental work corroborated by ab-initio calculations.[103] For layer thicknesses greater than a monolayer, there is an additional low intensity peak, located at ~310 cm^{-1} and indicated by the dashed box in Figure 4.3b. It has been equivalently referred to either as the A_{1g}^2 vibrational mode in even layer number WSe_2 and the $A_1'^2$ vibrational mode in odd layer number WSe_2[103] or the out-of-phase A_{2u} IR active vibrational mode when it becomes Raman active due to Davydov splitting.[110]

To analyze the behavior of the Raman modes as strain is applied, we fit the various modes to Lorentzian peaks. For both monolayer and three-layer materials, we fit the Raman modes from ~240 cm^{-1} to ~280 cm^{-1} in frequency with two Lorentzian peaks at applied uniaxial strains below 0.58% for monolayer and 0.5% for multilayer because of the frequency degeneracy of the in-plane and out-of-plane modes. Figures 4.3c and 4.3d show the peak fitting for Raman spectra from unstrained monolayer and three-layer WSe_2, respectively. We fit an additional Lorentzian to the multilayer only peak for the spectra obtained from the three-layer flake. Fitting of the Raman spectra from the unstrained monolayer flake yields peak positions of 252 cm^{-1} for the frequency degenerate A_1' and E' peak and 264 cm^{-1} for the 2LA peak in monolayer WSe_2.[99] Fitting of the Raman spectra from the three-layer flake yields peak positions of 253 cm^{-1} for the frequency degenerate A_{1g} and E_{2g}^1 peak, 261 cm^{-1} for the 2LA peak, and 305 cm^{-1} for the multilayer-only peak in

three-layer WSe_2.[99] Figures 4.3e and 4.3f clearly show the splitting of the in-plane E' mode and the out-of-plane A_1' mode in monolayer WSe_2 and the splitting of the in-plane $E_{2g}{}^1$ mode and the out-of-plane A_{1g} mode in three-layer WSe_2, which both result from the negative shift of the in-plane mode that becomes apparent when greater uniaxial tensile strain is applied. Once the splitting between the in-plane and out-of-plane modes becomes apparent, we fit the Raman spectra from ~240 cm^{-1} to ~280 cm^{-1} to three peaks corresponding to the in-plane mode, the out-of-plane mode, and the 2LA mode.

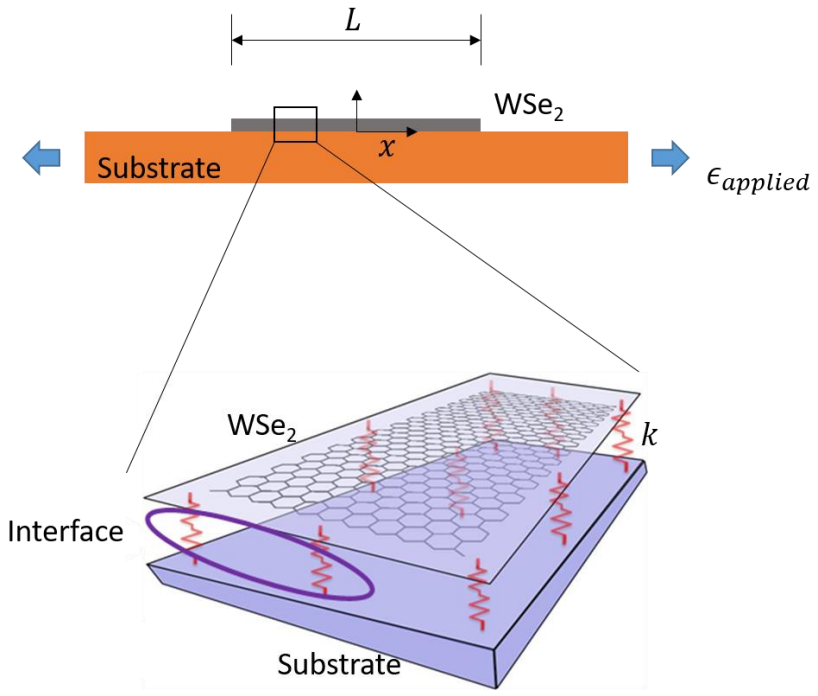

Figure 4.4. Illustration of the mechanical interaction between the WSe_2 flake and substrate assumed for linear shear lag theory.

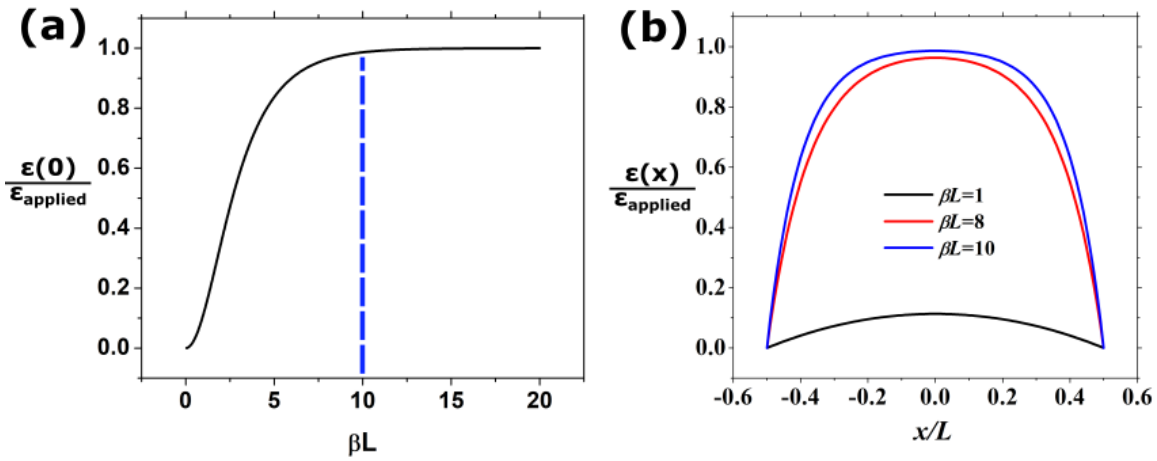

Figure 4.5. **(a)** The percentage of strain transferred to the center of WSe_2 in relation to βL. The blue dashed line indicates the approximate βL value for the monolayer and three-layer flakes used in the these experiments. **(b)** Transferred strain profile across a flake for βL values of 1, 8, and 10 shown with the black, red, and blue curves, respectively

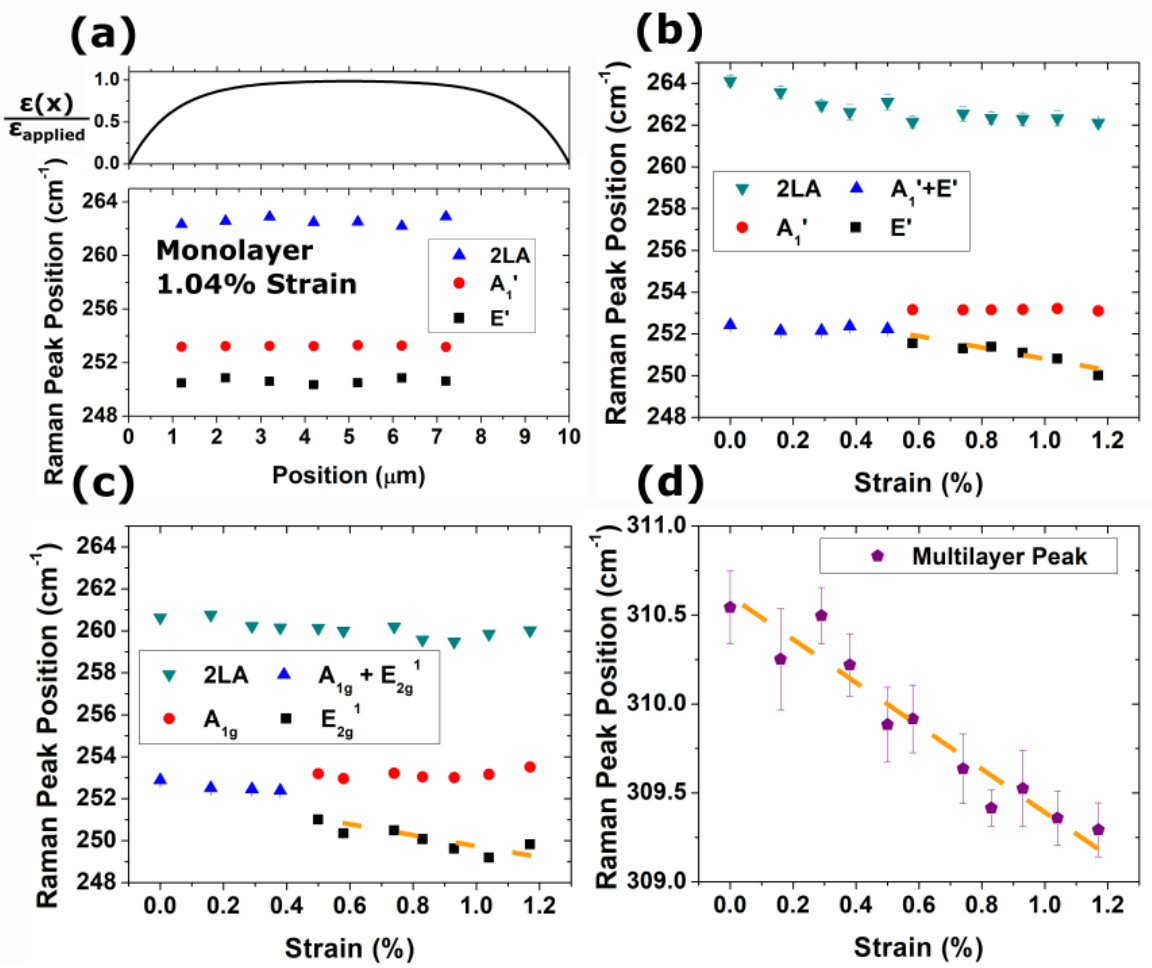

Figure 4.6. (a) (Top panel) Calculated strain distribution across a monolayer flake approximately 10 μm in length along the applied strain axis. (Bottom panel) Raman peak positions (with error bars) across a monolayer flake with 1.04% applied uniaxial strain. Raman peak positions (with error bars) for the 2LA, out-of-plane (A_1' for monolayer and A_{1g} for three-layer), and in-plane (E' for monolayer and E_{2g}^1 for three-layer) Raman modes with increasing uniaxial tensile strain for **(b)** monolayer and **(c)** three-layer WSe_2. At strains below 0.5%, the in-plane and out-of-plane modes are approximately frequency degenerate and are fitted to a single Lorentzian with peak positions indicated by the blue triangles. At strains above 0.5%, peak splitting becomes clearly observable and the in-plane and out-of-plane modes are fit to two peaks. **(d)** Raman peak positions (with error bars) of the multilayer-only Raman mode from the three-layer flake with increasing uniaxial tensile strain. The orange dashed lines indicate the fitted lines used to obtain the strain induced Raman shifts for the in-plane and the multilayer-only Raman modes.

We have performed analyses of the strain transfer from PET to WSe_2 based on linear shear lag theory for flakes of approximately 10 μm in length along the applied strain axis, which is the approximate size of both the monolayer and three-layer flakes. Linear shear lag theory estimates the percentage of strain transferred to the center of a small flake when applying strain to the substrate to which the flake is attached. The transferred strain is a function of the position on the sample following the equation[101]:

$$\epsilon(x) = \epsilon_{applied}\left(1 - \frac{cosh(\beta x)}{cosh(\beta L/2)}\right), \quad (1)$$

where $\epsilon(x)$ is the strain distribution in WSe_2, $\epsilon_{applied}$ is the applied strain on the substrate, L is the length of the WSe_2 flake, and β is the interface parameter. $\beta = \sqrt{\frac{k}{E_{2D}}}$, where k is the effective interface spring constant and E_{2D} is the 2D stiffness of WSe_2. We take E_{2D} to be 115 N/m for WSe_2[111] and k to be 132 TPa/m, the value measured for graphene on polymeric substrate including PET .[101] It would give us an estimated $\beta \sim 1\ \mu m^{-1}$. Figure 4.5a shows the percentage of strain transferred as a function of βL. WSe_2 flakes of lengths 10 μm (monolayer) and 8 μm (three layer) along the strain axis would suggest strain transfer of approximately 98% and 96%, respectively. Figure 4.5b plots the transferred strain profile for βL values of 1, 8, and 10 calculated from similar analyses for graphene[101] and using the same E_{2D} and k values as was used for the shear lag theory calculation. For large βL, the strain distribution can show a plateau towards the center of the flake.

To ensure that we have achieved near complete strain transfer from the uniaxially strained PET sheet to the WSe_2 flakes, we have taken Raman measurements across the length of the flake along the applied strain axis to observe the variation in Raman peak position based on position. The bottom panel of Figure 4.6a shows the peak positions of the A_1', E', and 2LA modes for monolayer MoS_2 with ~1.04% uniaxial strain applied to the PET substrate, with similar results obtained for three-layer WSe_2. The top panel of

Figure 4.6a shows the calculated ratio of strain transferred to the sample over strain applied to the PET substrate on a sample of WSe_2 of 10 μm in length along the applied strain axis. According to a simple linear shear lag theory, the strain transfer efficiency depends on the length of the sample and interface stiffness.[112,113] By adopting the interface stiffness measured from the graphene-PET interface, monolayer and three-layer WSe_2 flakes of lengths 10 μm and 8 μm along the strain axis, respectively, would have a strain transfer of approximately 98% and 96%, respectively. In addition, the analysis predicts a plateau-like strain distribution along the center of the flake for our monolayer sample, which agrees with the constant Raman peak positions across the center of the flake. In fact, a higher interface stiffness can be expected for the WSe_2-PET interface due to the relative softness of WSe_2 compared with graphene. This implied that the above-mentioned strain transfer ratio (98% and 96%) might be underestimated, calling for further detailed characterization on the mechanics of WSe_2-PET interface. We thus suggest that we have achieved close to complete strain transfer from the PET substrate to the WSe_2.[101] Additionally, we anticipate some nonuniformity in the transfer of strain to the top two layers of the three-layer WSe_2 flake due to the van der Waals interaction between the layers. A limited degree of nonuniformity would be consistent with the broader width of the E_{2g}^1 peak in the three-layer WSe_2 relative to the width of the E' peak in the monolayer WSe_2. While the degree of nonuniformity in strain transfer to the top two layers of the three-layer flake is difficult to estimate quantitatively, and we therefore do not attempt to do so, our measurements may somewhat underestimate the effect of strain on the Raman behavior for the three-layer flake.

Figures 4.6b and 4.6c show the dependence of the peak positions of the Raman modes on uniaxial tensile strain for monolayer and three-layer WSe_2, respectively. Table 4.1 shows a summary of the experimentally determined strain induced Raman shifts. In

the monolayer case, the 2LA peak show a negative shift with increasing tensile strain, with a linear fit yielding a strain induced Raman shift of -1.4 ± 0.3 cm^{-1} per % strain. Due to the frequency degeneracy of the A_1' and E' modes in WSe_2, the linear negative shift of the in-plane E' mode is not clearly visible for strains less than 0.58%, at which point splitting of the two modes becomes clearly observable. We therefore perform a linear fit for the data points of 0.58% strain and higher, indicated by the orange dashed line, which yields a strain induced Raman shift for the E' mode of -2.5 ± 0.5 cm^{-1} per % strain. The out-of-plane A_1' mode shows minimal response to strain and the peak position remains constant. We performed the same analysis of the Raman modes for three-layer WSe_2, obtaining a strain induced Raman shift of -0.80 ± 0.2 cm^{-1} per % strain for the 2LA mode and -2.1 ± 0.8 cm^{-1} per % strain for the in-plane E_{2g}^1 mode for strains of 0.5% and above when splitting is easily observable in the Raman spectra. We also see a minimal response to strain for the out-of-plane A_{1g} mode in three-layer WSe_2. Fig 4.6d shows the behavior of the multilayer only peak from the three-layer flake, which also follows a negative linear trend as more tensile strain is applied and yields a strain induced Raman shift of -1.2 ± 0.2 cm^{-1} per % strain. Because the multilayer only peak is isolated in frequency and shows linear strain dependence in the Raman peak position, it is particularly useful for straightforward strain detection in multilayer WSe_2.

Table 4.1. Experimentally determined and DFT calculated strain induced Raman shifts for monolayer and three-layer WSe_2.

	A_1', A_{1g} (cm^{-1}/%)	E', E_{2g}^1 (cm^{-1}/%)	2LA(M) (cm^{-1}/%)	Multilayer-Only (cm^{-1}/%)
Monolayer (Exp.)	0	-2.5 ± 0.5	-1.4 ± 0.3	N/A
Three-layer (Exp.)	0	-2.1 ± 0.8	-0.80 ± 0.2	-1.2 ± 0.2
Monolayer (DFT)	~0	-1.8 ± 0.1 (−) ~0 (+)	-0.94 ± 0.1	N/A
Bilayer (DFT)	~0	-1.9 ± 0.01 (−) ~0 (+)	N/A	-1.1 ± 0.002 (out-of-phase A_{2u})

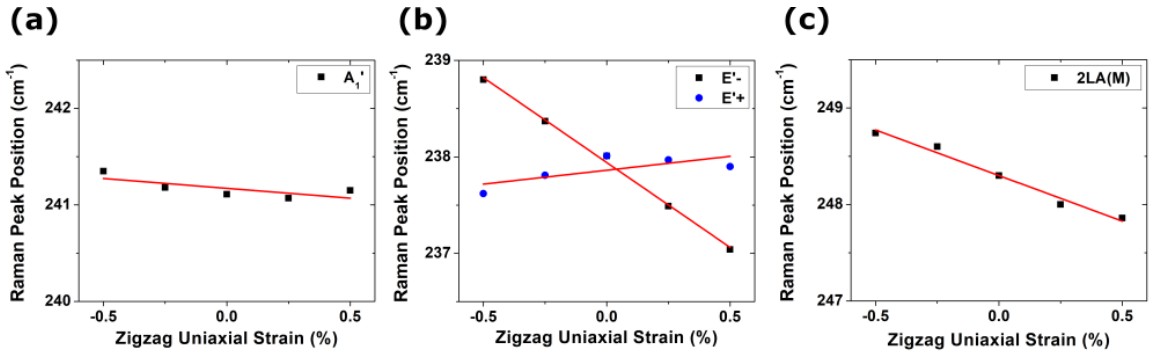

Figure 4.7. Strain dependence of the **(a)** A_1', **(b)** E'+, E'−, and **(c)** second order longitudinal acoustic vibrational modes in monolayer WSe_2 calculated using density functional perturbation theory. Calculations were performed for uniaxial strain in the zigzag direction. The red lines show the linear fit for each set of points.

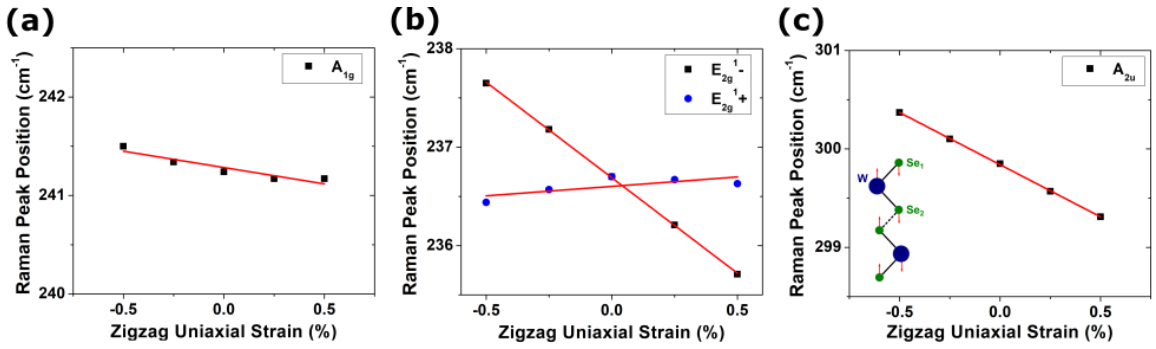

Figure 4.8. Strain dependence of the **(a)** A_{1g}, **(b)** $E_{2g}{}^{1}$+, $E_{2g}{}^{1}$–, and **(c)** out-of-phase A_{2u} vibrational modes in bilayer WSe_2 calculated using density functional perturbation theory. Calculations were performed for uniaxial strain in the zigzag direction. The red lines show the linear fit for each set of points. The inset in **(c)** shows the movement of the atoms for the out-of-phase A_{2u} mode.

We have used DFT to calculate the Raman behavior of the various vibrational modes in monolayer and bilayer WSe_2 to further confirm our experimental results. Because DFT calculations for three-layer WSe_2 are too computationally intensive, we have instead performed DFT calculations on bilayer WSe_2 to estimate the effects of interlayer interactions on the Raman behavior of the vibrational modes for few-layer WSe_2. Figures 4.7 and 4.8 show the strain dependence for the various vibrational modes in monolayer and bilayer WSe_2, respectively, calculated using DFPT. For each optimized structure at each strain, zone-center phonon modes were calculated for the first order modes. For the behavior of the second order longitudinal acoustic phonons, the vibrational frequency is calculated at the M point in the Brillouin zone. The Raman modes for both monolayer and bilayer WSe_2 follow similar behavior to experimental results. The slopes of the linear fits for the Raman modes are used as the strain induced Raman shifts calculated by DFT. The linear fits for strain dependence for the A_1' (A_{1g}) and E'+ ($E_{2g}{}^{1}$+) vibrational modes in monolayer (bilayer) are not as accurate because of the anti-crossing behavior seen between these two modes. The 2LA(M) mode in bilayer WSe_2 calculated using DFPT has not been

conclusively identified, and it remains unclear which eigenmode at the M point corresponds to the LA mode. Because the eigenmode at the M point exhibit different dependences on strain and we are not completely confident in the exact nature of the DFPT calculated 2LA(M) mode in bilayer WSe_2, we choose to not report a strain-induced Raman shift for the 2LA(M) mode in bilayer WSe_2. The out-of-phase A_{2u} vibrational mode that is Raman active due to Davydov splitting[110] has been referred to as the $A_{1g}{}^2$ mode in other work[103] but represent the same vibrational mode.

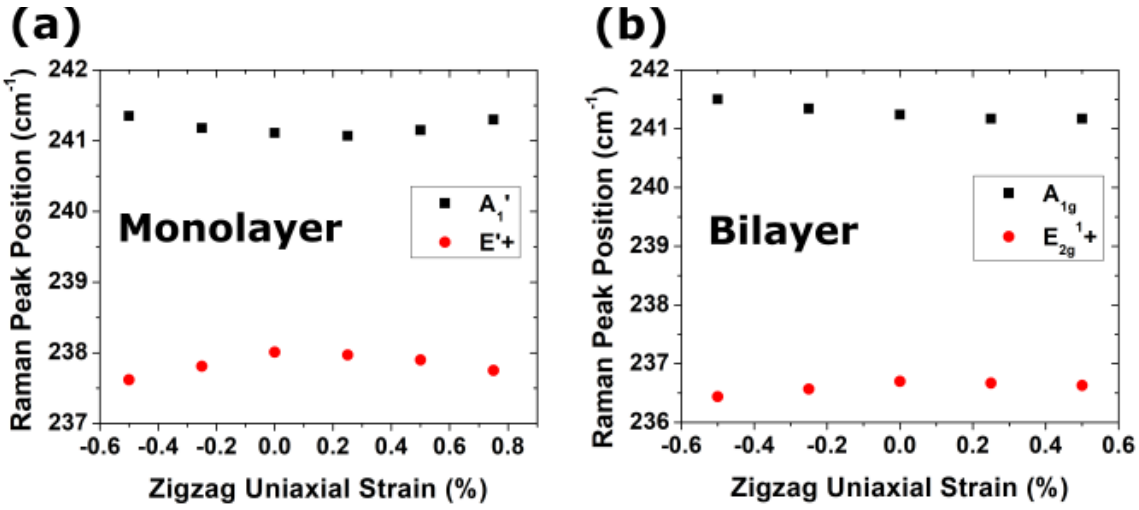

Figure. 4.9. Anti-crossing behavior for the strain dependent Raman shifts for (a) the A_1' (black squares) and E'+ (red circles) vibrational modes in monolayer WSe_2 and (b) the A_{1g} (black squares) and $E_{2g}{}^1$+ (red circles) vibrational modes in bilayer WSe_2 calculated using density functional perturbation theory.

Table 4.1 shows the strain induced Raman shifts for the various vibrational modes in monolayer and bilayer WSe_2 calculated using DFT. In general, the DFT calculated strain induced Raman shifts are similar to the experimental strain induced Raman shifts, with the DFT results generally underestimating the effect of strain on the Raman peak positions in comparison to experimental results. In both monolayer and three-layer WSe_2, we should

observe a splitting of the in-plane E' and E_{2g}^1 modes, respectively, from symmetry breaking due to the applied uniaxial strain, as shown by DFT calculations (which we differentiate with the + and – symbols). However, the peak that is less strain sensitive and remains frequency degenerate with the out-of-plane A' and A_{1g} modes is difficult to measure separately. The experimentally determined strain induced Raman shifts for the E'+ and A_1' modes in monolayer WSe_2 and for the E_{2g}^1+ and A_{1g} modes in three-layer WSe_2 are assumed to be negligible. Based on experimental results and DFT calculations, the unstrained out-of-plane A_1' and in-plane E' vibrational modes in monolayer (A_{1g} and E_{2g}^1 vibrational modes in multilayer) WSe_2 are close in energy. When uniaxial strain is applied in-plane in the zigzag direction, the symmetry of the A_1' and E' vibrational modes in monolayer (A_{1g} and E_{2g}^1 vibrational modes in multilayer) WSe_2 is reduced with the only symmetries remaining being the identity, a C2 axis, and two vertical mirror planes. The symmetry reduction results in the unit cell symmetry going from the D_{3h} (D_{6h} in multilayer) to the C_{2v} point group and both modes belonging to the same irreducible representation (A1) where coupling between the vibrational modes can occur. Coupling of the A_1' and E'+ vibrational modes leads to anti-crossing behavior of the Raman peak positions as uniaxial strain is applied as shown in Figure 4.9. Therefore, the modes do not show obvious linear behavior when strain is applied in the DFT simulations so we choose to report the strain-induced Raman shifts for both modes as relatively negligible, which agrees with experimentally determined results. The DFT calculated strain induced Raman shift of the out-of-phase A_{2u} vibrational mode matches closely the experimentally determined strain induced Raman shift of the multilayer-only peak, which gives further evidence that this peak comes from the A_{2u} mode becoming Raman active due to Davydov splitting.

From the strain induced Raman shifts, we also derive the value of the Grüneisen parameter for a given mode, γ_m, and shear deformation potential, β_m, for the E' mode in monolayer WSe_2 and the E_{2g}^1 in three-layer WSe_2 using the following equations[108]:

$$\gamma_m = -\frac{\Delta\omega_{m+} + \Delta\omega_{m-}}{2\omega_m(1-\nu)\varepsilon}, \tag{4.2}$$

$$\beta_m = \frac{\Delta\omega_{m+} - \Delta\omega_{m-}}{\omega_m(1+\nu)\varepsilon}, \tag{4.3}$$

where ω_m is the frequency of the given mode when unstrained, $\Delta\omega_m$ is the change in frequency per unit strain, and ν is Poisson's ratio, which is that of the PET substrate the WSe_2 flakes are adhering to with a value of 0.34.[108] Under uniaxial strain, strain along the longitudinal direction, which is parallel to the strain axis, is taken to be ε, and strain along the transverse direction is taken to be $-\nu\varepsilon$. Table 4.2 shows the Grüneisen parameter and shear deformation potential values for the E' and E_{2g}^1 modes of monolayer and three-layer WSe_2, respectively, calculated from experimental strain-induce Raman shift values and deformation potential values for the E' and E_{2g}^1 modes of monolayer and bilayer WSe_2, respectively, calculated from strain-induced Raman shift values obtained from DFT simulations. We take $\Delta\omega_m$- to be the measured Raman shift due to strain while we assume $\Delta\omega_m$+ is negligible for deformation potentials calculated from experimentally obtained values. We take the $\Delta\omega_m$- and $\Delta\omega_m$+ values obtained from DFT simulations for the deformation potentials calculated from DFT values. Using experimentally determined strain induced Raman shifts for the E' mode in monolayer WSe_2, $\gamma_{E'}$ is 0.75 ± 0.2 and $\beta_{E'}$ is 0.75 ± 0.2, while for the E_{2g}^1 mode in three-layer WSe_2, $\gamma_{E_{2g}^1}$ is 0.63 ± 0.2 and $\beta_{E_{2g}^1}$ is 0.62 ± 0.2, calculated from experimental values. Using DFT calculated strain induced Raman shifts, for the E' mode in monolayer WSe_2, $\gamma_{E'}$ is 0.48 ± 0.1 and $\beta_{E'}$ is 0.65 ± 0.1, while for the E_{2g}^1 mode in bilayer WSe_2, $\gamma_{E_{2g}^1}$ is 0.54 ± 0.0 and $\beta_{E_{2g}^1}$ is 0.65 ± 0.0. The Grüneisen parameters and shear deformation potentials determined from experimental and

DFT values are in reasonably good agreement. The Grüneisen parameter and shear deformation potentials are comparable to previously reported results in monolayer MoS_2, with values of 1.1 and 0.78, respectively.[9]

Table 4.2. Experimentally determined and DFT calculated Grüneisen parameters and shear deformation potentials for monolayer and three-layer WSe_2

	Grüneisen parameter	**Shear Deformation Potential**
Monolayer, E' mode (Exp.)	0.75 ± 0.2	0.74 ± 0.2
Three-layer, E_{2g}^1 mode (Exp.)	0.63 ± 0.2	0.62 ± 0.2
Monolayer, E' mode (DFT)	0.48 ± 0.1	0.65 ± 0.1
Bilayer, E_{2g}^1 mode (DFT)	0.54 ± 0.04	0.65 ± 0.03

CONCLUSIONS

In conclusion, we have performed detailed Raman spectroscopy studies of uniaxially strained monolayer and three-layer WSe_2 and determined the strain induced Raman shifts of the first order in-plane vibrational modes (E' and E_{2g}^1, respectively) as well as the second order longitudinal acoustic phonon mode (2LA). In three-layer WSe_2, we also clearly show the linear strain dependence of the frequency isolated multilayer only mode. From the strain-induced Raman shift, we are able to experimentally determine the Grüneisen parameter and shear deformation potential for the in-plane vibrational mode for both monolayer and three-layer WSe_2. Successful strain transfer from the PET substrate to the WSe_2 flake is confirmed through measurement of Raman peak positions across the WSe_2 flake while strained. Measured strain induced Raman shifts were found to agree well with values obtained from DFT simulations. These measurements of the phonon

deformation potentials and behavior of the Raman spectra in general are expected to be essential for characterizing and understanding properties of strained heterostructures and devices that incorporate WSe_2.

Chapter 5: Conclusions and Future Work

The work presented in this dissertation shows the capabilities of Raman and TERS to characterize material properties at the nanoscale, specifically strain. Experiments were performed on various material systems including core-shell nanowires, atomically thin MoS_2, and atomically thin WSe_2.

Chapter 2 focuses on experiments performed on Ge-Si_xGe_{1-x} core-shell nanowires where we detect two distinct Raman peaks in the Ge core which we attribute to what we call the core and interface regions. We analyze the local strain configuration in the nanowires, where the Raman behavior of both the core and interface region Raman peaks follow parallel diameter dependence, which indicates that both peaks come from different regions of the Ge core. By placing the Au TERS tip close to the surface of the nanowire, we directly influence the separation between the core and interface peaks that indicates localized probing of the interface region. We performed electromagnetic simulations of the tip and nanowire interaction to better understand the unique physics that occur. By performing Fourier analysis on the simulated electric field, we show that the proximity of the Au TERS tip increased the higher-order Fourier amplitudes in the vicinity of the Au tip. The higher Fourier amplitudes result in increased coupling of intervalence-band transition of phonons, which causes the increased negative shift of the interface peak relative to the core peak.

Further confirmation about the origin of the interface peak shift could be performed by successfully electrically contacting the Ge-Si_xGe_{1-x} core-shell nanowires and attempting to deplete the holes in the 2D hole gas and observing the effect on the Raman spectrum. Further work on core-shell nanowires could also involve performing TERS experiments on similar nanowire structures. Specifically, in thinner 1D structures, the possibility of

taking advantage of the plasmonic gap mode that occurs between a Au substrate and a Au TERS tip could produce significantly enhanced Raman signal that would possibly give significantly more information about the structure.

Chapter 3 summarizes the work on probing monolayer and bilayer MoS_2 with submicron spatial resolution using TERS and TEPL. In these experiments, we have locally strained bilayer MoS_2 using Au nanopyramids patterned with nanosphere lithography. We observe shifted and enhanced PL spectra in the locally tensile strained MoS_2, which we attribute to a decrease in the bandgap energy as well as greater plasmonic enhancement from the gap mode from by the TERS tip and the underlying Au substrate. We also probed the strain dependence of the second order Raman spectrum in bilayer MoS_2, which shows shifts in the Raman peak positions and relative changes in the Raman peaks areas that we attribute to changes in the electronic band structure and phonon dispersion due to tensile strain. DFT calculations show that applying tensile strain affects the energy level of the conduction band minimum as well as the acoustic phonon dispersion, which confirms that changes in the second order Raman spectrum obtained by TERS acts as a useful probe for band structure and phonon mode behavior.

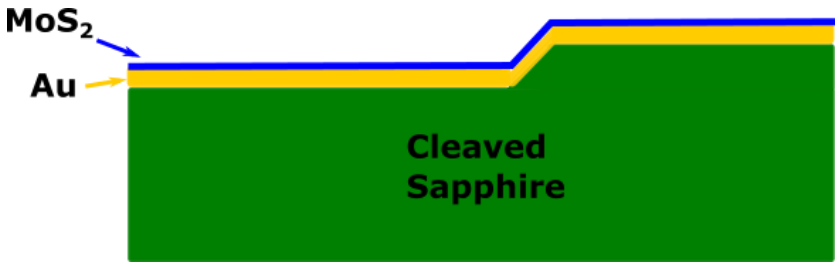

Figure 5.1 Schematic diagram of MoS_2 that has been transferred onto Au coated cleaved sapphire showing a parallel step edge.

One possible future direction for further research into mechanical properties of 2D materials is to create localized strain with different types of nanostructures. One possible platform is to use cleaved sapphire. Cleaved sapphire can create clean parallel step edges where after a 2D material is transferred and adheres to the surface, can create localized strain regions. We have already transferred MoS_2 and CVD grown monolayer graphene sheets onto Au coated cleaved sapphire. Figure 5.1 shows a schematic diagram of MoS_2 that has been transferred onto Au coated cleaved sapphire showing a parallel step edge. Other novel structures could also be used to create various other strain configurations in 2D materials. Novel strain structures could not only be measured with TERS but also PL, where high levels of strain could cause significant shifts in the PL spectra.

Chapter 4 details Raman studies on uniaxially strained monolayer and three-layer WSe_2, where we determine the strain induced Raman shift of the first order in-plane vibrational mode as well as the second order longitudinal acoustic phonon mode. From the strain induced Raman shift, we are able to experimentally determine the Grüneisen parameter and shear deformation potential for the in-plane vibrational mode for both monolayer and three-layer WSe_2. Successful strain transfer from the PET substrate to the WSe_2 flake is confirmed through measuring constant Raman peak positions across the WSe_2 flake while strained. Strain induced Raman shifts were found to also agree with simulated results obtained from DFT simulations. Precise measurement of the phonon deformation potentials and behavior of the Raman spectra in general is essential for understanding mechanical properties of heterostructures and devices that incorporate WSe_2.

The strain induced Raman shifts of WSe_2 deduced by our stretching experiments allows further probing of strained WSe_2 structures. This information can be used in analyzing different WSe_2 based heterostructures where understanding the amount of strain

induced in the WSe_2 is essential to engineering devices. Knowledge about strain distributions could also be correlated to various other material properties such as conductivity.

Appendix A: TERS Operation Procedure

This Appendix should serve as a partial guide to aligning and operating both the Horiba LabRAM and AIST-NT Omegascope for conventional Raman, AFM and TERS experiments. Basic operating information can be found in the manuals for both systems. This guide mostly serves to fill in the gaps not written in the manuals and to offer additional insight learned from operating the system for purposes relevant to the Nanoscale Characterization and Device Lab.

LabRAM Raman Calibration Alignment

1. Align laser on the conventional Raman side on the Si alignment side at D3 power in video mode. Remember, the power setting adjusts which neutral density filter (NDF) is used in the NDF wheel. Generally, we also put an additional NDF in series along the beam line, either D0.3 (50% power) or D0.6 (25% power). Align by centering the laser to the green spot and make sure focusing is also centered. Generally, align using the 50 X and 100 X objectives.
2. To calibrate the Raman, go to Maintenance → Calibration then use the 520.7 cm^{-1} Si peak and zero-order peak to adjust the Koeff and Zero variables so both peaks are properly positioned. The Zero variable shifts the zero-order peak position while the Koeff determines the scaling in frequency for data points away from the zero point.
3. To acquire the signal, make sure the spot is focused visually at using either the 50 X or 100 X objectives. Switch from video to Raman mode and go to D0.6 laser power. Use real time acquisition to continuously acquire Raman spectra to locate the Si peak and the zero-order peak and use the cursor to read the frequency

position. Generally, iterate between aligning to the zero-order peak and Si peak by centering your grating at the corresponding frequency for each.

4. Use the same calibration procedure for both the 300 and 1800 grooves/mm gratings. Peak position calibration should be performed at least once a week.
5. If baseline noise level becomes too low, go to Acquistion → Detector then change the Shift value to adjust the Baseline.

REGULAR ALIGNMENT FOR TERS

Follow the following steps for regular TERS alignment:

1. Perform LabRAM conventional Raman alignment.
2. Use swing mirror to direct laser to AFM.
3. Put in probe holder with tip.
4. If signal intensity appears stable, steps 4 and 5 do not need to be implemented during every alignment but should be checked when signal intensity seems to decrease. Generally, do step 4 at least once a month and step 5 once every couple of months.
5. Set laser power to D2 in video mode. Remove AFM housing and check center of the laser through the side objective using lens paper. Adjust centering with the adjustment screws for the mirror that direct the laser from the Raman system. The laser should be centered in the side objective and fill it relatively fully. When placing AFM housing back in, especially with the 100 X objective screwed in, be very careful of not hitting the objective with the tooth that secures the housing. The objective is very expensive!!
6. Set laser power back to D3 in video mode. If spot is very faint, go to D2 power. Locate position of laser from top objective on a metal sample slide at sample height.

To establish sample height, (1) land probe, (2) retract probe, (3) remove probe holder from housing, and (4) raise sample 2mm. Locate laser and mark it with the cross on the video toolbar.

7. Place in silicon reference sample.
8. Place backlight source in correct position and turn on using the AIST-NT software in the video window. Increase light output till the tip is fully illuminated.
9. If unable to locate tip visually, land tip on sample. Retract and move 0.5 mm from sample.
10. Find substrate Raman signal then position tip at x marked on video.

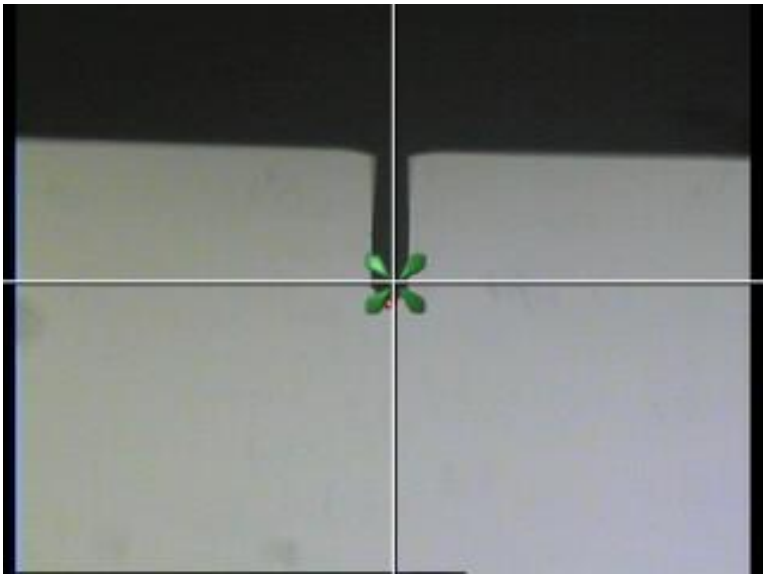

Figure A.1. Visual image of top objective with tip at X marked spot

11. Maximize signal of substrate by adjusting fine z-position screw.

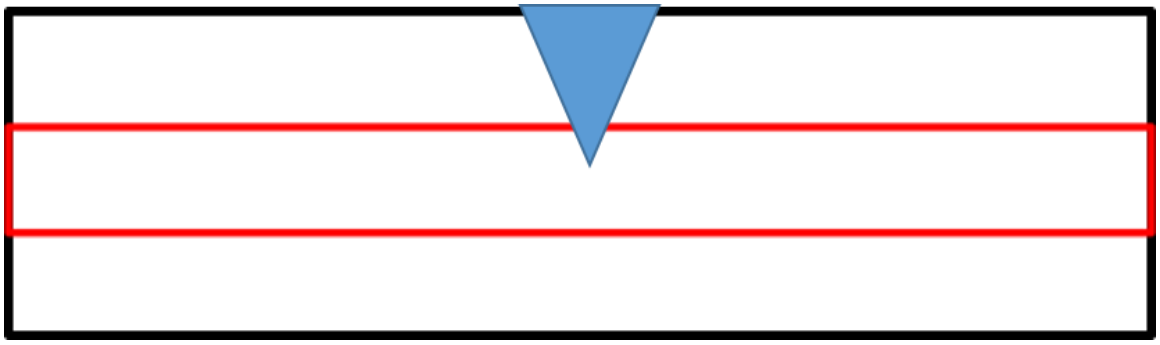

Figure A.2. Position of the Au tip relative to Si band in a XY objective map scan. The Au tip is shown in blue and the Si band is shown in red.

12. Perform a XY objective map scan of size 12 by 6 µm (24 by 12 points (pts)). Map should look like Figure A.2 with the center region outlined in red being the substrate signal. This is best done on a Si substrate.
13. Find tip by looking at Peak area of the background signal. Eventually you want to position tip so that it shades the top area above the substrate signal stripe like that showed in Figure A.2 with the blue triangle.
14. After performing the large area XY objective scan, perform an XZ objective scan, 3 by 6 µm (10 by 18 pts). Center laser position so that the shade (determined by the background peak area caused by the Au tip response) creates and\ hourglass shape with the focal point in the center (shown with the red dot in Fig. A.3).

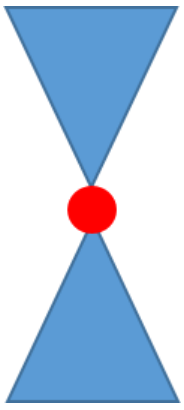

Figure A.3. XZ objective scan with the bright spot centered in the hourglass shape.

15. Perform a smaller XY objective scan, 3x6 µm (10x18 pts)
16. Land Tip. Now obtain the same Si signal plus hourglass shape from the background. Should observe shade of Si signal from the tip.
17. Final alignment based on TERS signal from the sample. If possible, use a reliable reference sample (such as a carbon nanotube sample on Au) to establish final alignment then go to sample of interest.

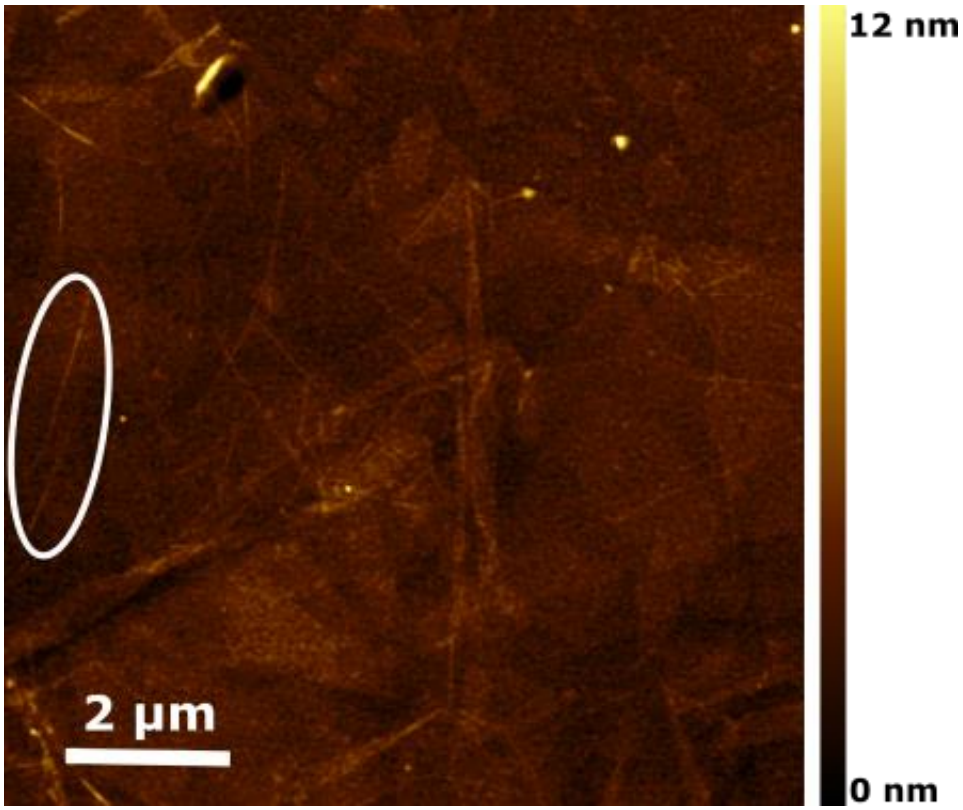

Figure A.4. AFM topographic image of the surface of the nanotube and graphene on Au reference sample. Two example nanotubes that could be used to confirm enhancement are indicated by the white oval.

18. When using the carbon nanotube on Au reference sample, find a nanotube that is approximately 5 nm in height and place tip on the nanotube. Figure A.4 shows an example AFM topographic scan of the carbon nanotube reference sample with example nanotubes highlighted by the white oval.
19. Start obtaining real time Raman spectra (1 second per acquisition) and specifically look at the range from 400 to 1600 cm^{-1}. Use spec-top mode and go into contact. If enhancing, there should be two main peaks that become easily apparent around 1200 to 1600 cm^{-1}.

GENERAL TIPS

1. When performing optical alignment by adjusting screws on mirrors, the general rule of thumb is that the mirror closer to the laser source has more control of the centering of the focusing while the farther mirror has more control of the position of the laser spot. The mirrors are often coupled together so adjusting one mirror often affects both the centering of the focusing and the laser spot position.

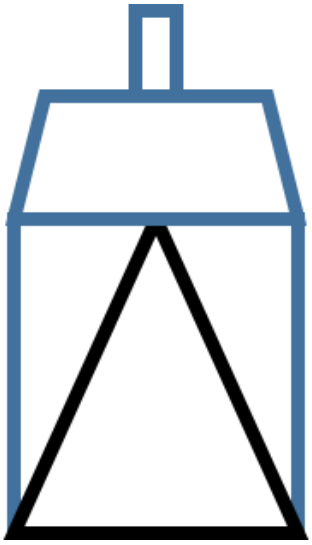

Figure A.5. Position of tip in holder with the triangular top of the holder (shown in black) aligned to the trapezoid below the cantilever.

2. When placing probe into holder, from the top view when the tip holder is in system, the tip should look like the image in Figure A.5. The blue outlined area is the probe itself while the black triangle represents the part of the holder you want to overlap.
3. When putting in probe holder with tip into the AFM housing, be careful. It is generally better to have the probe holder hit the top of the entrance than the bottom.
4. Make sure the tip holder is securely in place by making sure when you move the tip holder gently with your finger, it springs back into the same position.
5. Close laser shutter when not measuring to minimize damage on the tip due to higher temperatures.
6. When using adaptive scan, set the Z error value to:

$$\frac{(Free\ amplitude\ when\ landing) - (\text{Set point})}{2}, \tag{A.1}$$

where the free amplitude is determined from the maximum value of the deflection graph obtained when landing the tip.

7. The contact gain should be in the 80 to 120 range when placing tip in soft contact for TERS.
8. Shutdown feedback before moving tip (this is done automatically with new tip command).
9. Use Auto to land tip after finding tip and visually align laser with tip.
10. Use D3 power when aligning laser to tip.
11. When performing TERS use D1 power with either the 25% or 50% NDF in series with computer controlled ND filter wheel in the beam line.

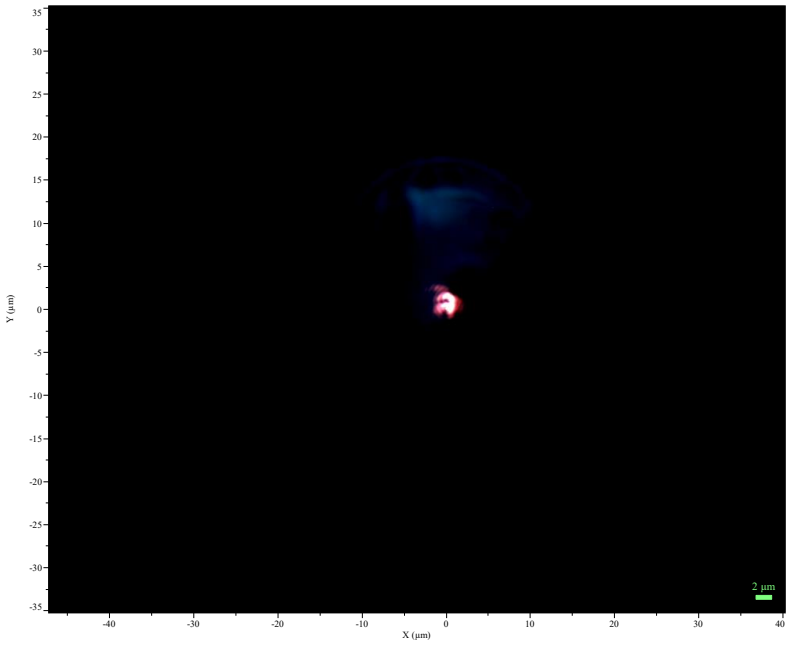

Figure A.6. Optical reflection of laser aligned to tip.

12. For visually aligning the laser and tip, obtain a nice sharp scattering spot, as shown in the example in Figure A.6.

13. Use nitrogen gun to blow out the detector once every few weeks. Eventually the detector will degrade and possibly need replacement. Cleanout dust in fans and other parts of the Raman and AFM system in general.

INTENSIVE ALIGNMENT

If system is dramatically out of alignment, follow the following steps:

1. Remove both top and side objectives.
2. First check if the beam is parallel to the surface when coming from the spectrometer. Use optical posts or ruler to determine this then use align mirror directing laser from the spectrometer.
3. Before removing AFM head, establish sample height with metal slide as sample. (1) Land probe, (2) retract probe 2mm (new tip button), (3) remove probe, and (4) return sample 2mm back to original height.
4. Remove the AFM housing to remove the AFM head. (1) Open front panel to unclip cables, (2) unscrew the four screws securing the AFM head (be careful), and (3) remove head with cables and set aside.
5. Align laser to center of hole leading to mirrors. Do this by loosening screws for the alignment posts then using hex wrench to lower and raise posts as well as reposition the system as a whole.
6. Direct laser to top objective mirror and with AFM housing removed, align to center metal ball housing sits on.
7. Place housing back in with the same sample at same height when probe was landed. With Sharpie, mark on the metal slide where the laser is hitting.
8. Switch to side illumination with the swing mirror.

9. Align to same spot marked with the sharpie with alignment posts and positioning of the system. Iterate between aligning the top view and side view to the same spot till both are aligned.
10. Center laser through the side objective hole both at entrance and exit. AIST-NT has a tool but same possible with alignment disks.
11. Remove AFM housing, screw objectives back into place. When placing AFM housing back in, especially with the 100x objective in, be very careful of not hitting the objective with the tooth that secures the housing.
12. With camera at 20x magnification, align top objective focus on camera till its symmetric by adjusting position of whole system and alignment posts by using the Video option in the AIST-NT software. You may need to remove the housing to adjust the post below the housing. Again, be careful removing and placing the housing back in to not damage the objective.
13. Remove AFM housing to reattach the AFM head. Secure head with all four screws tight but not with too much force.
14. Open front panel and reclip in cable so it is secure, can move, and will not be damaged when the front panel is placed back on.
15. Lower sample 2 mm and put probe back in position.
16. If loud sounds occur after putting side objective back in, adjust Parameter tables for Scan2 to the following: x = 16.5, y = 16.5, and z = 33.

AFM, RAMAN, AND TERS PROCEDURE

1. Depending on laser wavelength used, check if correct filters are in place and the mirror switch is in the correct position. Check which additional ND filters are placed along the beam path.
2. Turn on and open shutters on the Laser control box. Turn on green laser if using green laser.
3. Turn on AFM control box.
4. Open latest version of the AIST software. Open Horiba LabSpec software.
5. Make sure the excitation wavelength used in measurements matches that in the Horiba software.
6. Make sure the internal optics are configured for the wavelength desired, such as the correct mirrors and notch filters are in place.
7. Open camera view (make sure beam splitter is set to video instead of Raman setting) to center laser. Make sure laser power is at D0.3 or below.
8. Center beam and focusing of laser spot by adjusting mirrors either at the cut out circular hole at the back of Raman for the red laser or in the optics housing for the green laser.
9. If performing conventional Raman, make sure the final swing mirror directs the laser to the microscope stage and proceed with conventional Raman. To see surface of the sample, turn on light source next to the Raman. Remember, what you see in the top objective will not be exactly where your tip will land due to the top objective not being completely normal to the sample surface.
10. For conventional Raman measurements, when taking data make sure you limit ambient light, switch to Raman mode, and are using the 100x objective. Laser power used is sample dependent but usually start with D0.6.

11. If performing TERS, use the mirror switch to direct the laser to the AFM. Make sure to turn on the AFM server in the Horiba software.
12. Use the Regular Alignment Procedure to align tip to laser. Follow General Tips for tip alignment.
13. After alignment is complete, lower reference sample by pressing new tip twice (lowers 4 mm in total) then remove reference sample.
14. Place in sample of interest and locate manually with sample placement tweezers general area of interest. **Be careful not to damage the tip when moving the sample around.** Once general area is found, approach surface.
15. Turn on adaptive scanning and set Z-error to value stated in General Tips. The adaptive scanning toggle can be found by clicking the settings wheel icon.
16. When scanning with tapping mode AFM, be conservative with scan speed to maintain tip integrity. Recommended scan rate of 1.0 for a 10x10 μm area. When performing scans of larger areas, scale the scan rate appropriately.
17. After finishing measurements, use z-motor → new tip twice to lift tip 4 mm above sample then remove sample. Re-center the sample stage using the moto xyz controller in the x and y, if x and y movement was used.
18. Remove tip holder carefully and place tip back into box.
19. Close both the Raman and AFM software.
20. Turn off the AFM control box.
21. Turn off laser power and shutter.

References

1. Smith, E. & Dent, G. *Modern Raman Spectroscopy- A Practical Approach*. (John Wiley & Sons, 2005).
2. *Modern Techniques in Raman Spectroscopy*. (John Wiley & Sons, 1996).
3. Khanna, R. K., Stranz, D. D. & Donn, B. A spectroscopic study of intermediates in the condensation of refractory smokes: Matrix isolation experiments of SiO. *J. Chem. Phys.* **74,** 2108–2115 (1981).
4. Moore, D. S. & McGrane, S. D. Raman temperature measurement. *J. Phys. Conf. Ser.* **500,** 192011 (2014).
5. Oja, I. *et al.* Crystal quality studies of CuInS2 films prepared by spray pyrolysis. *Thin Solid Films* **480–481,** 82–86 (2005).
6. Ujihara, T. *et al.* Crystal quality of a 6H-SiC layer grown over macrodefects by liquid-phase epitaxy: A Raman spectroscopic study. *Thin Solid Films* **476,** 206–209 (2005).
7. Olego, D. & Cardona, M. Self-energy effects of the optical phonons of heavily doped p-GaAs and p-Ge. *Phys. Rev. B* **23,** (1981).
8. Zhang, Z. *et al.* Probing nanoscale variations in strain and band structure of MoS2 on Au nanopyramids using tip-enhanced Raman spectroscopy. *Phys. Rev. B* **97,** 85305 (2018).
9. Conley, H. J. *et al.* Bandgap Engineering of Strained Monolayer and Bilayer MoS 2. *Nano Lett.* **13,** 3626–3630 (2013).
10. Rice, C. *et al.* Raman-scattering measurements and first-principles calculations of strain-induced phonon shifts in monolayer MoS2. *Phys. Rev. B* **87,** 81307 (2013).
11. Ureña, F., Olsen, S. H., Raskin, J., Olsen, S. H. & Raskin, J. Raman measurements of uniaxial strain in silicon nanostructures Raman measurements of uniaxial strain in silicon nanostructures. **144507,** 0–11 (2013).
12. Dillen, D. C., Varahramyan, K. M., Corbet, C. M. & Tutuc, E. Raman spectroscopy and strain mapping in individual Ge-Si_{x}Ge_{1−x} core-shell nanowires. *Phys. Rev. B* **86,** 45311 (2012).
13. Bao, W. *et al.* Visualizing nanoscale excitonic relaxation properties of disordered edges and grain boundaries in monolayer molybdenum disulfide. *Nat. Commun.* **6,** 7993 (2015).
14. Van Der Zande, A. M. *et al.* Grains and grain boundaries in highly crystalline monolayer molybdenum disulphide. *Nat. Mater.* **12,** 554–561 (2013).
15. Lee, Y. *et al.* Characterization of the structural defects in CVD-grown monolayered MoS 2 using near-field photoluminescence imaging. *Nanoscale* **7,**

11909–11914 (2015).

16. Hong, Y., Lam, J. W. Y. & Tang, B. Z. Aggregation-induced emission: phenomenon, mechanism and applications. *Chem. Commun.* 4332 (2009). doi:10.1039/b904665h

17. Weber, J. & Alonso, M. I. Near-band-gap photoluminescence of Si-Ge alloys. *Phys. Rev. B* **40,** 5683–5693 (1989).

18. Castellanos-Gomez, A. *et al.* Local Strain Engineering in Atomically Thin MoS 2. *Nano Lett.* **13,** 5361–5366 (2013).

19. Fleischmann, M., Hendra, P. J. & McQuillan, A. J. Raman spectra of pyridine adsorbed at a silver electrode. *Chem. Phys. Lett.* **26,** 163–166 (1974).

20. Le Ru, E. C. & Etchegoin, P. G. Single-Molecule Surface-Enhanced Raman Spectroscopy. *Annu. Rev. Phys. Chem.* **63,** 65–87 (2012).

21. Kennedy, B. J., Spaeth, S., Dickey, M. & Carron, K. T. Determination of the Distance Dependence and Experimental Effects for Modified SERS Substrates Based on Self-Assembled Monolayers Formed Using Alkanethiols. *J. Phys. Chem. B* **103,** 3640–3646 (1999).

22. El-Ansary, A. Nanoparticles as biochemical sensors. *Nanotechnol. Sci. Appl.* **3,** 65 (2010).

23. Brosseau, C. L., Casadio, F. & Van Duyne, R. P. Revealing the invisible: Using surface-enhanced Raman spectroscopy to identify minute remnants of color in Winslow Homer's colorless skies. *J. Raman Spectrosc.* **42,** 1305–1310 (2011).

24. Hayazawa, N., Inouye, Y., Sekkat, Z. & Kawata, S. Metallized tip amplification of near-field Raman scattering. *Opt. Commun.* **183,** 333–336 (2000).

25. Anderson, M. S. Locally enhanced Raman spectroscopy with an atomic force microscope. *Appl. Phys. Lett.* **76,** 3130–3132 (2000).

26. Stöckle, R. M., Suh, Y. D., Deckert, V. & Zenobi, R. Nanoscale chemical analysis by tip-enhanced Raman spectroscopy. *Chem. Phys. Lett.* **318,** 131–136 (2000).

27. Park, K.-D. *et al.* Hybrid Tip-Enhanced Nanospectroscopy and Nanoimaging of Monolayer WSe 2 with Local Strain Control. *Nano Lett.* **16,** 2621–2627 (2016).

28. Ikeda, K., Fujimoto, N., Uehara, H. & Uosaki, K. Raman scattering of aryl isocyanide monolayers on atomically flat Au(111) single crystal surfaces enhanced by gap-mode plasmon excitation. *Chem. Phys. Lett.* **460,** 205–208 (2008).

29. Xiang, J. *et al.* Ge/Si nanowire heterostructures as high-performance field-effect transistors. *Nature* **441,** 489–93 (2006).

30. Nah, J., Dillen, D. C., Varahramyan, K. M., Banerjee, S. K. & Tutuc, E. Role of confinement on carrier transport in Ge-Si(x)Ge(1-x) core-shell nanowires. *Nano Lett.* **12,** 108–12 (2012).

31. Xiang, J., Vidan, a, Tinkham, M., Westervelt, R. M. & Lieber, C. M. Ge/Si nanowire mesoscopic Josephson junctions. *Nat. Nanotechnol.* **1,** 208–13 (2006).

32. Sau, J. D., Tewari, S. & Das Sarma, S. Experimental and materials considerations for the topological superconducting state in electron- and hole-doped semiconductors: Searching for non-Abelian Majorana modes in 1D nanowires and 2D heterostructures. *Phys. Rev. B* **85,** 64512 (2012).

33. Björk, M. T. *et al.* Few-Electron Quantum Dots in Nanowires. *Nano Lett.* **4,** 1621–1625 (2004).

34. Hu, Y. *et al.* A Ge/Si heterostructure nanowire-based double quantum dot with integrated charge sensor. *Nat. Nanotechnol.* **2,** 622–5 (2007).

35. Li, D. *et al.* Thermal conductivity of individual silicon nanowires. *Appl. Phys. Lett.* **83,** 2934 (2003).

36. Chen, R. *et al.* Thermal Conductance of Thin Silicon Nanowires. *Phys. Rev. Lett.* **101,** 105501 (2008).

37. Hochbaum, A. I. *et al.* Enhanced thermoelectric performance of rough silicon nanowires. *Nature* **451,** 163–7 (2008).

38. Boukai, A. I. *et al.* Silicon nanowires as efficient thermoelectric materials. *Nature* **451,** 168–71 (2008).

39. Schmidt, V., McIntyre, P. & Gösele, U. Morphological instability of misfit-strained core-shell nanowires. *Phys. Rev. B* **77,** 235302 (2008).

40. Liang, Y., Nix, W. D., Griffin, P. B. & Plummer, J. D. Critical thickness enhancement of epitaxial SiGe films grown on small structures. *J. Appl. Phys.* **97,** 43519 (2005).

41. Grönqvist, J. *et al.* Strain in semiconductor core-shell nanowires. *J. Appl. Phys.* **106,** 53508 (2009).

42. Cerdeira, F. & Cardona, M. Effect of Carrier Concentration on the Raman Frequencies of Si and Ge. *Phys. Rev. B* **5,** 1440–1454 (1972).

43. Bertolazzi, S., Brivio, J. & Kis, A. Stretching and breaking of ultrathin MoS 2. *ACS Nano* **5,** 9703–9709 (2011).

44. Cooper, R. C. *et al.* Nonlinear elastic behavior of two-dimensional molybdenum disulfide. *Phys. Rev. B* **87,** 35423 (2013).

45. Yin, Z. *et al.* Single-Layer MoS 2 Phototransistors. *ACS Nano* **6,** 74–80 (2012).

46. Wang, Q. H., Kalantar-Zadeh, K., Kis, A., Coleman, J. N. & Strano, M. S. Electronics and optoelectronics of two-dimensional transition metal dichalcogenides. *Nat. Nanotechnol.* **7,** 699–712 (2012).

47. Yu, W. J. *et al.* Vertically stacked multi-heterostructures of layered materials for

logic transistors and complementary inverters. *Nat. Mater.* **12,** 246–252 (2013).

48. Palacios-Berraquero, C. *et al.* Large-scale quantum-emitter arrays in atomically thin semiconductors. *Nat. Commun.* **8,** 15093 (2017).

49. Branny, A., Kumar, S., Proux, R. & Gerardot, B. D. Deterministic strain-induced arrays of quantum emitters in a two-dimensional semiconductor. *Nat. Commun.* **8,** 15053 (2017).

50. Kim, S. K. *et al.* Directional dependent piezoelectric effect in CVD grown monolayer MoS 2 for flexible piezoelectric nanogenerators. *Nano Energy* **22,** 483–489 (2016).

51. Wu, W. *et al.* Piezoelectricity of single-atomic-layer MoS2 for energy conversion and piezotronics. *Nature* **514,** 470–474 (2014).

52. Brennan, C. J. *et al.* Out-of-Plane Electromechanical Response of Monolayer Molybdenum Disulfide Measured by Piezoresponse Force Microscopy. *Nano Lett.* **17,** 5464–5471 (2017).

53. Frey, G. L., Tenne, R., Matthews, M. J., Dresselhaus, M. S. & Dresselhaus, G. Raman and resonance Raman investigation of MoS2 nanoparticles. *Phys. Rev. B* **60,** 2883–2892 (1999).

54. Carvalho, B. R. *et al.* Intervalley scattering by acoustic phonons in two-dimensional MoS2 revealed by double-resonance Raman spectroscopy. *Nat. Commun.* **8,** 14670 (2017).

55. Chuang, H. J. *et al.* High mobility WSe2 p - And n - Field-effect transistors contacted by highly doped graphene for low-resistance contacts. *Nano Lett.* **14,** 3594–3601 (2014).

56. Movva, H. C. P. *et al.* High-Mobility Holes in Dual-Gated WSe2 Field-Effect Transistors. *ACS Nano* **9,** 10402–10410 (2015).

57. Amin, B., Kaloni, T. P. & Schwingenschlögl, U. Strain engineering of WS_2, WSe_2, and WTe_2. *RSC Adv.* **4,** 34561 (2014).

58. Yang, C. xia, Zhao, X. & Wei, S. yi. Manipulation of electronic structure in WSe2 monolayer by strain. *Solid State Commun.* **245,** 70–74 (2016).

59. Sahin, H. *et al.* Anomalous Raman spectra and thickness-dependent electronic properties of WSe2. *Phys. Rev. B - Condens. Matter Mater. Phys.* **87,** 1–6 (2013).

60. Zhang, S., Lopez, F. J., Hyun, J. K. & Lauhon, L. J. Direct detection of hole gas in Ge-Si core-shell nanowires by enhanced Raman scattering. *Nano Lett.* **10,** 4483–7 (2010).

61. Wagner, R. S. & Ellis, W. C. Vapor-Liquid-Solid Mechanism of Single Crystal Growth. *Appl. Phys. Lett.* **4,** 89 (1964).

62. Raychaudhuri, S. & Yu, E. T. Calculation of critical dimensions for wurtzite and

cubic zinc blende coaxial nanowire heterostructures. *J. Vac. Sci. Technol. B Microelectron. Nanom. Struct.* **24,** 2053 (2006).

63. Richard, S., Aniel, F. & Fishman, G. Energy-band structure of Ge, Si, and GaAs: A thirty-band k·p method. *Phys. Rev. B* **70,** 235204 (2004).

64. Olego, D., Cardona, M. & Rössler, U. Intra- and inter-valence-band electronic Raman scattering in heavily doped p-GaAs. *Phys. Rev. B* **22,** 1905–1911 (1980).

65. Pinczuk, A. & Burstein, E. Fundamentals of Inelastic Scattering in Semiconductors and Insulators. in *Light Scattering in Solids* (ed. Cardona, M.) 23–78 (Springer-Verlag, 1975).

66. Abstreiter, G., Cardona, M. & Pinczuk, A. Light Scattering by Free Carrier Excitations in Semiconductors. in *Light Scattering in Solids IV* (eds. Cardona, M. & Guntherodt, G.) 5–145 (Springer-Verlag, 1984).

67. Fano, U. Effects of Configuration Interaction on Intensities and Phase Shifts. *Phys. Rev.* **124,** 1866–1878 (1961).

68. Cerdeira, F., Fjeldly, T. A. & Cardona, M. Effect of Free Carriers on Zone-Center Vibrational Modes in Heavily Doped p-type Si. II. Optical Modes. *Phys. Rev. B* **8,** 4734–4745 (1973).

69. Palik, E. D. *Handbook of Optical Constants of Solids*. (Academic Press, 1998).

70. Ganesan, S., Maradudin, A. . & Oitmaa, J. A lattice theory of morphic effects in crystals of the diamond structure. *Ann. Phys. (N. Y).* **56,** 556–594 (1970).

71. Menéndez, J., Singh, R. & Drucker, J. Theory of strain effects on the Raman spectrum of Si-Ge core-shell nanowires. *Ann. Phys.* **523,** 145–156 (2011).

72. Loudon, R. The Raman effect in crystals. *Adv. Phys.* **13,** 423–482 (1964).

73. Reparaz, J. S., Bernardi, a., Goñi, a. R., Alonso, M. I. & Garriga, M. Composition dependence of the phonon strain shift coefficients of SiGe alloys revisited. *Appl. Phys. Lett.* **92,** 81909 (2008).

74. Cerdeira, F., Buchenauer, C. J., Pollak, F. H. & Cardona, M. Stress-Induced Shifts of First-Order Raman Frequencies of Diamond- and Zinc-Blende-Type Semiconductors. *Phys. Rev. B* **5,** 580–593 (1972).

75. Wortman, J. J. & Evans, R. a. Young's Modulus, Shear Modulus, and Poisson's Ratio in Silicon and Germanium. *J. Appl. Phys.* **36,** 153 (1965).

76. Weber, W. Adiabatic bond charge model for the phonons in diamond, Si, Ge, and α-Sn. *Phys. Rev. B* **15,** 4789–4803 (1977).

77. Watkins, G. & Fowler, W. Resonant interactions of optical phonons with acceptor continuum states in silicon. *Phys. Rev. B* **16,** 4524–4529 (1977).

78. Liu, Y. *et al.* Mesoscale Imperfections in MoS 2 Atomic Layers Grown by a Vapor

Transport Technique. *Nano Lett.* **14,** 4682–4686 (2014).

79. Lloyd, D. *et al.* Band Gap Engineering with Ultralarge Biaxial Strains in Suspended Monolayer MoS 2. *Nano Lett.* **16,** 5836–5841 (2016).

80. Yang, Z., Aizpurua, J. & Xu, H. Electromagnetic field enhancement in TERS configurations. *J. Raman Spectrosc.* **40,** 1343–1348 (2009).

81. Giannozzi, P. *et al.* QUANTUM ESPRESSO: A modular and open-source software project for quantum simulations of materials. *J. Phys. Condens. Matter* **21,** 395502–395520 (2009).

82. Vanderbilt, D. Soft self-consistent pseudopotentials in a generalized eigenvalue formalism. *Phys. Rev. B* **41,** 7892–7895 (1990).

83. Perdew, J. P. *et al.* Erratum: Atoms, molecules, solids, and surfaces: Applications of the generalized gradient approximation for exchange and correlation (Physical Review B (1993) 48, 7, (4978)). *Physical Review B* **48,** 4978 (1993).

84. Grimme, S. Semiempirical GGA-type density functional constructed with a long-range dispersion correction. *J. Comput. Chem.* **27,** 1787–1799 (2006).

85. Monkhorst, H. J. & Pack, J. D. Special points for Brillouin-zone intergrations. *Phys. Rev. B* **13,** 5897–5899 (1978).

86. Böker, T. *et al.* Band structure of MoS2, MoSe2, and α−MoTe2: Angle-resolved photoelectron spectroscopy and ab initio calculations. *Phys. Rev. B* **64,** 235305 (2001).

87. Peelaers, H. & Van de Walle, C. G. Effects of strain on band structure and effective masses in MoS <math display='inline'> <msub> <mrow/> <mn>2</mn> </msub> </math>. *Phys. Rev. B* **86,** 241401 (2012).

88. Ramasubramaniam, A., Naveh, D. & Towe, E. Tunable band gaps in bilayer transition-metal dichalcogenides. *Phys. Rev. B* **84,** 205325 (2011).

89. Lee, C. *et al.* Anomalous Lattice Vibrations of Single- and Few-Layer MoS 2. *ACS Nano* **4,** 2695–2700 (2010).

90. Mak, K. F., Lee, C., Hone, J., Shan, J. & Heinz, T. F. Atomically Thin MoS2 : A New Direct-Gap Semiconductor. *Phys. Rev. Lett.* **105,** 136805 (2010).

91. Splendiani, A. *et al.* Emerging photoluminescence in monolayer MoS2. *Nano Lett.* **10,** 1271–1275 (2010).

92. Mak, K. F. *et al.* Tightly bound trions in monolayer MoS2. *Nat. Mater.* **12,** 207–211 (2013).

93. Buscema, M., Steele, G. A., van der Zant, H. S. J. & Castellanos-Gomez, A. The effect of the substrate on the Raman and photoluminescence emission of single-layer MoS2. *Nano Res.* **7,** 1–11 (2014).

94. Wang, R. *et al.* Ultrafast and spatially resolved studies of charge carriers in atomically thin molybdenum disulfide. *Phys. Rev. B* **86,** 45406 (2012).

95. Shin, B. G. *et al.* Indirect Bandgap Puddles in Monolayer MoS2 by Substrate-Induced Local Strain. *Adv. Mater.* **28,** 9378–9384 (2016).

96. Lee, J.-U. *et al.* Strain-shear coupling in bilayer MoS2. *Nat. Commun.* **8,** 1370 (2017).

97. Duan, X. *et al.* Lateral epitaxial growth of two-dimensional layered semiconductor heterojunctions. *Nat. Nanotechnol.* **9,** 1024–1030 (2014).

98. Huang, C. *et al.* Lateral heterojunctions within monolayer MoSe 2 –WSe 2 semiconductors. *Nat. Mater.* **13,** 1096–1101 (2014).

99. Zhao, W. *et al.* Lattice dynamics in mono- and few-layer sheets of WS2 and WSe2. *Nanoscale* **5,** 9677 (2013).

100. Zhao, W. *et al.* Evolution of electronic structure in atomically thin sheets of ws 2 and wse2. *ACS Nano* **7,** 791–797 (2013).

101. Dai, Z. *et al.* Mechanical behavior and properties of hydrogen bonded graphene/polymer nano-interfaces. *Compos. Sci. Technol.* **136,** 1–9 (2016).

102. Kim, K. *et al.* van der Waals Heterostructures with High Accuracy Rotational Alignment. *Nano Lett.* **16,** 1989–1995 (2016).

103. Terrones, H. *et al.* New first order Raman-active modes in few layered transition metal dichalcogenides. *Sci. Rep.* **4,** 4215 (2014).

104. Malard, L. M., Alencar, T. V., Barboza, A. P. M., Mak, K. F. & De Paula, A. M. Observation of intense second harmonic generation from MoS2 atomic crystals. *Phys. Rev. B - Condens. Matter Mater. Phys.* **87,** 1–5 (2013).

105. *We used W.pbe-nsp-van.UPF and Se.pbe-n-rrkus_psl.0.2.UPF from http://www.quantum-espresso.org*.

106. Perdew, J. P., Burke, K. & Ernzerhof, M. Generalized Gradient Approximation Made Simple. *Phys. Rev. Lett.* **77,** 3865–3868 (1996).

107. W.J. Schutte, J.L. De Boer, F. J. Crystal Structures of Tungsten Disulfide and Diselenide. *J. Solid State Chem.* **70,** 207–209 (1987).

108. Mohiuddin, T. M. G. *et al.* Uniaxial strain in graphene by Raman spectroscopy: G peak splitting, Grüneisen parameters, and sample orientation. *Phys. Rev. B - Condens. Matter Mater. Phys.* **79,** 1–8 (2009).

109. Del Corro, E. *et al.* Atypical Exciton-Phonon Interactions in WS2 and WSe2 Monolayers Revealed by Resonance Raman Spectroscopy. *Nano Lett.* **16,** 2363–2368 (2016).

110. Kim, S., Kim, K., Lee, J.-U. & Cheong, H. Excitonic resonance effects and

Davydov splitting in circularly polarized Raman spectra of few-layer WSe 2. *2D Mater.* **4,** 45002 (2017).

111. Zhang, R., Koutsos, V. & Cheung, R. Elastic properties of suspended multilayer WSe 2. *Appl. Phys. Lett.* **108,** 42104 (2016).

112. Jiang, T., Huang, R. & Zhu, Y. Interfacial sliding and buckling of monolayer graphene on a stretchable substrate. *Adv. Funct. Mater.* **24,** 396–402 (2014).

113. Wang, G. *et al.* Tuning the Interfacial Mechanical Behaviors of Monolayer Graphene/PMMA Nanocomposites. *ACS Appl. Mater. Interfaces* **8,** 22554–22562 (2016).